An Electrochemical and Spectroscopic Investigation of Nickel Electrodes in Alkaline Media for Applications in Electro-Catalysis

David S. Hall

Thesis submitted to the
Faculty of Graduate and Postdoctoral Studies
In partial fulfillment of the requirements
For the PhD degree in Chemistry

Department of Chemistry
Faculty of Science
University of Ottawa

Abstract

Nickel-based catalysts in aqueous alkaline media are low-cost electrode materials for electrolytic hydrogen generation, a renewable method of producing fuel and industrial feedstock. However, further work is necessary to develop inexpensive electro-catalyst materials with high activity and long-term stability. This thesis employs spectroscopic and electrochemical methods to directly address specific research problems for the development of improved materials and devices with commercial or industrial value. The first chapter reviews the applications of nickel electrodes; the structures of nickel, nickel hydroxides, and nickel hydrides; and techniques for measuring the electrochemically active surface area (A_{ECSA}) of nickel. In the second chapter, electrochemically precipitated nickel hydroxide materials are fully characterized by Raman spectroscopy, Fourier-transform infrared (FT-IR) spectroscopy, X-ray photoelectron spectroscopy (XPS), and X-ray diffraction (XRD). This work unifies and simplifies the large body of literature on the topic by considering two fundamental phases, α- and β-$Ni(OH)_2$, and various types and extents of structural disorder. The third chapter examines and demonstrates the potential applications of in situ Raman spectroscopy by monitoring the spontaneous ageing of α-$Ni(OH)_2$ to β-$Ni(OH)_2$ in pure water at room temperature. The fourth chapter considers the longstanding problem of electrode deactivation, the gradual decrease in nickel electro-catalyst activity during prolonged hydrogen production. Voltammetric and XRD evidence demonstrates that hydrogen atoms can incorporate into the electrode material and cause structural disorder or the formation of α-NiH_x and β-NiH_x at the surface. The voltammetric formation of NiO_x, α-$Ni(OH)_2$, β-$Ni(OH)_2$, and β-NiOOH surface species are examined by electrochemical and XPS measurements. The fifth chapter of this thesis presents a new method to measure the A_{ECSA} of

nickel, in situ, by the addition of an oxalate salt to the alkaline electrolyte. Oxalate adsorbs onto the (001) surface of the surface $Ni(OH)_2$, as evidenced by voltammetric and attenuated total reflectance (ATR) FT-IR spectroscopy measurements. The adsorbed oxalate limits the surface hydroxide to a single layer. The surface $NiOOH/Ni(OH)_2$ reduction peak during the reverse scan may be used to accurately and precisely measure the A_{ECSA}. The error of this method is estimated at < 10 %.

Table of Contents

Acknowledgements

This work was supported by National Research Council Canada (NRC), the Natural Sciences and Engineering Research Council of Canada (NSERC) and the University of Ottawa. All experimental work was conducted at the NRC Montreal Road campus in Ottawa.

The research in this thesis was performed under the guidance and supervision of Dr. Barry MacDougall and Dr. Christina Bock. It has been a pleasure to learn from their vast knowledge, experience, and their creativity. I have appreciated their mentorship, their friendship, and I admire their dedication to science.

A significant portion of the research in this thesis was performed in collaboration with Dr. David Lockwood. I have thoroughly enjoyed our long discussions interpreting results and developing new ideas. He has been a valued mentor and has become a true friend.

This work was also supported by the contributions of several experts at the NRC. Shawn Poirier performed all Raman spectroscopy measurements presented in this thesis. Bussaraporn Patarachao performed all XRD measurements presented in this thesis and also assisted with the interpretation of these results. I also acknowledge the contributions of David Kingston, who assisted with the XPS measurements and interpretation; Dr. Gregory Marshall, who assisted with the XPS interpretation and the FT-IR measurements; Dr. Pamela Whitfield, who assisted with the XRD interpretation; and Dr. Yvon LePage, who assisted with the XRD interpretation.

My academic studies would not have been possible without the continued support of my parents, who have always encouraged me to follow my passions and to do my best. I also acknowledge the example of my brothers. By emulating their successes, I have achieved success for myself.

Finally, I acknowledge the contributions of my beloved wife Laura. I have relied on her guidance and support throughout my studies. She has always been there to help me in all aspects of my life. She is an exceptional scientist herself and I thoroughly enjoy our passionate discussions of scientific works, which often include our own. My greatest supporter and my keenest critic, I appreciate her continued love and companionship.

Table of Tables

Table of Figures

List of Abbreviations

A_{ECSA}	Electrochemically active surface area
ATR	Attenuated total reflectance
C_{dl}	Double layer capacitance
CE	Counter electrode
CPE	Constant-phase element
DTGS	Deuterated triglycine sulfate
EIS	Electrochemical impedance spectroscopy
EQCM	Electrochemical quartz crystal microbalance
EXAFS	Extended X-ray absorption fine structure
fcc	Face-centred cubic
FT	Fourier transform
FWHM	Full width at half maximum
HER	Hydrogen evolution reaction
INS	Inelastic neutron scattering
IR	Infrared
LO	Longitudinal optical
OER	Oxygen evolution reaction
PEM	Polyelectrolyte membrane
RE	Reference electrode
RHE	Reversible hydrogen electrode
RHEED	Reflection high energy electron diffraction

SCE	Saturated calomel electrode
SERS	Surface-enhanced Raman spectroscopy
TO	Transverse optical
UV/vis	Ultraviolet/visible
XPS	X-ray photoelectron spectroscopy
XRD	X-ray diffraction

1. General Introduction

Part of the literature review presented in this chapter is adapted from a manuscript in preparation for submission to a peer-reviewed journal:

Hall, D.S., Lockwood, D.J., Bock, C., MacDougall, B.R. Nickel Hydroxides: A Review of the Structures, Preparations, and Properties. *Proc. R. Soc. A* (to be submitted fall 2014).

1.1. Nickel Electrodes and Applications in Electro-catalysis

Hydrogen generation by water electrolysis is a renewable method of producing high purity fuel and industrial chemical feedstock (*e.g.*, for float glass manufacturing, petroleum refining and ammonia production), where large-scale stationary production can be integrated into the existing electrical distribution infrastructure [1-3]. Approximately 65 million metric tonnes of H_2 with a value of about $100 billion are produced and used annually [1, 3], of which electrolysis accounts for ~4 % [1, 4]. Polymer electrolyte membrane (PEM) cells, which use noble-metal-based electrode materials in acidic media, offer high energy efficiency and are commonly used for small-scale H_2 production. However, these units are too expensive to compete as large-scale sources of H_2. Hence, this work considers H_2-evolution catalysts based on high surface area Ni electrodes in alkaline media as low-cost alternatives that are better suited for large-scale H_2 generation [2, 5, 6].

Nickel-based electrode materials also find prominent use in a variety of other applications in science and engineering such as electrochemical sensors [7] and secondary battery electrodes [8]. Nickel is extensively used in electro-catalysts for diverse applications including oxygen evolution [9], the oxidation of organic compounds [10], methanogenic microbial electrolysis [11], and the electrochemical treatment of wastewater [12].

A problem Ni-based electrodes face is that the hydrogen evolution reaction (HER) activity of Ni cathodes is significantly greater on fresh electrodes than after several hours of electrolysis [13-18]. Determining the origin of this deactivation has proven difficult, primarily because the voltammetric behaviour of nickel electrodes in alkaline media had not been fully explained when I began the work for this thesis. During the course of the research project, I determined the cause of this electrode deactivation, examined the nature of the surface oxides

and hydroxides that form electrochemically on Ni electrodes, and fully assigned the voltammetric behaviour of Ni electrodes in alkaline media (chapter 4). However, it was first necessary to investigate nickel hydroxides, which are introduced in section 1.2.2.

Initially, I set out to establish an objective method to compare catalyst materials and conduct a comprehensive comparison of candidate electro-catalysts reported in the available literature. My goal was to separately consider surface area and chemical differences (*e.g.,* the presence of other metals such as Zn or Mo [19-21]) between catalysts. However, I discovered that there were no established methods to measure the electrochemically active surface area (A_{ECSA}) of Ni or Ni-based electrodes with reasonable accuracy and precision (see section 5.11). Therefore, I instead developed a new method to accurately measure the A_{ECSA} on Ni electrodes, which is the subject of chapter 5.

1.2. Electrode Materials

1.2.1. Nickel

Ni has a face-centred cubic (fcc) crystal lattice with unit cell parameter a = 3.5238 Å (Figure 1.1) [22]. Ni is a ferromagnetic metal below its Curie temperature of 357 °C and has a density of 8.90 g cm^{-3} at 25 °C [22, 23]. In general, Ni finds widespread use in engineering for its ability, when alloyed with other elements, to improve a metal's strength, toughness, and corrosion resistance over a wide range of temperatures [23]. In electro-catalysis, Ni is used as a low-cost alternative to noble metals, such as Pt and Pd (*e.g.*, [5]). Ni also has particular economic value for Canada. In 2012, Canadian mines produced 220,000 tonnes of Ni, which represents 10.5 % of global production [24].

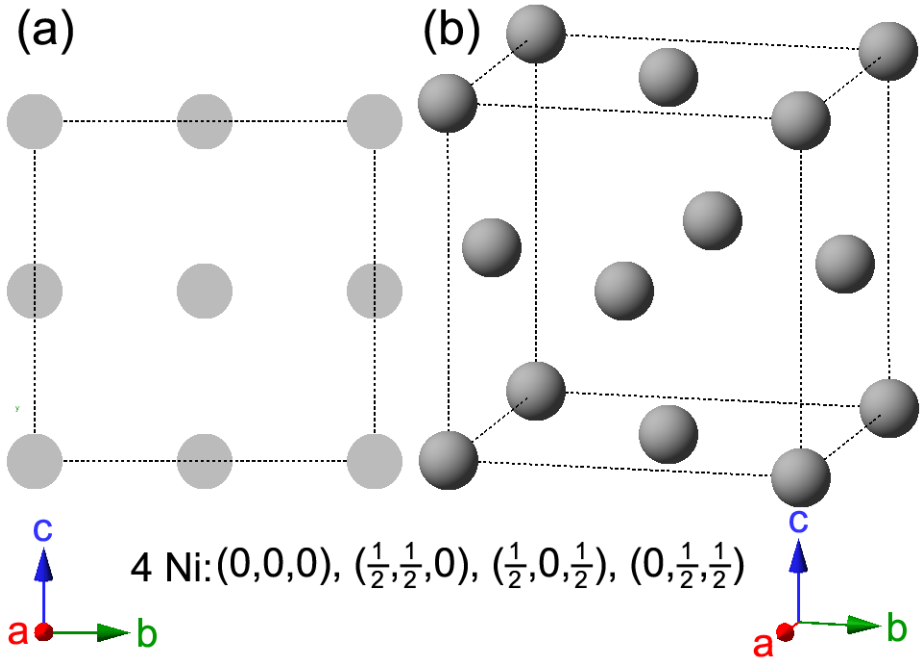

Figure 1.1 The crystal structure of Ni represented by (a) unit cell projection and (b) ball-and-stick unit cell. Grey = Ni.

1.2.2. Nickel Hydroxides

$Ni(OH)_2$ materials are important for many potential applications, including energy storage [25-36], electrochromic devices [37, 38], and photocatalysis [39]. In the field of corrosion science, $Ni(OH)_2$ components have been observed in electrochemically and air-formed surface layers on Ni metal [40-46], on many Ni-containing alloys [47, 48], and are often formed as the corrosion product in rechargeable batteries [8, 35]. In this thesis, I present the results of my investigations of $Ni(OH)_2$ materials and surface layers in chapters 2 and 3. The results of this work are applied to fully understand the voltammetric behaviour of Ni electrodes in alkaline media in chapter 4.

Bode et al. first identified the two known polymorphs of $Ni(OH)_2$, denoted α- and β-$Ni(OH)_2$ [26]. The β-phase material (Figure 1.2) is isostructural with brucite, $Mg(OH)_2$ [34], and naturally occurs as the mineral theophrastite [49, 50]. The unit cell parameters, measured by X-ray diffraction (XRD) [34, 51] and neutron diffraction [51, 52], are listed in Table 1.1.

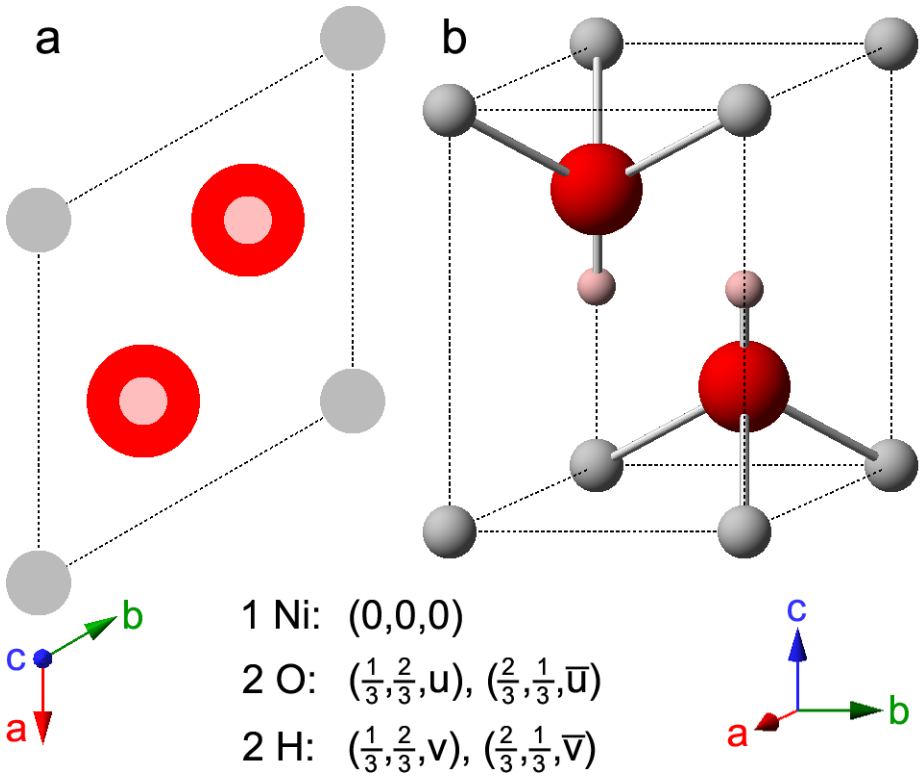

Figure 1.2 The crystal structure of β-$Ni(OH)_2$ represented by (a) unit cell projection and (b) ball-and-stick unit cell (u = 0.24 and v = 0.47 [51]; or u = 0.2221 and v = 0.4275 [52]). Grey = Ni^{2+}, red = O^{2-}, pink = H^{+}.

Table 1.1 Unit cell parameters for the two fundamental phases of $Ni(OH)_2$.

	β-$Ni(OH)_2$	β-$Ni(OD)_2$		α-$Ni(OH)_2 \cdot xH_2O$
	McEwen [34]	Greaves [52]		Pandya [53]
Space Group	$D_{3d}^3/P\bar{3}m1$/No. 164			$D_{3d}^1/P\bar{3}1m$/No. 162[a]
$\alpha = \beta$	90°			90°
γ	120°			120°
$a = b$	3.126 Å	3.126 Å	d_{Ni-Ni}[b]	3.08 Å
c	4.605 Å	4.593 Å		8.0 Å[c]

[a]The space group is for the idealized structure shown in Figure 1.3. However, the H_2O molecules do not actually occupy fixed lattice points and α-$Ni(OH)_2$ materials are always turbostratic. Therefore this is only a representative symmetry.

[b]The *a*-parameter of α-$Ni(OH)_2$ depends on the definition of the unit cell. The Ni–Ni spacing, however, may be directly compared to the *a*-parameter of β-$Ni(OH)_2$.

[c]The *c*-parameter may exceed this value if there are anionic impurities incorporated into the interlayer space.

The second polymorph of nickel hydroxide, α-$Ni(OH)_2 \cdot xH_2O$, consists of layers of β-$Ni(OH)_2$ intercalated by water molecules (Figure 1.3) [26]. The degree of hydration is variable, and has been reported for $0.5 \leq x \leq 0.7$ [34]. Typically, the water molecules are omitted from the formula, i.e., the material is denoted α-$Ni(OH)_2$. However, since water is intrinsic to the structure of the material, it should always be assumed to be present whenever the 'α' designation is used. Note that the representation of α-$Ni(OH)_2$ shown in Figure 1.3 is incorrect or, at the very least, a bit misleading [34, 35, 54]. This is because the intercalated water molecules are not fixed, but rather they have some freedom to rotate and translate within the plane defined by the crystallographic a- and b-axes (the ab-plane). If the water molecules had fixed positions that are close-packed with the hydroxide ions, as originally proposed by Bode et al [26], the c-parameter would be close to 7.6 Å. Rather, the observed value is ~8.0 Å, which corresponds well to water acting as an 'amorphous glue' that holds the $Ni(OH)_2$ layers together [34]. As a result, adjacent layers have little, or no, tendency to orient relative to one another. This random layer orientation motif is known as a 'turbostratic' structure [34, 55]. Furthermore, the interlayer spacing can be quite variable, where values as high as c = 13.2 Å have been reported for α-$Ni(OH)_2$ with large anionic impurities incorporated into the structure [56].

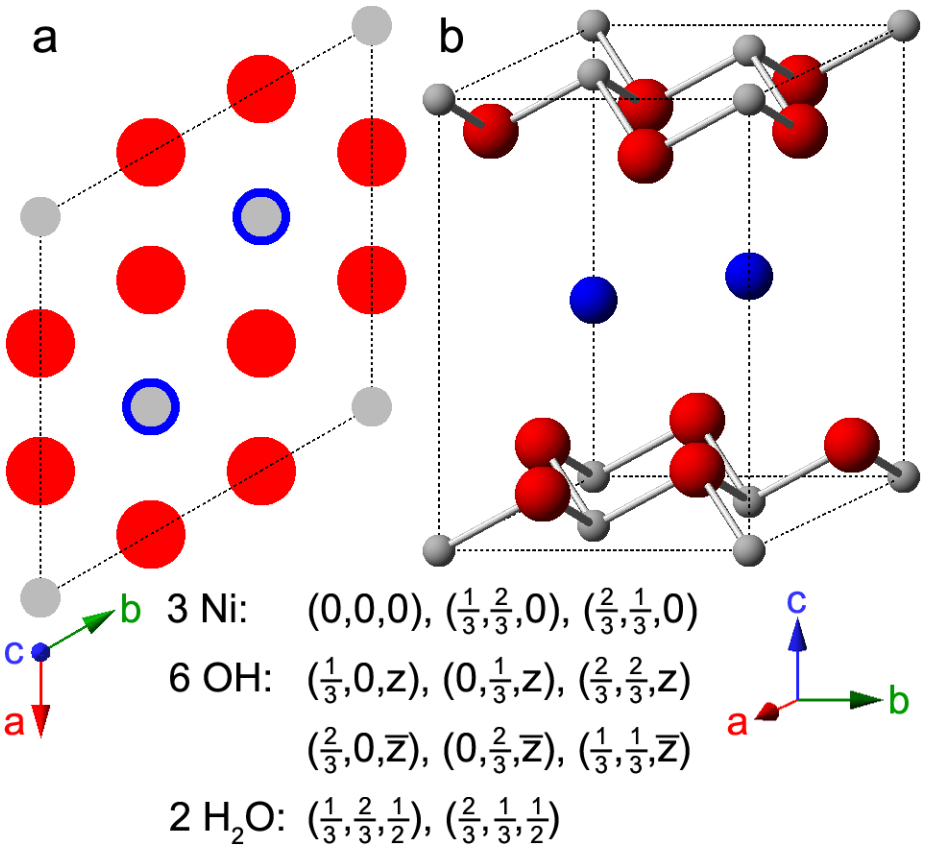

Figure 1.3 The idealized crystal structure of α-$Ni(OH)_2 \cdot xH_2O$ represented by (a) unit cell projection and (b) ball-and-stick unit cell for $x = 0.67$ (actual value varies, $0.5 \leq x \leq 0.7$). Grey = Ni^{2+}, red = OH^-, blue = H_2O.

It is known from extended X-ray absorption fine spectrum (EXAFS) measurements that there is a 0.05 Å contraction in the Ni–Ni distance ($d_{Ni–Ni}$) in α-$Ni(OH)_2$, relative to β-$Ni(OH)_2$ [53]. Therefore, the unit cell parameters for the idealized stoichiometry (3 Ni : 2 H_2O) shown in Figure 1.3 are a = b = 5.335 Å and c = 8.0 Å. Note that the a-parameter depends on the size of the unit cell chosen, which is defined by the degree of hydration. However, $d_{Ni–Ni}$ may be directly compared with the a-parameter of β-$Ni(OH)_2$ (Table 1.1). Further, the c-parameter will increase if there are anionic impurities incorporated into the interlayer space (see section 2.3.7).

The physical properties of the nickel hydroxides have been thoroughly investigated utilizing infrared spectroscopy (IR) [25, 28, 30, 31, 38, 57-65], Raman spectroscopy [29, 59, 66-76], extended X-ray absorption fine structure (EXAFS) [53, 67], inelastic neutron scattering (INS) [77], neutron diffraction [51, 52, 78] and more detailed XRD studies [34, 55, 68, 79]. However, the literature is complicated by the proposed existence of several additional phases and the numerous methods of denoting these materials that exist, including α_{am}, α*, α', IS and β_{bc} [35, 58, 80, 81]. These notations are used inconsistently between reports by different authors and are often ambiguous and redundant. The results presented in chapter 2 do not support the existence of these additional phases, but rather the two fundamental phases (α and β) with various types and extents of structural disorder.

Further investigation of these structures is merited because several studies have linked structural changes in $Ni(OH)_2$ electrodes and devices to their performance. As an example, the $Ni(OH)_2$/NiOOH redox pair is used extensively for the anodes of secondary alkaline batteries, including NiCd and NiMH [82], and it is generally agreed to be limited by electron and proton conductivities, which depend on the crystal microstructure [77]. It has been shown that the substitution of Ni sites with Co improves the charge capacity and proton conductivity of β-

$Ni(OH)_2$ electrodes. However, it cannot be conclusively stated whether this is due to increased proton vacancies or other structural defects [66, 67, 83]. In another example, the electrochromic efficiency and stability during electrochemical cycling of precipitated $Ni(OH)_2$ films were linked to the nickel salts used during preparation, although without further details of the structural differences, the authors were unable to determine the origin of the differences between samples [38]. This demonstrates the need for methods to measure the incorporation of anions from commonly used nickel salts, such as sulfate, chloride and nitrate, and separately examine other types of disorder, such as hydration and crystal defects. Such work will allow more systematic investigations of the link between structural changes and material performance.

Although impurities and defects can improve electrode performance they can also cause instability; for instance, α-$Ni(OH)_2$ is not currently used in battery applications because its charge capacity tends to decrease more rapidly on cycling than that of β-$Ni(OH)_2$ electrodes [66]. One can also consider, as an example, that the slow leaching of impurities could cause other problems, *e.g.* chloride anions initiate pitting corrosion of certain metals that may be used elsewhere in a device. Thus, methods to clearly identify different types of disorder and impurities in the different phases of $Ni(OH)_2$ will allow useful disorder to be incorporated while simultaneously deliberately avoiding problematic disorder that destabilizes the material.

It is clear that the effects of structural disorder can have very important practical consequences. However, the relationships between structural disorder and the experimentally measured properties are not always clear. Therefore, it is important that all possible forms of disorder should be considered when studying nickel hydroxides. The known types of disorder are briefly reviewed below.

1.2.2.1. Hydration

The hydration of β-$Ni(OH)_2$ materials is very important for electrochemical applications. The electrochemically active form of the material has a small amount of water in its structure. This hydrated form has been given the representation $[Ni(H_2O)_x](OH)_2$, where the degree of hydration has been measured in the range of $0.3 \leq x \leq 0.34$ [84] or $0.1 \leq x \leq 0.4$ [85]. The incorporated water is fully removed at high temperatures, T ≈ 160 °C [66, 84-86], which decreases the charge capacity of β-$Ni(OH)_2$ battery electrodes by about 10–14 %, relative to the hydrated form [31, 84]. The water molecules are weakly associated with the nickel cations and do not form hydrogen bonds with the lattice hydroxide [8, 30, 31, 84]. The presence of incorporated water increases the unit cell c-parameter by $\Delta c \approx 0.1$ Å [52]. It should be noted that this expansion may not be wholly attributable to hydration effects because the role of stacking faults (see 1.2.2.2) in these measurements is unknown. Incorporated water may be conclusively detected by the presence of additional O–H libration (bending) modes in the Raman and IR spectra [30, 31, 52, 66, 87] (see chapter 2 for details).

Water is intrinsic to the structure of α-$Ni(OH)_2 \cdot xH_2O$ and hydration should always be assumed to be present whenever the 'α' designation is used. Although the 'pure' material is generally reported as $0.5 \leq x \leq 0.7$, the exact degree of hydration is frequently quite variable and is strongly affected by the incorporation of foreign anions into the interlayer region between $Ni(OH)_2$ layers (see section 1.2.2.3). The hydration of α-$Ni(OH)_2$ materials is generally discussed with the underlying assumption that water is limited to the interlayer region. However, it has been suggested that water may also associate with the lattice Ni, similar to what is observed for hydrated β-$Ni(OH)_2$ materials [30, 85]. There is evidence that some α-$Ni(OH)_2$ materials have Ni–O coordination numbers greater than six, which supports this possibility [53].

1.2.2.2.Stacking Faults

The presence of stacking faults is common in layered double hydroxides (LDHs) [88]. This disorder may be understood by examining the unit cell of β-$Ni(OH)_2$ (Figure 1.2). There is strong ionic bonding between Ni^{2+}, O^{2-}, and H^{+} ions within the plane defined by the crystallographic a- and b-axes, whereas interactions between adjacent layers are relatively weak. Therefore, LDH materials consist of several 'stacked' layers. Consequently, in addition to the aligned thermodynamic product, illustrated in Figure 1.4a, one can propose three additional stacking motifs. The first arises from rotation about the c-axis by 60° (Figure 1.4b), the second from translation within the ab-plane (Figure 1.4c), and the last from both rotation and translation. For more information on stacking fault disorder in nickel hydroxides, the reader is referred to Tessier et al. [89] or, for a detailed and general discussion of stacking fault disorder, Sebastian and Krishna [90]. Stacking faults cause selective line-broadening in XRD patterns, because the disorder is only along the direction of the crystallographic c-axis (i.e., the ab-plane is still considered crystalline) [83, 89]. Stacking faults in β-$Ni(OH)_2$ materials may be measured by the appearance of additional O-H stretching modes in Raman and infrared spectra (see Section 3) [87]. It is meaningless to discuss stacking faults in α-$Ni(OH)_2$ because of its turbostratic structure (the layer orientation is always random).

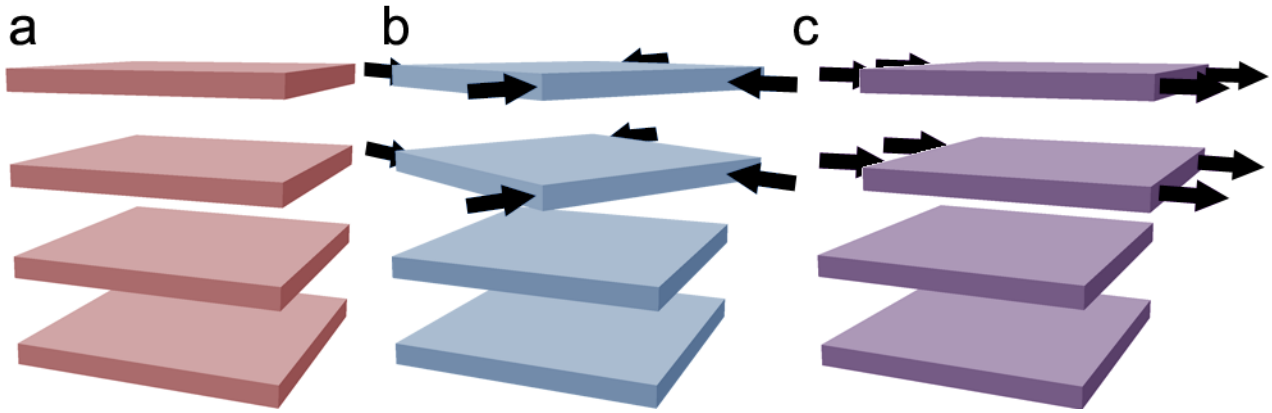

Figure 1.4 Schematic representation of stacking fault disorder between two adjacent layers. (a) No stacking faults are present and adjacent layers are aligned. (b) Rotation about the crystallographic c-axis. (c) Translation within the ab-plane.

1.2.2.3. Ionic Substitutions and Foreign Ion Incorporation

Substitutional point defects involve the substitution of a lattice atom (or polyatomic ion) with another. Numerous cationic substitutions of nickel hydroxides have been prepared from bivalent metal cations. These materials have the general formula $Ni_{1-x}M_x(OH)_2$, where M is the substituted metal atom. In the literature, there are examples of such point defects occurring as impurities during material preparation, such as the substitution of Ni^{2+} with Ca^{2+} ($Ni_{1-x}Ca_x(OH)_2$, $x \leq 0.02$ [87]). More extensive cationic substitution may occur with some metals, especially if there is an isostructural material, such as brucite, $Mg(OH)_2$, in which case a solid solution of any composition may be possible. Such solid solutions of β-$Ni(OH)_2$ and brucite have been used to correlate the vibrational modes of β-$Ni(OH)_2$ and $Mg(OH)_2$ [57].

β-$Ni(OH)_2$ materials have been prepared with cationic substitutions of the lattice Ni with Mg [57, 91], Al [92], Ca [87, 91], Co [66, 67, 83, 91, 93-95], Cu [91], Zn [91, 96, 97], and Cd [67, 95]. All of these materials maintain the space group of the parent β-phase material, although generally with slightly modified unit cell parameters. For example, the interplanar spacing, *c*, decreases with increasing Co content [94]. However, this may not be purely a result of the different cationic radii, since these substitutions are often accompanied by other structural disorder, such as increased or decreased stacking fault disorder [83].

α-$Ni(OH)_2$ materials have also been prepared with cationic substitutions of the lattice Ni with Al [92, 98-104], Mn [105], Fe [106, 107], Co [103, 104, 108-110], Cu [98, 111], Zn [96, 97, 100, 112, 113], Y [114], and Yb [115]. For some of these examples, the bivalent Ni^{2+} cation is replaced with a trivalent species (*e.g.*, Fe^{3+}). Therefore, the resulting materials must be hydroxide-rich, proton-deficient or there is a corresponding degree of anionic incorporation (*e.g.*,

carbonate anions in Ref. [107]) to maintain charge balance. The incorporation of foreign anions into α-$Ni(OH)_2$ is further discussed below.

$Ni(OH)_2$ materials have also been isotopically enriched by treatment with D_2O, which is another form of cationic substitution. Deuterated materials have been used to perform crystallographic studies of β-$Ni(OD)_2$ [52] and to definitively identify O–H and O–D stretching modes in the IR spectra of β-$Ni(OH)_2$ and β-$Ni(OD)_2$ materials, respectively [31, 62, 78]. Deuterated materials have also been used for crystallographic and IR spectroscopic investigations of α-$Ni(OH)_2$/α-$Ni(OD)_2$ [78].

It is also possible to incorporate foreign anions during nickel hydroxide synthesis. During precipitation from a nickel(II) salt, it is quite common that some of the counterions used to prepare the material are incorporated into the structure. This is especially important for α-$Ni(OH)_2$, in which anions may either occupy a lattice hydroxyl site or rest within the intersheet water region [87, 116]. The extent of this anion incorporation can be considerable and the resultant material may be generally represented by the formula $Ni(OH)_{2-x}A_yB_z \cdot nH_2O$, where A and B are monovalent and divalent anions, respectively, and $x = y + 2z$ [56]. The most common foreign anion is nitrate, because $Ni(NO_3)_2$ is widely used as a precursor to prepare nickel hydroxide materials [35, 117]. Samples have also been prepared containing chloride, sulfate, carbonate, cyanate, acetate, succinate, glutarate, and adipate anions [56, 87, 118, 119]. Incorporated anions may either occupy lattice hydroxide sites or they may sit within the interlayer region. The former tends to be less stable, likely due to mechanical stresses from the size mismatch. In contrast, anions in the intercalation region tend to be more stable and have very similar spectroscopic properties to the free solution species. In the field of intercalation chemistry, the thickness of the interlayer space is known as the ‘gallery height’ [120].The

presence of foreign ions in the interlayer space can increase the gallery height and, consequently, the interlayer spacing. For example, the interlayer spacing of α-$Ni(OH)_2$ containing nitrate or carbonate is typically 8.0 Å ≤ c ≤ 8.2 Å, whereas the spacing of α-$Ni(OH)_2$ that contains the larger anion adipate, $[(CH_2)_4(CO_2)_2]^{2-}$, has been reported as high as c = 13.2 Å. This is a 65 % expansion from the parent structure [56]. Presumably the increased gallery height causes the degree of hydration of these materials to increase as well by the incorporation of additional water molecules into the expanded interlayer space.

In general, the incorporation of foreign anions into β-$Ni(OH)_2$ materials is less common than it is with the α-phase because adjacent layers are close-packed. Further, foreign anions are quickly removed during the aging process (the conversion of α- to β-$Ni(OH)_2$, see chapter 3) [87, 116]. Nevertheless, anionic substitution of the lattice hydroxide is possible. For example there is electrochemical evidence that sulfide anions have been incorporated into $Ni(OH)_2$ materials [121]. It is unknown which phase of $Ni(OH)_2$ was produced or whether the substituted anionic species was S^{2-} or SH^-.

1.2.2.4. α/β-Interstratification

One can consider a single grain or crystal of nickel hydroxide in which some of the layers are separated by intercalated water (α), whereas the rest are not (β). Such materials have been studied by Rajamathi *et al*, who noted the absence of the expected (001) XRD lines, which should correspond to the stacking of layers (*cf.* $c_\alpha \approx 8.0$ Å, $c_\beta = 4.6$ Å) [122]. They described these materials as 'interstratified phases consisting of α- and β-type structural motifs' and conclude that they are not simple mixtures of α-$Ni(OH)_2$ and β-$Ni(OH)_2$ crystals [81, 122]. Rather, the presence of interstratification allows α- and β-$Ni(OH)_2$ domains to coexist within a

single crystal. These domains may hypothetically be as little as a single layer. Consequently, the long-range structural order along the c-axis, required for diffraction measurements, does not exist in interstratified materials. However, it should be noted that vibrational spectra collected from the interstratified materials reported in Ref. [81] still contain the characteristic α and β O–H internal stretching modes discussed in chapter 2.

1.2.2.5. Internal Mechanical Stress

There are several causes of internal mechanical stress. For example, the insertion of large polyatomic anions, such as nitrate, into the lattice sites or the intercalation space of α-$Ni(OH)_2$ is expected to introduce mechanical stress. In chapter 3 of this thesis, I present Raman spectroscopic evidence of internal stresses during the chemical transformation of α-$Ni(OH)_2$ to β-$Ni(OH)_2$. This is explained in terms of the changing unit cell c-parameter (8.0 to 4.6 Å). The result is compressive and tensile forces along the c-direction of the α- and β-phases, respectively [116]. There is also evidence of mechanical stress in the vibrational spectra of dried nickel hydroxide films. In addition to the shifted lattice modes, the films are visibly cracked, showing that the removal of water changes the compactness of the materials, which gives rise to internal stress at a large scale (see section 2.2.4) [87]. Mechanical stresses also occur during the oxidation and reduction of nickel hydroxides to and from nickel oxyhydroxides, because of the differences in lattice parameters [35, 123].

1.2.2.6. Synthesis of $Ni(OH)_2$ Materials

There are several synthetic methods for the preparation of α- and β-$Ni(OH)_2$, either as bulk materials or as thin surface layers. α-$Ni(OH)_2$ may be prepared in bulk quantities by

homogeneous chemical precipitation (Figure 1.5a) [34, 35] or deposited as a thin layer on a conductive substrate by electrochemical precipitation (Figure 1.5b) [34, 117, 124]. I used the latter method to prepare the α-$Ni(OH)_2$ samples for chapters 2 and 3. A wide variety of micro- and nano-scale structured α- and β-$Ni(OH)_2$ materials may be prepared by sol-gel synthesis (Figure 1.5c), *e.g.*, [125-128]. High purity β-$Ni(OH)_2$ materials may be produced by chemical aging (Figure 1.5d, see chapter 3). Micro- and nano-scale structured β-$Ni(OH)_2$ may be produced by hydrothermal synthesis (Figure 1.5e), *e.g.*, [119, 129, 130]. Nickel hydroxides are also important surface components of surface layers formed electrochemically (see section 4.3.2) or during the corrosion of nickel metal and nickel-based alloys (Figure 1.5f), *e.g.*, [40-48].

In this thesis, standard $Ni(OH)_2$ materials were prepared for spectroscopic analysis by electrochemical precipitation (α-$Ni(OH)_2$) and by chemical aging the electrochemically precipitated films (β-$Ni(OH)_2$) in chapters 2 and 3. $Ni(OH)_2$ surface layers were also formed electrochemically on metallic electrodes during the voltammetric experiments presented in chapters 4 and 5.

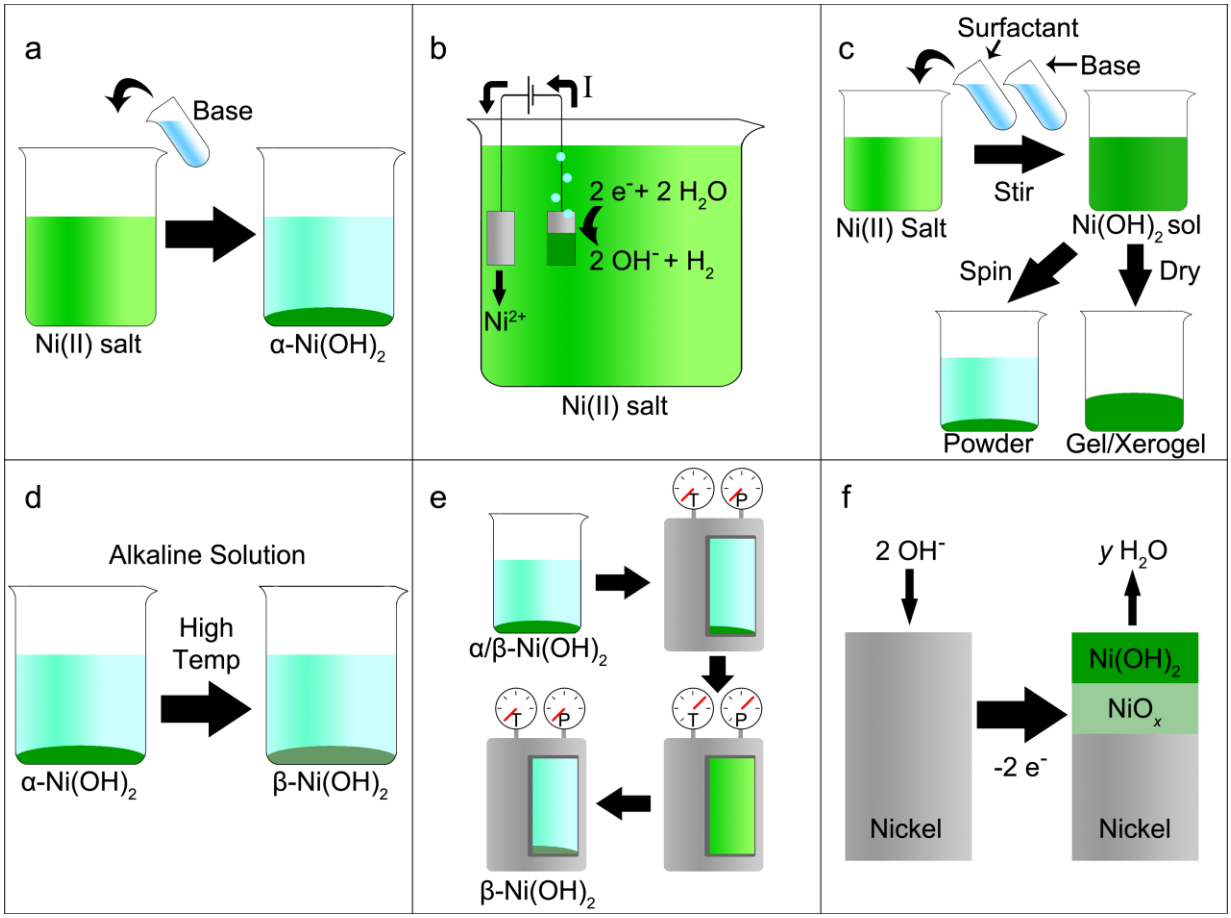

Figure 1.5 Six methods of preparing $Ni(OH)_2$. (a) Basification of a nickel(II) salt solution (e.g., by addition of $NH_{3(aq)}$ to $NiCl_{2(aq)}$) produces α-$Ni(OH)_2$ precipitate. (b) Electrochemical precipitation deposits α-$Ni(OH)_2$ onto a conductive substrate. The reduction of water produces hydroxide anions at the cathode surface, which react with the Ni(II) cations in solution. In this example, the anode material is a Ni sheet. (c) Sol-gel methods produce α/β-$Ni(OH)_2$ particles or porous materials. A solution of a Ni(II) salt and a surfactant (*e.g.*, sodium dodecylsulfate) is basified to form a $Ni(OH)_2$ sol (colloidal suspension). Nanoparticles may be collected by centrifugation or the solvent may be evaporated to produce a gel/xerogel. (d) Chemical aging converts α-$Ni(OH)_2$ to β-$Ni(OH)_2$. This is typically performed in concentrated alkaline media at high temperatures, but also proceeds slowly in room temperature water. (e) The hydrothermal method produces highly crystalline β-$Ni(OH)_2$, often with unique nanoscale structure. α/β-$Ni(OH)_2$ precursor is dissolved in a pressure vessel at very high temperatures. The temperature is subsequently decreased and β-$Ni(OH)_2$ precipitates. (f) α/β-$Ni(OH)_2$ surface layers form on nickel metal and nickel-based alloys as corrosion products and during electrochemical treatments, typically over an underlayer of non-stoichiometric nickel oxide.

1.2.1. Nickel Hydrides

H_2-evolution catalysts based on high surface area Ni electrodes in alkaline media are low-cost alternatives that are better suited for large-scale H_2 generation [2-5]. However, the HER activity is significantly greater for fresh Ni cathodes than it is after several hours of electrolysis [13-18]. This gradual decrease of the HER activity with time has been suggested to arise from the formation of a nickel hydride sub-surface or bulk phase [16-18, 131], similar to what is observed in acidic media [132]. The formation of a hydride phase would change the electronic band structure, lower the density of states near the electrode surface and, hence, would explain the lower HER activity [17, 18].

The electrochemical formation of nickel hydrides has been discussed extensively [18, 133-137]. However, aside from the work presented in chapter 4 of this thesis, there is only one published report that provides direct evidence of electrochemically formed nickel hydride in alkaline media. Soares *et al.* detected small amounts of β-NiH_x by X-ray diffraction (XRD) after they applied large cathodic currents (-0.3 A cm^{-2}) to nickel in concentrated electrolyte solutions (30 % [w/w] KOH) [18]. Because of the limited direct evidence of nickel hydride formation, Baranowski argued that only small amounts of nickel hydride can be formed in alkaline media, which further requires the use of high currents and very high pH electrolytes [133]. Moreover, there are alternate explanations for the deactivation, including the Rowland effect, which is the deposition of impurities from the solution onto the electrode surface. There is evidence that this effect can contribute to electrode deactivation and the addition of EDTA to the electrolyte can greatly reduce or entirely eliminate the deactivation [138-140] However, other authors have reported that the Rowland effect's role in electrode deactivation is quite minor [16, 18].

Therefore the formation of nickel hydrides and the origin of Ni cathode deactivation have remained uncertain.

It is important to note that the term 'nickel hydride' may have a variety of meanings that span the dimensional and energetic sequence: (1) A point hydride, a single surface or lattice defect; (2) a line hydride, a one-dimensional hydride on a crystal edge; (3) a surface hydride, a two-dimensional hydride on a crystal surface; (4) a sub-surface hydride, a three-dimensional hydride formed to a limited depth or thickness; and (5) a bulk hydride, a three-dimensional hydride [133]. When studying electro-catalysts for the HER, surface hydrides ($Ni\text{-}H_{(ads)}$) are a very important intermediate species. In general, the strength of the M-H surface bond on a given electro-catalyst determines the exchange current density and the kinetic pathway [141].

There are two phases of bulk nickel hydride, α and β, which draw their nomenclature from the palladium hydrides [142]. β-NiH_x has a fcc lattice structure with the H atoms in the octahedral sites (Figure 1.6) and $x = 0.6 \pm 0.1$ [143]. The β phase lattice parameter is ~6 % greater than that of Ni metal [143, 144]. The lattice parameter of α-NiH_x is only slightly expanded relative to Ni metal (less than ~1 %). Although there is no neutron data available for α-NiH_x, the lattice expansion supports the general belief that it is isostructural with α-PdH_x, which has been studied more extensively and for which $x \leq 0.03$ [145, 146]. The H atoms in α- and β-PdH_x occupy the octahedral interstitial sites of the fcc Ni structure (Figure 1.6) [143-146].

In this thesis, it is found that the incorporation of hydrogen into the electrode material can also affect the electrocatalytic activity. Therefore, bulk hydrides feature in the results and discussion of chapter 4.

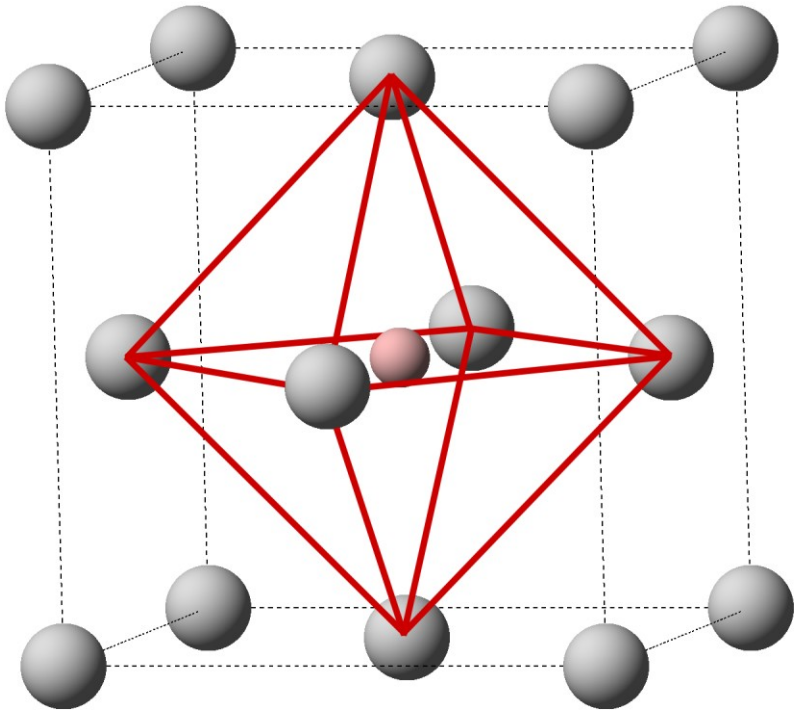

Figure 1.6 The H atoms in α- and β-NiH_x materials occupy octahedral interstitial sites.

Grey = Ni, pink = H.

1.3. Electrochemically Active Surface Area (A_{ECSA}) Measurements

In general, the measured activity of an electro-catalyst is determined by three factors: (1) its catalytic properties, i.e., the reaction pathway and the activation energies of each step, (2) its electrochemical surface area (A_{ECSA}), and (3) whether the system is under mass-transfer control. The catalytic properties are determined by chemical factors such as the atomic spacing and the electronic structure at the electrode surface. The A_{ECSA} is the interfacial surface area that is available for a pure Faradaic reaction that is activation-controlled. For the purposes of electro-catalyst design, mass-transfer limitations may be ignored, since these are engineering problems that arise during cell construction. Therefore, it is desirable to have an objective method to compare electro-catalysts such that chemical and surface roughness effects may be examined separately. The simplest approach is to first measure the A_{ECSA} values of different catalysts and then divide this by their geometric areas to find the surface roughnesses [147]. Since the electrode activities are directly proportional to A_{ECSA}, the catalytic properties of candidate materials may be compared by dividing the measured activity of each by the corresponding A_{ECSA} values to obtain the real current densities (*e.g.*, Ni_xZn_y [19] and Ni_xMo_y [20, 21]). However, this first requires a method to accurately measure A_{ECSA}.

The preparation of high surface area nickel electrodes has been an area of study for several decades [148]. Real surface area measurements in electrochemical systems are typically performed using one of the methods outlined by Trasatti and Petrii, who describe in detail eleven *in situ* and four *ex situ* techniques [147]. However, the application of these methods can pose experimental challenges, especially for non-noble-metal electrodes such as nickel. Several methods have been used previously to estimate the surface area of nickel electrodes, including the voltammetric formation of a surface oxide/hydroxide layer [131, 149], the measurement of

the electrochemical double layer capacitance (C_{dl}) by electrochemical impedance spectroscopy (EIS) [150, 151]. and by measuring the Faradaic desorption of a surface intermediate [152]. However, all of these methods involve initial assumptions or estimations that limit the confidence of the calculated A_{ECSA}.

Machado and Avaca assumed that the anodic peak at ~0.3 V vs. the reversible hydrogen electrode (RHE) during a forward voltammetric sweep on metallic nickel corresponds to the formation of a monolayer of α-$Ni(OH)_2$ [131]. It has since been shown that the primary surface component formed at this potential is indeed α-$Ni(OH)_2$. However, the exact thickness of this surface layer has never been determined. Further, non-stoichiometric NiO_x also forms in this potential region and the voltammetric behaviour as a whole is heavily dependent on the electrode history and pretreatment [40]. Therefore, this method yields only an approximate surface area with limited accuracy and precision.

Shervedani and Lasia utilized the adsorption of solution CO to evaluate the surface area of nickel electrodes [153]. In this method, CO is bubbled into the electrolyte solution for 25 min and then the electrode is transferred to a deaerated solution for testing. The adsorbed CO ad-layer is then removed by oxidative stripping voltammetry. It is assumed that there is one CO molecule for each surface Ni atom. However, the voltammetric peak overlaps with the oxidative formation of α/β-$Ni(OH)_2$ and NiO_x. Consequently, the peak is not well-resolved and the background current must be estimated. Furthermore, the exact thickness of the surface oxide/hydroxide is not exactly known. Nevertheless, this method yields a sharper peak than the previous method and is therefore a more precise strategy.

In contrast to the previous two methods, the C_{dl} of an electrode may be measured with high precision, either by electrochemical impedance spectroscopy (EIS) or by cyclic

voltammetry (CV) over a small potential window slightly below the RHE potential [153]. Both methods also have the advantage of being non-destructive. This is in contrast to the methods in the previous two paragraphs, which require the formation of surface nickel oxides and hydroxides. These surface species may not fully reduce back to metallic nickel [40, 151]. However, the exact value of this capacitance is potential-dependent [151, 154]. Furthermore, the C_{dl} of a planar nickel electrode is unknown and therefore must be estimated. Estimated reference values range from 20 – 25 μF cm^{-2}, for metallic electrodes [150, 151, 153, 154], and 40 – 60 μF cm^{-2} for oxide covered electrodes [155, 156]. Therefore, the accuracy of surface areas calculated from the double-layer capacitance are questionable, with large associated uncertainties. For example, Bockris and Otagawa estimated their experimental uncertainty at ± 100 % [155]. As a cautionary note, it is also important to correct for dispersion effects when using EIS [157]. An experimentally measured constant-phase element (CPE_{dl}) may, however, easily be transformed to the corresponding C_{dl} by utilizing the method of Brug et al [158].

Another method used to measure A_{ECSA} values on nickel electrodes involves the measurement of adsorbed hydroxide species formed in the Ni(III) potential region [156]. First, an anodic charging current is applied to form Ni(III) oxyhydroxide. This reaction is reported to proceed via an adsorbed surface intermediate, $[Ni(III)O_m(OH)_{n+1}]^{p-}{}_{(ads)}$. Next, the charging current is interrupted and a transient cathodic current is measured, which is proposed to correspond to the desorption of the intermediate species via the reaction [152]:

$$[Ni(III)O_m(OH)_{n+1}]^{p-} + H_2O + 2e^- \rightarrow [Ni(II)O_{m-1}(OH)_{n+1}]^{p-} + 2OH^- \qquad \textbf{(1)}$$

(4The total transient charge, Q_{decay}, is plotted against the overpotential from the anodic charging step, η_{charge}. At sufficiently high η_{charge}, Q_{decay} reaches a plateau because the fractional surface coverage of the intermediate approaches unity ($\theta \rightarrow 1$). Therefore, the limiting Q_{decay} corresponds to desorption of a monolayer of the adsorbed species. By estimating the charge for a

smooth electrode, one obtains an estimated maximum Q_{decay} of 420 μC cm^{-2}. The authors clearly state that this reference value is merely a reasonable "universal accepted standard," which may be used to obtain approximate surface area estimates [152, 156]. In addition to the limited accuracy of this reference value, it is also imprecise between measurements because there are two possible oxyhydroxides of nickel, β- and γ-NiOOH, with different unit cell parameters and symmetries [34]. The amount of each at the electrode surface is dependent on the electrode preparation and treatment [8, 26]. Furthermore, it has been shown that the formation and subsequent reduction of a nickel oxyhydroxide surface layer, necessary for this A_{ECSA} measurement method, can change the surface roughness of metallic nickel [40]. Therefore, this method is unsuitable for metallic electrodes and catalysts. However, it is particularly useful for measuring the surface area of oxidized nickel surfaces, such as battery anodes and electro-catalysts for oxygen evolution. Therefore, the current transient decay method is perhaps the best approach developed to date for surface area measurements of nickel electrodes.

During this thesis, I set out to develop a new method to measure the surface area of nickel electrodes, *in situ*, with improved accuracy and precision. In chapter 5, a novel approach is presented that utilizes the addition of solution oxalate and the measurement of a surface-limited process with highly unusual voltammetric characteristics.

1.4. Thesis Objectives

The overall goal of this research is to develop better methods of testing Ni-based electro-catalysts, especially for applications in electrolytic hydrogen production. Over the course of the research project, I focused on addressing a fundamental lack of understanding regarding the voltammetric behaviour of nickel in alkaline media. I also developed a new way to accurately

measure the A_{ECSA} of Ni electrodes to allow for more rigorous comparison of Ni-based electro-catalysts. However, it was first necessary to understand the nickel hydroxide surface layers that form electrochemically on nickel. As a result, this project is divided into two principal branches: vibrational spectroscopy and electrochemistry. Nevertheless, the work is highly interlinked and each chapter draws from one or more of the preceding sections.

The chapter numbers and corresponding research objectives are:

2. Develop methods to fully characterize nickel hydroxide materials
3. Develop and test practical methods to characterize nickel hydroxide materials and surface layers during chemical and electrochemical treatments
4. Determine the source of Ni-based HER electro-catalyst de-activation and fully assign the voltammetric behaviour of Ni in alkaline media
5. Develop a method to measure the electrochemically active surface area of Ni electro-catalysts with high accuracy and precision

2. Raman and Infrared Spectroscopy of α and β Phases of Nickel Hydroxide

The contents of this chapter were adapted from the following peer-reviewed journal article [87]:

Hall, D.S., Lockwood, D.J., Poirier, S., Bock, C. & MacDougall, B.R. 2012 Raman and Infrared Spectroscopy of α and β Phases of Thin Nickel Hydroxide Films Electrochemically Formed on Nickel. J. Phys. Chem. A 116, 6771-6784. (doi:10.1021/jp303546r).

2.1. Introduction

The introduction of such terms as “active/de-activated α” and “active/de-activated β” to describe $Ni(OH)_2$ electrodes demonstrates a lack of knowledge about both of these phases and reaffirms their practical importance [80]. A more complete description of the two main phases of $Ni(OH)_2$ and any intermediates will be invaluable to research focused on applied $Ni(OH)_2$ electrochemistry. The ability to measure and, ultimately, to control the types of disorder present in an electrode or catalyst material will allow for the optimization of its performance, as determined by charge capacity, electrochromic efficiency, or catalytic activity, while simultaneously enabling improvements in the long-term stability of an electrode or device.

Therefore, the work presented in this chapter utilizes Raman and IR vibrational spectroscopy and uses modern instruments that offer higher resolution and sensitivity than previously reported, supported by XPS and fixed incidence XRD measurements, to re-examine the fine structural details of $Ni(OH)_2$. It is from the combination of these four analytical techniques with a review of previous studies that a comprehensive, yet simplified, model of $Ni(OH)_2$ is presented that considers its possible phases, incorporation of impurities and structural disorder. For example, XRD patterns are used to rationalize the appearance of additional, and previously unidentified, stretching modes in the Raman and IR spectra of β-$Ni(OH)_2$. As another example, Raman and IR peaks are used to identify at least two distinct chemical environments of nitrate anions incorporated as impurities in α-$Ni(OH)_2$ materials. Finally, this study identifies and assigns, for the first time, all of the lattice modes of β-$Ni(OH)_2$ using factor group analysis and summarizes the known Raman and IR peaks for both α and β-$Ni(OH)_2$.

2.2. Experimental Methods

2.2.1. Material Preparation

Metallic Ni foil (Alfa Aesar, ≥ 99 %, 0.127 mm) electrodes (1 cm × 2 cm) were attached to Ni wire (Alfa Aesar, 99.9 %, 0.065 mm diameter) by electric arc welding. The wire and one end of the electrode were covered with Teflon tape. The Ni foil substrates were washed with acetone and ethyl alcohol before sonicating them in high purity water (Millipore MilliQ, 18.2 MΩ cm). Immediately after, the substrates were cleaned in an acid bath (50 % acetic acid, 30 % phosphoric acid, 10 % sulfuric acid, 10 % nitric acid, 85 ºC) for 30 s then rinsed again with excessive amounts of high purity water.

Ni hydroxide films were formed by the conditions and treatments listed in Table 2.1. A Ni wire (~10 cm long) served as a counter electrode. Electrochemical treatments were performed using a Solartron Analytical 1470E multistat controlled with MultiStat software (v. 1.5a, Scribner Associates Inc.). Deposition solutions were prepared from $NiSO_4 \cdot 6H_2O$ (Alfa Aesar, ≥ 98 %), $NiCl_2 \cdot 6H_2O$ (J.T. Baker, assay = 100.7 %) and $Ni(NO_3)_2 \cdot 6H_2O$ (Alfa Aesar, ≥ 98 %). All solutions were prepared with high purity water. Solution concentrations were selected for efficient precipitation based on reported studies [117]. The current density and deposition times were selected to form α-$Ni(OH)_2$ films generally sufficiently thick to be identified by the spectroscopic methods (~5 μm, see section 2.2.4). Aging solutions were prepared from KOH pellets (Fisher Scientific, ACS certified).

Table 2.1 Methods used for sample preparation.

Sample	Start Material	Current Density	Time	Solution	Temperature
		mA cm^{-2}			°C
α_1	Substrate	-2.5	10 min	0.1 M $NiSO_4$	22
α_2	Substrate	-2.5	10 min	0.1 M $NiCl_2$	22
α_3	Substrate	-2.5	2 min	0.1 M $Ni(NO_3)_2$	22
β_1	α_1	N/A	185 h	30 % KOH	90
β_2	α_2	N/A	185 h	30 % KOH	90
β_3	α_3	N/A	185 h	30 % KOH	90
α/β	α_2	N/A	140 h	Water	22

Sample α_1 was prepared in duplicate and each sample was analyzed by XRD, XPS, Raman spectroscopy and FT-IR spectroscopy and to confirm reproducibility in the sample preparation and measurement methods. Sample α_3 was also prepared twice and each sample was analyzed by XPS, Raman and FT-IR spectroscopy to further confirm reproducibility. Samples β_1, β_2 and β_3 were stored in high purity water after aging in base and were dried immediately before analysis. The preparation methods for the β-phase samples were considered to be well-controlled and reproducible because the α-phase samples were found to be reproducible and the measurements for the three β-phase samples gave similar results.

2.2.2. X-Ray Diffraction (XRD)

Samples were analyzed using a Bruker AXS D8 DISCOVER diffractometer. Fixed incidence (5°) measurements were taken at 0.02° point^{-1} and 3 s point^{-1} using a Cu Kα X-ray source (λ = 1.54 Å). Data were smoothed for presentation with a 10-point, second order Savitzky-Golay filter.

2.2.3. X-Ray Photoelectron Spectroscopy (XPS)

Samples were analyzed with a Kratos Analytical Axis Ultra DLD equipped with a mono Al Kα X-ray source. Survey spectra, used for elemental quantification, were collected at 160 eV pass energy, and high-resolution spectra of the Ni 2p and the C 1s regions were collected at 20 eV pass energy. All spectra were collected at a 54° take-off angle. Spectra were processed with CasaXPS (v. 2.3.16dev95, Casa Software Ltd.) using Shirley backgrounds and the Ni 2p peak positions and widths for β-$Ni(OH)_2$, NiO and Ni metal reported by Biesinger *et al.* The elemental relative sensitivity factors (RSF) provided by Kratos Analytical were used for elemental

quantification. Measured binding energies were adjusted to compensate for the shift that arises from a buildup of electrostatic charge by setting the adventitious hydrocarbon C 1s peak to the binding energy 284.8 eV [159].

2.2.4. Raman Spectroscopy

The Raman measurements were performed at room temperature (22 °C) employing 1 mW of 457 nm laser light (Cobalt Twist diode-pumped solid state laser) for excitation in a backscattering geometry using the confocal microscope with a 100× objective on a Jobin-Yvon T64000 triple spectrometer operated in the subtractive mode and equipped with a back-illuminated Si charge-coupled-device detector. The sample surfaces, in general, were not planar comprising flatter areas surrounded by hilly areas. The laser beam diameter (~0.8 μm) was sufficiently small to lie within these regions and so measurements were made in three areas on each sample: A flatter area, a hilly area, and an area combining both topological areas. Generally, the features observed in each spectrum were the same for all areas, but the hilly regions gave the strongest signal consistent with their greater film thickness (~1 μm higher than the flatter areas). From depth dependent measurements of the Raman intensity in flatter areas using the confocal feature of the Raman microscope, the $Ni(OH)_2$ film thicknesses were estimated to be ~5 μm. Some of the samples exhibited irregular cracks in the film (see for example, Figure 2.1) that were probably introduced by stress during drying of the films. These cracks, which could reach down to the Ni substrate, were avoided during Raman measurements. Data were smoothed for presentation with a 25-point, second order Savitzky-Golay filter.

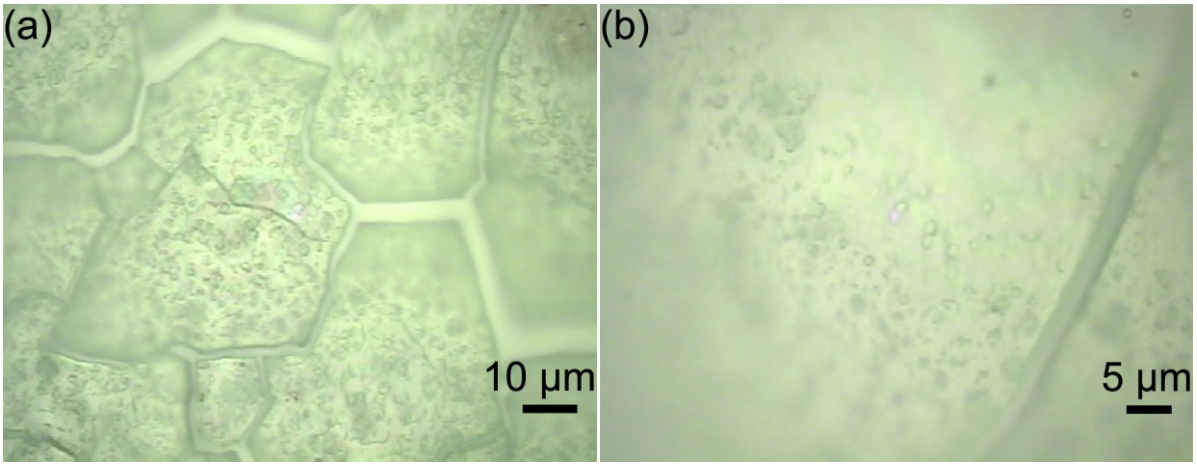

Figure 2.1 Photographs taken through the Raman microscope objective with objectives of (a) 50× and (b) 100× showing the cracked and bumpy nature (hence the fuzzy focus in regions of different height) of the $Ni(OH)_2$ film for sample α_3.

2.2.5. Fourier Transform Infrared (FT-IR) Spectroscopy

The infrared measurements were performed at room temperature in a nitrogen-purged sample chamber using a Bruker Hyperion microscope with a 15× objective on a Bruker Tensor 27 FT-IR operated in the reflective mode and equipped with a mercury cadmium telluride (MCT) detector. The light diameter was several millimeters and, thus, included both topological areas described above. An untreated substrate was used to set the instrument zero. Spurious peaks arising from H_2O and CO_2 in the sample chamber were removed from the spectra with OPUS software (v.4.2, Bruker Optik GmbH).

2.3. Results and Discussion

2.3.1. X-Ray Diffraction Patterns

All measured XRD patterns show three intense peaks that arise from the metallic Ni substrate, thus indicating that the X-rays penetrate the entire film (Figure 2.2). The relative intensities of the Ni metal (220) peaks in the β-$Ni(OH)_2$ samples are much weaker than for the α films. This indicates that the transmission at this angle is greater for the α than for the β films, implies that the β films are more crystalline than the α films and, from the relative intensities between samples, qualitatively shows that the sample thickness is $\beta_1 > \beta_2 > \beta_3$. The patterns from the β-$Ni(OH)_2$ films show all the expected peaks for this phase [51]. The (100) peaks are sharper than the (001) and (101) peaks, which indicates that there is greater order within the ab-plane than along the c-direction. This observation, with the layered structure of β-$Ni(OH)_2$, implies stacking faults of uniform $Ni(OH)_2$ sheets. From the full width half maxima of the (100) peaks, the β-films have similar crystallinity within the ab-plane, whereas the disorder in the c-direction is greatest for sample β_3 and least for sample β_1. The weak, broad diffraction peaks in the α-

$Ni(OH)_2$ samples demonstrate that these are highly disordered films, which is expected from previous studies that report similar diffraction patterns for α-$Ni(OH)_2$ [34]. Only the Ni substrate was clearly observed in the XRD pattern for sample α_1, because the samples were thinner and had a high degree of structural disorder.

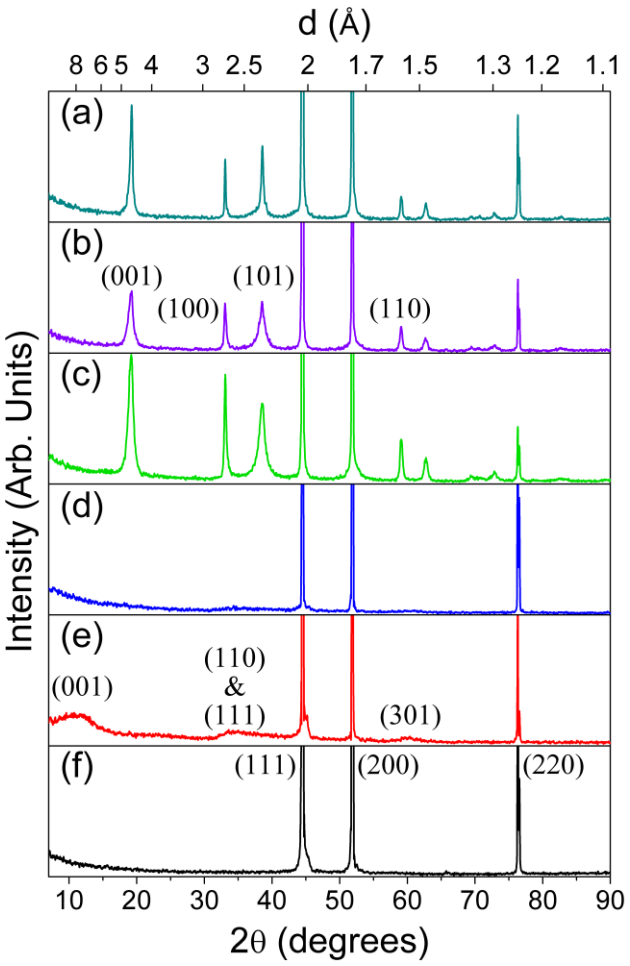

Figure 2.2 Diffraction patterns for samples (a) β_1, (b) β_2, (c) β_3, (d) α_2 (e) α_3 and (f) Ni metal substrate with the Miller indices for the first diffraction peaks of each material identified. All patterns are plotted on the same intensity scale. A Cu Kα X-ray source was used.

2.3.2. X-Ray Photoelectron Spectra

The XPS measurements of samples β_1, β_2 and β_3 (Figure 2.3a) agree well with reported β-$Ni(OH)_2$ spectra [159]. Sample β_1 shows that some K (~2 %) from the KOH aging solution remained on the surface. β_2 is pure and β_3 contains a small amount of Ca (~0.7 %), likely from impurities present in the $Ni(NO_3)_2$ salt used to deposit this film. Sample α_3 was prepared twice and Ca was detected in only one of the films (~0.2 %). Sample α_1 contains S (~2 %), α_2 contains Cl (~2%) and sample α_3 contains N (~3 %). This suggests that impurities, *i.e.* sulfate, chloride and nitrate anions, are incorporated during electrochemical precipitation of α-$Ni(OH)_2$ and are eliminated from the structure during the aging from the α to the β form.

The Ni 2p region for the α samples shows Ni(II) peaks similar to those observed in the β-$Ni(OH)_2$ spectra. However, subtle differences in the peak shapes and relative intensities between the α and β phases result in greater deviations between fitted line-shapes and the measured data (Figure 2.3b). At present, there are no reported XPS peak-fitting parameters for α-$Ni(OH)_2$.

These measurements demonstrate that XPS cannot easily differentiate the two phases. However, XPS can differentiate $Ni(OH)_2$ from metallic Ni and other nickel oxides, such as the air-formed nickel oxide on the Ni substrate (Figure 2.3c). It is also an effective way to identify and quantify elemental impurities on the surface.

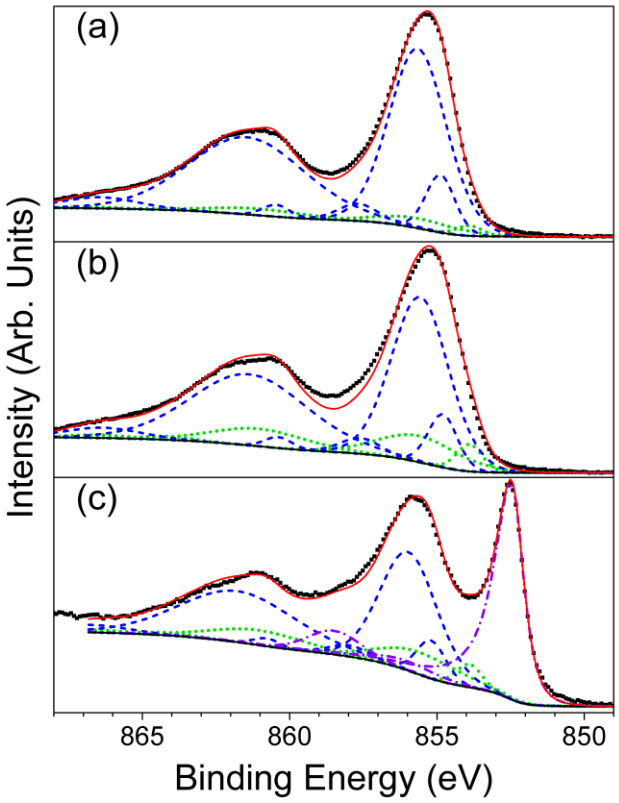

Figure 2.3 X-ray photoelectron spectra (■) for samples (a) β_3, (b) α_3 and (c) Ni metal substrate curve-fitted with β-$Ni(OH)_2$ (- - -), NiO (• • •) and Ni (– • –) components using the line shapes and method of Biesinger *et al* [159]. No literature references are presently available for the line shape of α-$Ni(OH)_2$. The solid red line shows the calculated line shape and the solid black line shows the Shirley background.

2.3.3. Raman Spectra

As measured, several of the Raman spectra show a strong background (Figure 2.4i) that can be removed computationally (Figure 2.4ii). All samples show a sharp feature at 2330 cm^{-1}, which is an artifact of the laser excitation source. All samples also show a weak feature at ~1556 cm^{-1}, which corresponds to a two-magnon transition that arises from the room temperature antiferromagnetism of NiO [160]. The presence of this peak demonstrates that the air-formed oxide (NiO_x, $x \approx 1$) on the metal substrate, only 9 – 12 Å thick [44, 45], underlies all the deposited $Ni(OH)_2$ films. The Raman spectra of samples β_1, β_2 and β_3 are very similar, whereas the spectra of sample α_3 contain several peaks that are not observed for sample α_2.

The Raman spectra for sample α_1 (Figure 2.4d) have very low signal-to-noise and only contain a broad, weak band centered at ~3575 cm^{-1} (α-$Ni(OH)_2$, O-H stretch) and medium peaks from sulfate ions (see section 2.3.8). Because the weak lattice modes could not be observed, this sample is not discussed in more detail.

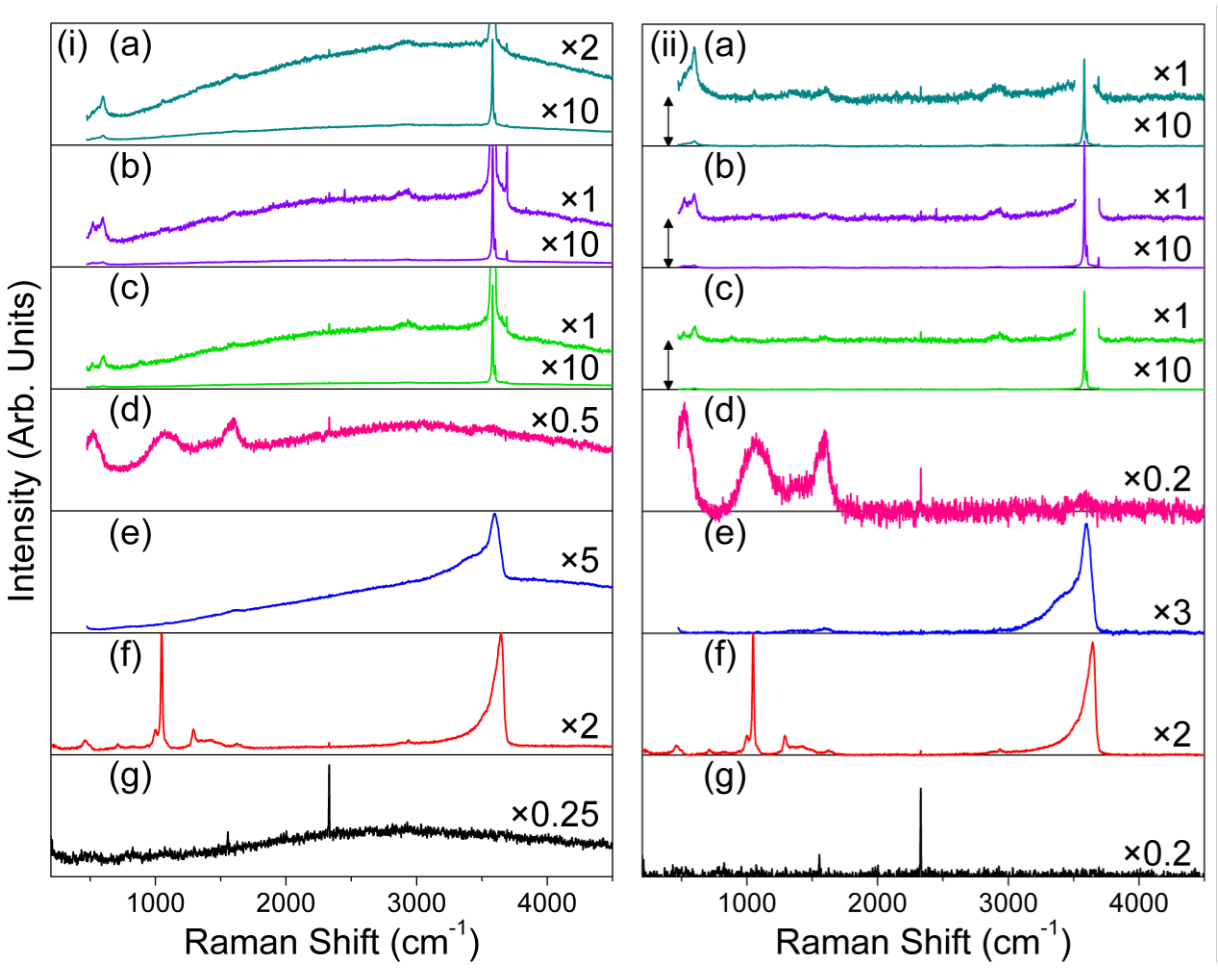

Figure 2.4 Raman spectra of samples (a) β_1, (b) β_2, (c) β_3, (d) α_1, (e) α_2, (f) α_3, and (g) the untreated Ni substrate. The data are shown on the same intensity scale (i) as collected and (ii) after background subtraction. The y-axis is linear and select traces are rescaled by a factor, indicated on the plots. Traces (ii) (a), (b), and (c) are offset as shown by double-headed arrows.

2.3.4. Infrared Spectra

All IR spectra contain sharp, weak features corresponding to the asymmetric bending, at 668 cm^{-1}, and asymmetric stretching, at 2341 cm^{-1} and 2361 cm^{-1}, modes of CO_2 gas and some sharp, weak interference that arises from bending, at ~1600 cm^{-1}, and asymmetric stretching, at ~3750 cm^{-1}, modes of H_2O vapour in the sample chamber (Figure 2.5). All spectra also contain a sharp, weak feature at 2170-2180 cm^{-1} due to an adsorbed species, likely CO_2. The absolute absorbance of each sample cannot be determined because the exact film thicknesses are unknown, which affects the relative peak intensities. The reflectance of the substrates varies slightly. This causes the spectra to be offset by unknown, however, constant values, assuming that the reflectance is independent of the wavelength. A large, periodic background arising from the Fourier transform procedure was computationally removed from the IR spectra of sample β_1. Therefore, peak shapes and absolute reflectance values are subject to some error. All other IR spectra are presented as measured. The results of the IR measurements complement the Raman spectra well, showing that samples β_1, β_2 and β_3 are very similar, whereas sample α_3 shows several peaks that are not observed in samples α_1 or α_2, which correspond to nitrate bands. Sample α_1 has very high reflectance and a low signal-to-noise ratio, which indicates that it is very disordered and scatters the incident IR beam. Several peaks that are not present in samples α_2 and α_3 are observed that originate from sulfate anions.

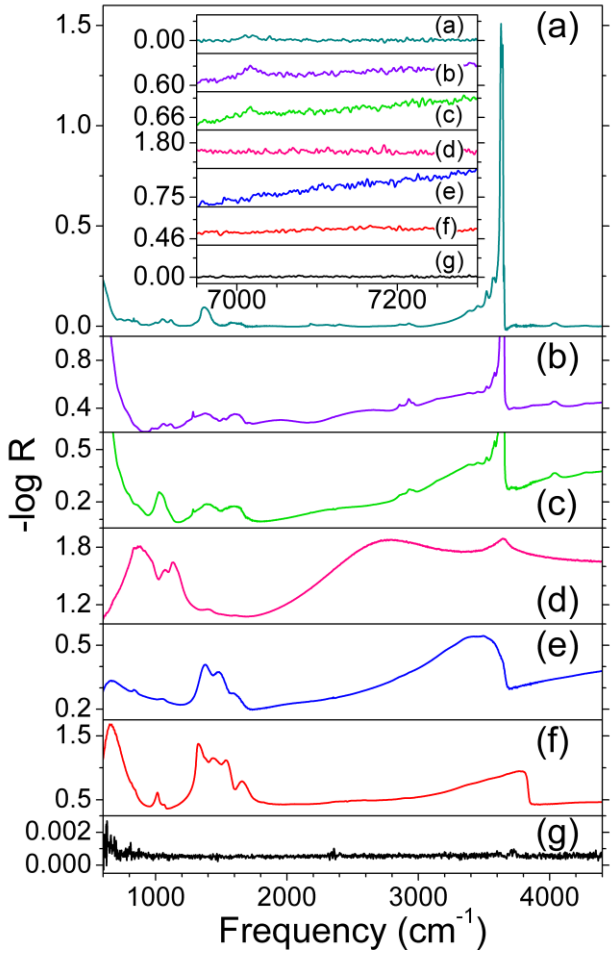

Figure 2.5 Infrared reflectance spectra of samples (a) β_1, (b) β_2, (c) β_3, (d) α_1, (e) α_2, (f) α_3, and (g) Ni substrate. The broad feature in (d) at ~2600 cm^{-1} is an artifact of the Fourier transform from low sample reflectance. Inset shows high frequency combination bands. Inset spectra are all plotted on the same -log R scale with each box 0.06 units in height and tick marks spaced 0.03 units apart.

The IR spectra for β-$Ni(OH)_2$ are more complex than the Raman spectra because of transverse optical (TO)/longitudinal optical (LO) splitting of the vibrational modes. For asymmetric vibrational modes involving ionic species, TO modes do not create long-range Coulomb effects, whereas LO modes do. Additional restoring forces act upon the oscillating nuclei and cause LO transitions to occur at higher energies than their corresponding TO transitions. Further, LO and TO transitions of different modes with the same symmetry may not cross over in energy [161]. The TO/LO splitting also causes peak intensities to depend on the crystal orientation relative to the polarization of the IR beam. However, this study examines polycrystalline samples using non-polarized light so this effect is not observed. The LO/TO effect is not observed for symmetric, *e.g.* Raman-active, modes.

2.3.5. Vibrational Modes of β-$Ni(OH)_2$

2.3.5.1. Raman-Active Vibrational Modes of β-$Ni(OH)_2$

From the symmetry of β-$Ni(OH)_2$, the factor group theory predicts four Raman-active transitions, two with E_g symmetry and two with A_{1g} [161]. It is well-established that three of these modes are at 310-315 cm^{-1}, 445-453 cm^{-1} and 3581 cm^{-1}. The symmetry of these transitions has been disputed because the position of the fourth mode has not been clearly determined [77]. However, it is worth noting that the Raman-active lattice modes of brucite, $Mg(OH)_2$, which is isostructural, are at similar positions: 280 cm^{-1}, 443 cm^{-1}, 725 cm^{-1} and 3652 cm^{-1} [162]. A detailed computational analysis of brucite shows the atomic displacements corresponding to each mode [161]. Thus, the peak measured at ~880 cm^{-1} (Figure 2.6a) is here ascribed to the final lattice mode of β-$Ni(OH)_2$ and the symmetries of the transitions can be assigned (Tables 2.2–2.5).

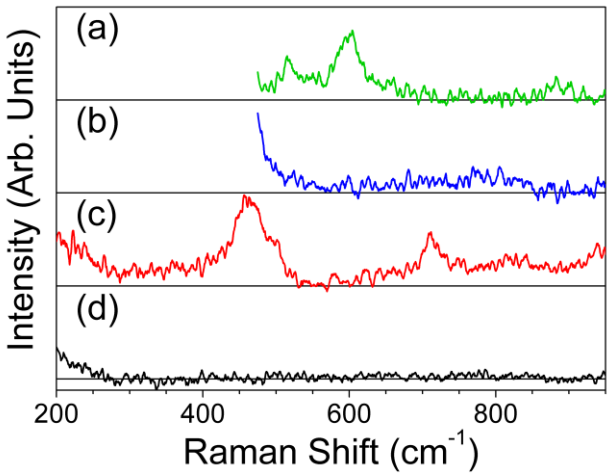

Figure 2.6 Raman spectra of samples (a) β_3, (b) α_2 and (c) α_3 showing lattice modes. (d) The Raman spectrum of water is shown for comparison. All spectra are plotted on the same intensity scale.

Table 2.2 Raman peaks for β-$Ni(OH)_2$ prepared from $Ni(NO_3)_2$ then aged in KOH [β_3][a].

Peak Frequency cm^{-1}	**Width**	**Peak Intensity**	**Peak Assignment**	
516	Medium	Weak	β-$Ni(OH)_2$	2nd order acoustic mode
601	Medium	Medium	β-$Ni(OH)_2$	2 E_g
~880[b]	Broad	Very weak	β-$Ni(OH)_2$	E_g O-H bend
1055[c]	Medium	Weak	SO_4^{2-}	ν_1
1556	Very Sharp	Extremely weak	Air-formed NiO_x	2 magnon
~1600	Broad	Very weak	Trapped H_2O	O-H bend
~1635	Broad	Weak	Free H_2O	O-H bend
~2900	Broad	Very weak	Surface hydrocarbon	C-H stretch
3581	Sharp	Very strong	β-$Ni(OH)_2$	A_{1g} O-H stretch
3601	Sharp	Strong	Disordered β-$Ni(OH)_2$	O-H stretch
3655[d]	Sharp	Very weak	Disordered β-$Ni(OH)_2$	O-H stretch
3688	Sharp	Weak	Disordered β-$Ni(OH)_2$	O-H stretch, surface

[a]Samples aged in KOH after preparation from $NiSO_4$ [β_1] and $NiCl_2$ [β_2] gave the same results except as noted.

[b]Not observed in samples prepared from $NiSO_4$ [β_1]

[c]Only observed in samples prepared from $NiSO_4$ [β_1]

[d]Only observed in samples prepared from $Ni(NO_3)_2$ [β_3]

Table 2.3 Infrared peaks for β-$Ni(OH)_2$ prepared from $NiSO_4$ then aged in KOH [β_1].

Peak Frequency cm^{-1}	**Width**	**Peak Intensity**	**Peak Assignment**	
< 600[a]	Medium	Strong	β-$Ni(OH)_2$	A_{1g} + acoustic mode combination
~635 sh	Medium	Weak	β-$Ni(OH)_2$	E_g + A_{2u} (TO)/E_g + E_u (TO) combination
~1045	Medium	Medium	β-$Ni(OH)_2$	E_u (LO) O-H bend
1285	Sharp	Weak	Surface hydrocarbon	C-H bend
1385	Medium	Medium	β-$Ni(OH)_2$	E_g + A_{2u} (TO) combination
~1560	Medium	Weak	β-$Ni(OH)_2$	E_u (LO) + 2^{nd} order acoustic mode
~1640	Medium	Weak	Free H_2O	O-H bend
2655	Sharp	Very weak	β-Ni(OH)(OD)	A_{2u} (TO/LO) O-D stretch
2855	Medium	Weak	Surface hydrocarbon	C-H stretch
2880 sh	Medium	Weak	Surface hydrocarbon	C-H stretch
2928	Medium	Weak	Surface hydrocarbon	C-H stretch
2960 sh	Medium	Weak	Surface hydrocarbon	C-H stretch
3380	Medium	Weak	Free H_2O	O-H stretch
3450	Medium	Weak	Free H_2O	O-H stretch
3520	Sharp	Weak	β-$Ni(OH)_2$	A_{1g} – acoustic mode subtraction
3566	Sharp	Weak	β-$Ni(OH)_2$	A_{1g} – acoustic mode subtraction
3580	Sharp	Medium	β-$Ni(OH)_2$	A_{1g} O-H stretch
3601 sh	Sharp	Medium	Disordered β-$Ni(OH)_2$	O-H stretch (in-phase)
3629	Sharp	Very strong	β-$Ni(OH)_2$	A_{2u} (TO) O-H stretch
3634 sh	Sharp	Strong	Disordered β-$Ni(OH)_2$	O-H stretch (TO, out-of-phase)
3643	Sharp	Very strong	β-$Ni(OH)_2$	A_{2u} (LO) O-H stretch
3652	Sharp	Strong	Disordered β-$Ni(OH)_2$	O-H stretch (LO, out-of-phase)
4040	Medium	Medium	β-$Ni(OH)_2$	A_{1g} + A_{2u} (LO)/A_{1g} + E_u (LO) combination
4270	Broad	Very weak	β-$Ni(OH)_2$	3^{rd} order combination
7020	Sharp	Very weak	β-$Ni(OH)_2$	A_{1g} + A_{2u} (TO/LO) combination

[a]Peak maximum is below the instrumental cut-off so the exact position is unknown.

Table 2.4 Infrared peaks for β-$Ni(OH)_2$ prepared from $Ni(NO_3)_2$ then aged in KOH [β_3][a].

Peak Frequency cm^{-1}	**Width**	**Peak Intensity**	**Peak Assignment**	
< 600[b]	Medium	Strong	β-$Ni(OH)_2$	A_{1g} + acoustic mode combination
665 sh	Medium	Weak	β-$Ni(OH)_2$	E_g + A_{2u} (TO)/E_g + E_u (TO) combination
1030	Medium	Medium	β-$Ni(OH)_2$	E_u (LO) O-H bend
1285	Sharp	Weak	Surface hydrocarbon	C-H bend
~1400	Broad	Medium	β-$Ni(OH)_2$	E_g + A_{2u} (TO) combination
~1550	Medium	Medium	β-$Ni(OH)_2$	E_u (LO) + 2^{nd} order acoustic mode
~1630	Broad	Medium	Free H_2O	O-H bend
2658	Sharp	Very weak	β-Ni(OH)(OD)	A_{2u} (TO/LO) O-D stretch
2855 sh	Medium	Weak	Surface hydrocarbon	C-H stretch
2880	Medium	Weak	Surface hydrocarbon	C-H stretch
2930	Medium	Weak	Surface hydrocarbon	C-H stretch
2960 sh	Medium	Weak	Surface hydrocarbon	C-H stretch
3140	Medium	Very weak	β-$Ni(OH)_2$	O-H bend combination
3380	Medium	Weak	Free H_2O	O-H stretch
3450	Medium	Weak	Free H_2O	O-H stretch
3520	Sharp	Weak	β-$Ni(OH)_2$	A_{1g} – acoustic mode subtraction
3566	Sharp	Very weak	β-$Ni(OH)_2$	A_{1g} – acoustic mode subtraction
3581	Sharp	Weak	β-$Ni(OH)_2$	A_{1g} O-H stretch
3601 sh	Sharp	Very weak	Disordered β-$Ni(OH)_2$	O-H stretch (in-phase)
~3635	Sharp	Extremely strong	β-$Ni(OH)_2$	A_{2u} (TO/LO) O-H stretch
3652	Sharp	Strong	Disordered β-$Ni(OH)_2$	O-H stretch (LO, out-of-phase)
4035	Medium	Weak	β-$Ni(OH)_2$	A_{1g} + A_{2u} (LO)/A_{1g} + E_u (LO) combination
~4275	Broad	Very weak	β-$Ni(OH)_2$	3^{rd} order combination
7020	Sharp	Very weak	β-$Ni(OH)_2$	A_{1g} + A_{2u} (TO/LO) combination

[a]The sample prepared from $NiCl_2$ then aged in KOH [β_2] gave the same results.

[b]Peak maximum is below the instrumental cut-off so the exact position is unknown.

Table 2.5 Comparison of literature values for the vibrational modes in β-$Ni(OH)_2$ and equivalent modes in $Mg(OH)_2$ (brucite).

Our Peak Assignment	**Mode Frequency (cm^{-1})**		
	This Study	Literature	$Mg(OH)_2$
Raman			
E_g lattice mode	---	315 [29], 319 [59], 310 [66], 310 [67], 312-313 [69], 318 [72], 306 [73], 315 [75], 309 [76], 313 [77]	280 [162]
A_{1g} lattice mode	---	450 [29], 450 [46], 458 [59], 450 [66], 445 [67], 448-453 [69], 449 [72], 445 [73], 450 [75], 446 [76], 447 [77]	443 [162]
2^{nd} order acoustic mode	516	510 [46], 519 [59], 515 [66], 510 [67], 519 [69], 510 [73], 517 [75], 510 [76], 508 [77]	---
2 E_g 2^{nd} order lattice mode	601	---	---
E_g O-H bend	~880	~850 [72], 880 [75]	725 [162]
Trapped H_2O, O-H bend	~1600	---	---
Free H_2O, O-H bend	~1635	---	---
A_{1g} O-H stretch	3581	3581 [29], 3599 [59], 3580 [65], 3585 [66], 3570 [67], 3565 [68], 3580-3583 [69], 3580 [72], 3579 [73], 3580 [75], 3579 [76], 3581 [77]	3652 [162]
Disordered, O-H stretch	3601	3601 [29], 3605 [66], 3580 [67], 3600 [68], 3600 [69], 3600 [75], 3599 [76], 3601 [77]	---
Surface, O-H stretch	3688	3680 [67], 3687 [68], 3687 [69]	---
Infrared			
A_{2u} (TO)/E_u (TO) lattice modes	---	350 [30], 350 [31], 348 [57], 345 [58], 340 [59], 350 [61], 354 [62], 350 [72], 332 [77]	368 [163]
A_{2u} (LO)/E_u (LO) lattice modes	---	~450 [25], 450 [30], 450 [31], 451 [57], 460 [58], 458 [59], 460 [61], 475 [62], 460 [66], 452 [72] 440 [77]	562 [163]
E_u (TO) O-H bend	---	517 [25], 530 [30], 545 [31], 549 [57], 520 [58], 525 [59], 510 [61], 530 [62], 525 [66], 553 [72], 530 [77]	462 [163]
E_u (LO) O-H bend	1030	1030 sh [66]	---
Free H_2O, O-H bend	~1630	1620 [30], 1630 [66]	
A_{2u} (TO) O-H stretch	3629	3640 [25], 3650 [30], 3650 [31], 3650 [38], 3635 [57], 3650 [58], 3650 [61], 3650 [62], 3639 [65], 3630 [72], 3636 [77], 3640 [78]	3698 [163]
Disordered, (TO) O-H stretch	3634	---	---
A_{2u} (LO) O-H stretch	3643	---	---
Disordered, (LO) O-H stretch	3652	---	---
A_{1g} + A_{2u} (LO)/A_{1g} + E_u (LO)	4035	4028 [65]	---
3^{rd} order combination	~4275	4274[65]	---
A_{1g} + A_{2u} (TO/LO)	7020	7016[65]	---

An additional band at 508-519 cm^{-1} is sometimes reported and is visible in Figure 2.6a. The intensity of this feature varies between samples and is generally more intense for less crystalline samples [77]. Although it has sometimes been ascribed to a lattice mode, the frequency is much lower than expected for the E_g mode [161] and its intensity can vary independently of the other lattice modes [67]. Inelastic neutron scattering measurements show that there is an acoustic vibrational mode at ~250-270 cm^{-1}, the harmonic overtone of which should be observable by Raman spectroscopy [77]. Second order modes are typically very weak and increase in intensity for disordered samples, hence, the peak is assigned to this transition, consistent with the reported intensity-crystallinity correlation.

A Raman band is observed at 601 cm^{-1} (Figure 2.6a) that has not been previously reported, presumably due to instrumental limitations. Since this peak is very weak and is not a predicted lattice mode, this peak is taken to be the harmonic overtone of the E_g transition at 306-318 cm^{-1}.

A very weak feature at ~1600 cm^{-1} is superimposed with a weak peak at ~1630 cm^{-1} (c). The latter is ascribed to the O-H bend of H_2O that has adsorbed on the material surface or has been trapped within the material, whereas the former is similar in shape to free water, however, in the wrong position. Thus, this is taken to be the O-H bend for a small degree of hydration in the structure (formally termed a libration mode for lattice species [161]).

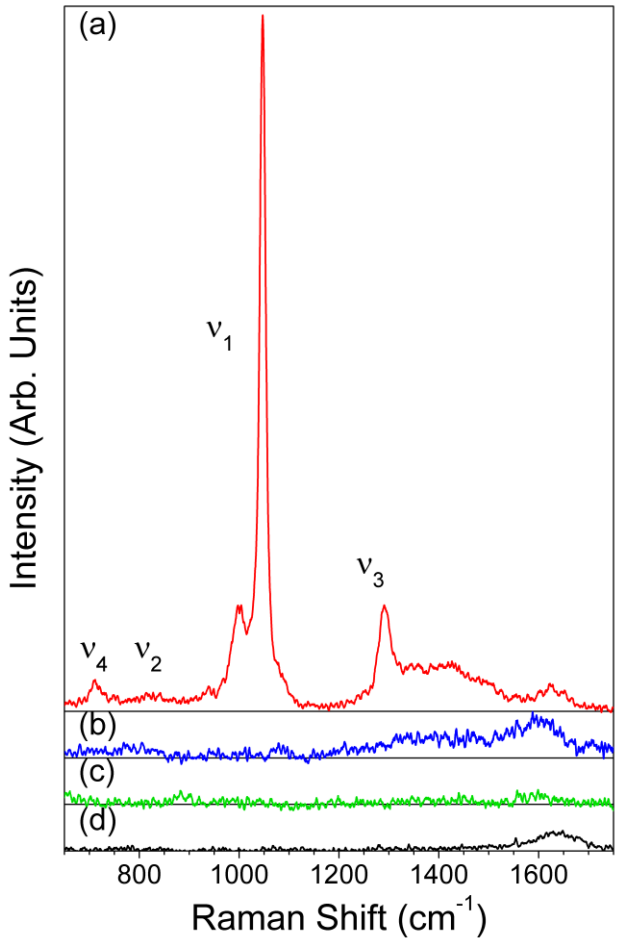

Figure 2.7 Raman spectra of samples (a) α_3, (b) α_2 and (c) β_3 showing the intermediate frequency range modes. The nitrate ion vibrational modes, labeled ν_1-ν_4 are shown for sample α_2. These features are absent in samples α_1 and β_2. (d) The Raman spectrum of water is shown for comparison. All spectra are plotted on the same intensity scale.

A sharp band at 3601 cm^{-1} is present in the Raman spectra for samples β_1, β_2, and β_3 (Figure 2.4 and Figure 2.8). This peak has previously been variously assigned to adsorbed H_2O, crystal defects, impurities, surface OH groups and the O-H stretch for a new crystal phase, β_{bc}-$Ni(OH)_2$ [66, 68, 77]. The intensity of this peak has been reported to increase with decreasing crystallite size, as measured by XRD peak width [66]. However, only the diffraction peaks involving the crystallographic c-axis were broadened. This indicates stacking faults rather than small crystallites, and thus the Scherrer equation cannot be properly applied. Re-examination of the results reveals that the Raman peak intensity at 3601 cm^{-1} increases as disorder along the c-axis increases. The peak intensity decreases when samples are heated to 100-150 °C [66].

I now propose that the β_{bc} phase is more accurately described as β-$Ni(OH)_2$ that has stacking fault disorder. In the O-H stretching modes, the H atoms approach adjacent sheets more closely than in other vibrational modes, and hence, the Raman peak at 3581 cm^{-1} is shifted to 3601 cm^{-1}. There must be a finite number of relative sheet positions and orientations that occupy local free energy minima. If the sheets do not rotate then two structures are predicted, namely a) Ni atoms in register between adjacent sheets, which is the thermodynamic minimum, and b) a staggered configuration in which Ni atoms are in register between alternating sheets (if the sheets do rotate, then the rotation would be by 60°, and hence, two more new structures are permitted). Though the true geometry is unknown, this kinetically stable structure has slightly different O-H stretching modes and restructures to the stable form when heated to 100-150 °C. This disordered structure has never been reported in excess of the ordered β-$Ni(OH)_2$ component and, thus, it can only co-exist as part of a parent β phase material. Therefore, the evidence does not support the existence of an additional crystallographic phase, but rather a disordered form of β-$Ni(OH)_2$.

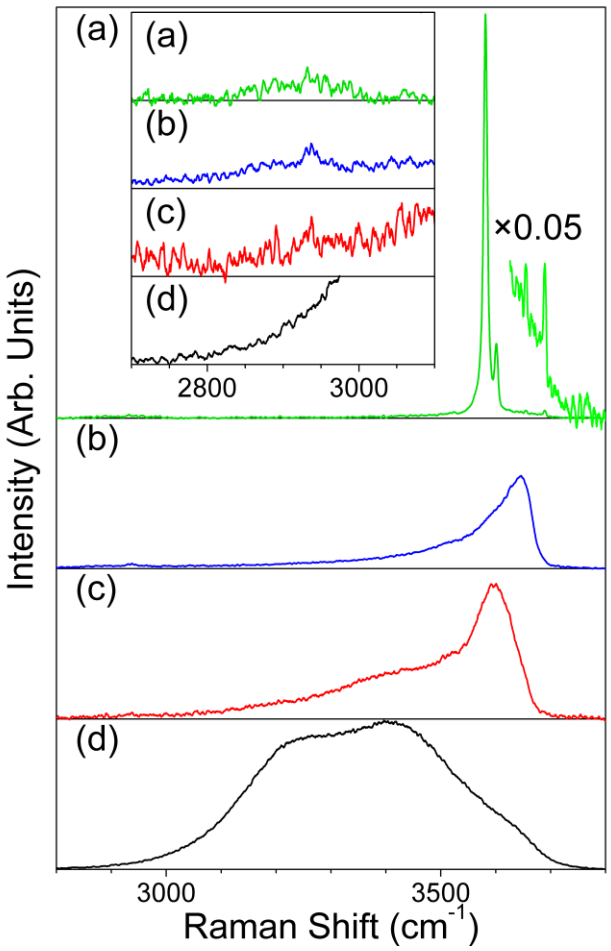

Figure 2.8 Raman spectra of samples (a) β_3, (b) α_2 and (c) α_3 showing O-H internal modes. (d) The Raman spectrum of water is shown for comparison. All spectra, except where noted, are plotted on the same intensity scale. Inset shows low frequency region of the figure enlarged by a factor of 15.

The number of exchanged electrons per Ni atom in β-$Ni(OH)_2$ electrodes has been found to approach unity for materials with a strong Raman band at 3605 cm^{-1} (corresponding to my peak at 3601 cm^{-1}), whereas it is close to 0.8 for samples that do not show this peak. This was previously attributed to the increased surface area of smaller crystallites [66]. However, my re-interpretation of this peak leads to the conclusion that materials with c-axis disorder are better candidates than more ordered structures. The photocatalysts prepared by Yu *et al.* also have c-axis disorder that can be observed from their XRD patterns [39], which may indicate that photocatalytic activity is also linked to stacking faults in the crystal structure.

A weak but sharp peak is observed at 3655 cm^{-1} that I assign to the IR-active disordered O-H stretch. Because this is an out-of-phase mode, it is quite weak in the Raman spectrum. However, the disorder or the change in symmetry makes it only weakly visible. It is also possible that this is a localized mode around Ca point defects from the $Ni(NO_3)_2$ starting material (*cf.* A_{1g} for bulk $Ca(OH)_2$ is observed at 3620 cm^{-1} [162]). Ca was not detected in the more-ordered samples β_1 and β_2 and the peak is not present in their Raman spectra, which makes either explanation equally plausible.

One additional Raman peak is observed at 3688 cm^{-1}. The intensity is sometimes reported to be linked to that of the peak at 3601 cm^{-1}. However, the peaks have also been observed to vary independently of each other [66, 67]. Bernard *et al.* observed that dry samples, which initially show this peak, that are rinsed with water and re-analyzed while still wet, lose the peak completely [67]. This indicates that it is a surface-related phenomenon, although the exact origin is unclear. Bernard *et al.* proposed that the O-H stretch for surface hydroxide groups is at higher energy than for those opposed by adjacent layers. Upon hydration the transition becomes similar to either the bulk O-H stretching mode, A_{1g}, or that of free H_2O [67].

The peak observations and assignments are summarized in Table 2.

2.3.5.2. Infrared-Active Vibrational Modes of β-Ni(OH)$_2$

Factor group theory predicts four IR-active vibrational modes for β-Ni(OH)$_2$: Two A_{2u} and two E_u [161]. There are twice as many IR peaks as there are Raman peaks for β-Ni(OH)$_2$ because of transverse optical (TO)/longitudinal optical (LO) splitting (see section 2.3.4). The magnitude of this splitting effect has been calculated for brucite and can be used to assist peak identification for β-Ni(OH)$_2$ [161].

Only four IR lattice modes have been previously identified: 332-354 cm^{-1}, 440-475 cm^{-1}, 510-553 cm^{-1} and 3630-3650 cm^{-1} [77]. The LO/TO splitting for the A_{2u} mode at ~3635 cm^{-1} is expected to be quite small (*cf.* 14 cm^{-1} for Mg(OH)$_2$ [161]). The observed peaks for samples β_2 and β_3 exhibit flat tops because of the low reflectance at this higher sample thickness. The peak for the thinner sample β_1 is better defined and shows peaks at 3629 cm^{-1} and 3643 cm^{-1}, which are assigned to the A_{2u} (TO) and A_{2u} (LO) modes, respectively. An IR study of β-Ni(OD)$_2$ showed that the two apparent peaks at 350 cm^{-1} and 450 cm^{-1} are actually each composed of two overlapping peaks: One each that red-shifts on deuteration and one each that does not observably shift. The peak at 550 cm^{-1} is also observed to red-shift on deuteration [31]. The two remaining A_{2u} modes are not predicted to significantly shift on deuteration, whereas all four of the E_u modes are [161]; hence, these peaks can be assigned accordingly. This is consistent with a study that observed the shift in position of three lattice modes for $Mg_{1-x}Ni_x(OH)_2$, where $0 \leq x \leq 1$ [57]. The remaining E_u mode is predicted at a frequency greater than 550 cm^{-1} and has a very large TO/LO split (*cf.* 370 cm^{-1} for brucite), thus, this mode is assigned to the broad band at ~1030 cm^{-1} (Figure 2.9). Because of its low intensity this peak is previously unreported, although close

examination reveals that it may be visible as a weak shoulder in published results [66]. Thus, the eight IR-active lattice modes have now been identified and assigned (Table 5).

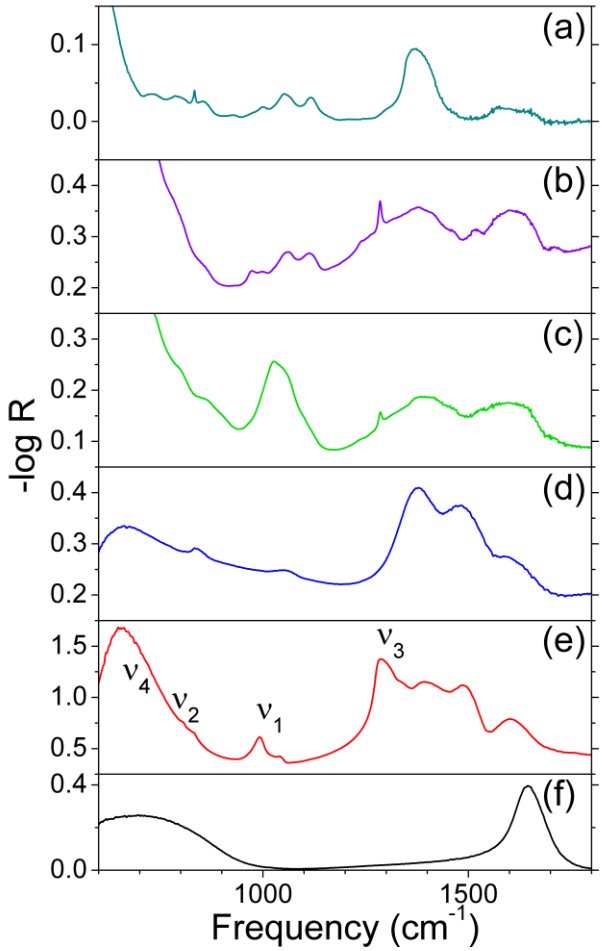

Figure 2.9 Infrared reflectance spectra of samples (a) β_1, (b) β_2, (c) β_3, (d) α_2, (e) α_3, and (f) a thin film of water on a Ni substrate.

A broad peak at ~1630 cm^{-1} (Figure 2.9) arises from the O-H bending mode of H_2O that is either adsorbed on the material surface or trapped within the structure. The peaks at ~3380 cm^{-1} and ~3450 cm^{-1} are from the O-H stretch of the H_2O (Figure 2.10).

A sharp but weak peak measured at 3581 cm^{-1} corresponds exactly to the Raman-active A_{1g} transition (Figure 2.10). This is formally forbidden in IR spectroscopy, however, structural disorder allows a very weak peak to be seen in the IR spectra. Conversely, a weak A_{2u} mode should also be allowed in the Raman spectrum. However, this mode overlaps with other features of the sample and, hence, cannot be observed in the Raman spectrum. A shoulder at 3601 cm^{-1} corresponds to the in-phase O-H stretch of disordered β-$Ni(OH)_2$ discussed in the Raman section. The corresponding out-of-phase O-H stretch (LO) is a strong, sharp peak at 3652 cm^{-1}. The corresponding TO mode is visible in the spectra for sample β_1 as a shoulder at 3634 cm^{-1}. Note that disorder shifts both the TO and LO modes to higher frequency by 5-9 cm^{-1}, which reaffirms that these two peaks are connected.

The peak at 2658 cm^{-1} is sharp, very weak and close to the positions reported for the A_{2u} mode of β-$Ni(OD)_2$ (*cf.* 2705 cm^{-1} [31], 2680 cm^{-1} [62], 2690 cm^{-1} [78]). The difference in position could arise because this study observes localized modes from the naturally present D (0.0115 %), whereas the reference materials were highly enriched.

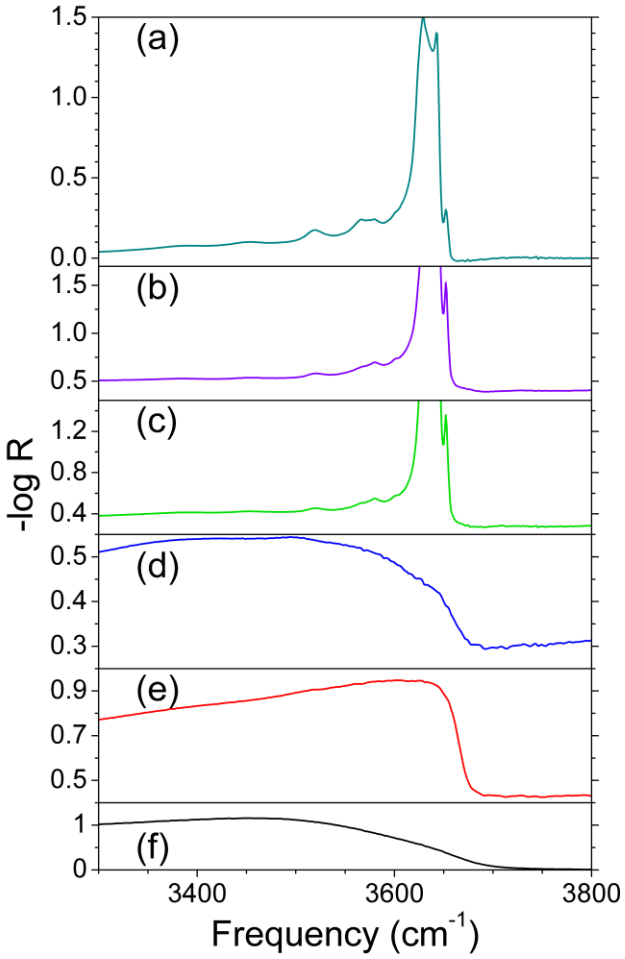

Figure 2.10 Infrared reflectance spectra of samples (a) β_1, (b) β_2, (c) β_3, (d) α_2, (e) α_3, and (f) a thin film of water on a Ni substrate.

Several previously unreported weak features are observed in the IR spectra for β-$Ni(OH)_2$ that can be ascribed to combination bands. Since this structure has an inversion centre, the overall symmetry must be odd (ungerade) for a transition to be IR-active. Thus, all overtone transitions are even and therefore Raman-active, whereas an IR mode or an acoustic mode combined with a Raman mode is odd and therefore IR-active. The peak assignments (Tables 2.3 and 2.4) were created by considering the IR and Raman lattice modes (Table 2.5) and the acoustic transitions observed by INS [77]. To conclusively assign these peaks, single crystal measurements using plane-polarized light are necessary, especially the modes for which multiple combinations are possible. One particularly interesting combination is the sharp peak at 3520 cm^{-1} assigned to the combination of the A_{1g} mode and a subtractive mode, *i.e.* a hot band, for the acoustic transition at ~60 cm^{-1} (Figure 2.10) [77]. Hot bands are not typically observed in IR spectra at room temperature. However, the acoustic transition is sufficiently low in energy that a Boltzmann distribution predicts a population ratio of 57 to 43 for the ground state and first excited state, respectively. Another combination of the A_{1g} and a subtractive mode is observed at 3566 cm^{-1}.

2.3.6. Vibrational Modes of α-$Ni(OH)_2$

2.3.6.1. Raman-Active Vibrational Modes of α-$Ni(OH)_2$

The Raman spectra of α-$Ni(OH)_2$ show lattice modes at 460 cm^{-1} and 495 cm^{-1} (Figure 2.6). Presumably due to instrumental limitations, only the former peak has been previously reported [69, 71, 73]. Weak features, assigned in this work to second order transitions, are observed at ~790 cm^{-1} and ~1075 cm^{-1}. Some authors report additional Raman-active lattice

modes [69, 76]. However, these are not observed in the present work and can all be ascribed to β-$Ni(OH)_2$ impurities.

Structural disorder causes the internal O-H bending mode of lattice OH to split and broaden into a weak feature at ~1400 cm^{-1} (Figure 2.7). Since the Raman intensity is quite weak it is necessary to use IR, discussed below, to observe fine details for these peaks. Further, this broad feature underlies several nitrate bands in sample α_3, and is therefore unclear. A second internal O-H bending mode at 1590-1620 cm^{-1} is similar in width and only slightly shifted from the position of free H_2O. Thus, this can be assigned to the O-H bending mode of intercalated H_2O. A third internal O-H bending mode is observed at 1630 cm^{-1}, which arises from adsorbed H_2O on the surface or H_2O trapped within the structure.

There are several O-H stretching modes from 3240 cm^{-1} to 3515 cm^{-1} that arise from free H_2O (Figure 2.8). The internal O-H stretching modes from lattice OH and intersheet H_2O are visible from 3590 to 3650 cm^{-1}. This region is quite different between samples α_2 and α_3 and such differences have previously been suggested to arise from the presence of intermediate phases [73]. However, since the lattice modes do not vary as significantly between samples, this supports that this phase tends to adopt disorder by the incorporation of foreign ions, variable hydration, and randomly oriented layers [35]. This is confirmed by my measurement of two preparations of sample α_2 where no variation in lattice mode frequencies was found but the frequencies of the internal modes of the nitrate ions (see section 2.3.7) and the O-H stretching frequency are different. The shifts in frequency are caused by variations in the local environment and/or stress (see section 2.2.4).

These peak observations and assignments are summarized in Tables 2.6 and 2.7.

Table 2.6 Raman peaks for α-$Ni(OH)_2$ prepared from $NiCl_2$ [α_2].

Peak Frequency cm^{-1}	**Width**	**Peak Intensity**	**Peak Assignment**	
~790	Medium	Weak	α-$Ni(OH)_2$	2nd order lattice mode
~1075	Medium	Very weak	α-$Ni(OH)_2$	2nd order lattice mode
~1400	Broad	Weak	α-$Ni(OH)_2$	O-H bend, lattice OH
1555	Very sharp	Extremely weak	NiO	2 magnon
~1590	Broad	Weak	α-$Ni(OH)_2$	O-H bend, layer H_2O
1630 sh	Medium	Very weak	Free H_2O	O-H bend
~2900	Broad	Very weak	α-$Ni(OH)_2$/surface hydrocarbon	2nd order O-H bend/C-H stretch
2935	Sharp	Very weak	Surface hydrocarbon	C-H stretch
~3240	Very broad	Weak	Free H_2O	O-H stretch
~3380	Very broad	Medium	Free H_2O	O-H stretch
~3515	Broad	Medium	Free H_2O	O-H stretch
3590	Medium	Strong	α-$Ni(OH)_2$	O-H stretch
3620	Medium	Strong	α-$Ni(OH)_2$	O-H stretch
3650 sh	Medium	Medium	α-$Ni(OH)_2$	O-H stretch

Table 2.7 Raman peaks for α-$Ni(OH)_2$ prepared from $Ni(NO_3)_2$ [α_3].

Peak Frequency cm^{-1}	**Width**	**Peak Intensity**	**Peak Assignment**	
460	Medium	Weak	α-$Ni(OH)_2$	Lattice mode
495 sh	Medium	Weak	α-$Ni(OH)_2$	Lattice mode
712/719[a]	Medium	Weak	NO_3^-	ν_4
816/840[a]	Medium	Weak	NO_3^-	ν_2
~935	Medium	Very weak	α-$Ni(OH)_2$	2nd order lattice mode
997/1002[a]	Sharp	Medium	NO_3^-	ν_1
1047/1048[a]	Sharp	Strong	Free NO_3^-	ν_1
1075 sh	Medium	Weak	α-$Ni(OH)_2$	2nd order lattice mode
1291/1293[a]	Medium	Medium	NO_3^-	ν_3
~1350	Medium	Very weak	Free NO_3^-	ν_3
~1420	Broad	Weak	NO_3^-	$2\nu_4$
~1495	Broad	Weak	NO_3^-	$\nu_2 + \nu_4$
1554	Very Sharp	Extremely weak	Air-formed NiO_x	2 magnon
~1620	Medium	Weak	α-$Ni(OH)_2$	O-H bend, layer H_2O
~1630	Broad	Weak	Free H_2O	O-H bend
~1695	Medium	Very weak	NO_3^-	$2\nu_2$
~2900	Broad	Very weak	α-$Ni(OH)_2$/Surface hydrocarbon	2nd order O-H bend/C-H stretch
~2935	Medium	Very weak	Surface hydrocarbon	C-H stretch
~3240	Broad	Very weak	Free H_2O	O-H stretch
3515 sh	Broad	Medium	Free H_2O	O-H stretch
3647/3642[a]	Medium	Strong	α-$Ni(OH)_2$	O-H stretch

2.3.6.2. Infrared-Active Vibrational Modes of α-Ni(OH)$_2$

There are three IR-active α-Ni(OH)$_2$ modes at 380-400 cm^{-1}, 460-480 cm^{-1} and 625-670 cm^{-1} (Figure 2.9). Only the last of these is observed in this work due to instrumental limitations. Weakly visible combination bands are observed at 835 cm^{-1} and 1055 cm^{-1}. The latter is not visible in the spectra of sample α_2 because it is obscured by nitrate bands.

Two peaks from the O-H bending modes of lattice OH are observed at 1380-1390 cm^{-1} and 1480-1490 cm^{-1} (Figure 2.9). These peaks shift slightly between samples because of structural disorder and the mechanical stress induced when the materials dried. The O-H bending mode from intercalated H_2O is measured at 1600 cm^{-1}, which matches the Raman spectra. Note that the absorbance of the first three O-H bending modes is too great to be assigned to free H_2O that is trapped within the material, whereas a weaker peak is observed at 1630 cm^{-1} that is consistent with this assignment.

As in the Raman spectra, several O-H stretching modes are observed in the IR spectra of the α phase samples (Figure 2.10). Broad features from free H_2O are measured at 3220-3515 cm^{-1} and peaks corresponding to lattice OH and intersheet H_2O are observed at 3570-3640 cm^{-1}. The variability from structural disorder is the same as in the Raman spectra.

A combination band of the O-H stretch and a lattice mode is measured at 4260-4280 cm^{-1}. A combination of O-H stretching modes is measured at 7140 cm^{-1} (Figure 2.5 inset). Additional features are difficult to distinguish by FT-IR because of periodic interference fringes arising from the Fourier transformation.

These peak observations and assignments are summarized in Tables 2.8–2.10. My results are compared with literature values in Table 2.11.

Table 2.8 Infrared peaks for α-$Ni(OH)_2$ prepared from $NiSO_4$ [α_1][a].

Peak Frequency cm^{-1}	**Width**	**Peak Intensity**	**Peak Assignment**	
685 sh[b]	Sharp	Very weak	SO_4^{2-}	ν_2
830 sh	Sharp	Weak	α-$Ni(OH)_2$	Lattice mode combination
885	Medium	Medium	SO_4^{2-}/α-$Ni(OH)_2$	ν_4 + lattice mode combination
980 sh	Medium	Weak	Free SO_4^{2-}	ν_1
1065	Medium	Medium	SO_4^{2-}	ν_1
~1130	Medium	Medium	Free SO_4^{2-}	ν_3
1180 sh	Medium	Medium	SO_4^{2-}	ν_3
1410	Medium	Weak	α-$Ni(OH)_2$	O-H bend, lattice OH
~1620	Medium	Weak	Free H_2O	O-H bend
3650	Broad	Medium	α-$Ni(OH)_2$	O-H stretch

[a]Two samples were used in this study (see section 2.2.1).

[b]Peak maximum is near the instrumental cut-off so the exact position may be lower.

Table 2.9 Infrared peaks for α-$Ni(OH)_2$ prepared from $NiCl_2$ [α_2].

Peak Frequency cm^{-1}	Width	Peak Intensity	Peak Assignment	
670[a]	Broad	Strong	α-$Ni(OH)_2$	Lattice mode
835	Sharp	Medium	α-$Ni(OH)_2$	Lattice mode combination
1055	Medium	Medium	α-$Ni(OH)_2$	Lattice mode combination
1380	Medium	Strong	α-$Ni(OH)_2$	O-H bend, lattice OH
1480	Medium	Strong	α-$Ni(OH)_2$	O-H bend, lattice OH
1600 sh	Medium	Strong	α-$Ni(OH)_2$	O-H bend, layer H_2O
1630 sh	Medium	Medium	Free H_2O	O-H bend
2860	Sharp	Very weak	Surface hydrocarbon	C-H stretch
2930	Sharp	Very weak	Surface hydrocarbon	C-H stretch
3220 sh	Broad	Medium	Free H_2O	O-H stretch
3380	Broad	Very strong	Free H_2O	O-H stretch
3500	Medium	Strong	Free H_2O	O-H stretch
3570	Medium	Very strong	α-$Ni(OH)_2$	O-H stretch
3640 sh	Medium	Strong	α-$Ni(OH)_2$	O-H stretch
4260	Medium	Very weak	α-$Ni(OH)_2$	O-H stretch + lattice mode

[a]Peak maximum is near the instrumental cut-off so the exact position may be lower.

Table 2.10 Infrared peaks for α-$Ni(OH)_2$ prepared from $Ni(NO_3)_2$ [α_3].

Peak Frequency cm^{-1}	**Width**	**Peak Intensity**	**Peak Assignment**	
[a]650	Broad	Very strong	α-$Ni(OH)_2$	Lattice mode
720 sh	Medium	Very weak	NO_3^-	ν_4
805 sh	Medium	Weak	NO_3^-	ν_2
835	Medium	Medium	α-$Ni(OH)_2$	Lattice mode combination
992	Medium	Medium	NO_3^-	ν_1
1042	Medium	Medium	Free NO_3^-	ν_1
1280	Medium	Strong	NO_3^-	ν_3
1310 sh	Medium	Strong	NO_3^-	ν_3
~ 1340	Medium	Strong	Free NO_3^-	ν_3
~1390	Medium	Strong	α-$Ni(OH)_2$	O-H bend, lattice OH
~ 1490	Medium	Strong	α-$Ni(OH)_2$	O-H bend, lattice OH
~1600	Medium	Strong	α-$Ni(OH)_2$	O-H bend, layer H_2O
1630 sh	Medium	Medium	Free H_2O	O-H bend
~1755	Medium	Weak	α-$Ni(OH)_2$ + NO_3^-	Lattice mode + ν_3
~1970	Medium	Weak	α-$Ni(OH)_2$ + NO_3^-	Lattice mode + ν_3
~ 2485	Medium	Very weak	NO_3^-	$2\nu_3$
~2775	Medium	Weak	NO_3^-	$2\nu_3$
~3240	Broad	Medium	Free H_2O	O-H stretch
3390 sh	Broad	Very strong	Free H_2O	O-H stretch
3515 sh	Broad	Strong	Free H_2O	O-H stretch
3600-3630	Medium	Very strong	α-$Ni(OH)_2$	O-H stretch
4280	Medium	Weak	α-$Ni(OH)_2$	O-H stretch + lattice mode
7140	Medium	Very weak	α-$Ni(OH)_2$	O-H stretch combination

[a]Peak maximum is near the instrumental cut-off so the exact position may be lower.

Table 2.11 Comparison of literature values for the vibrational modes in α-$Ni(OH)_2$.

Our Peak Assignment	**Mode Frequency (cm^{-1})**	
	This Study	Literature Frequency
Raman		
Lattice mode	460	462-464 [69], 451-460 [72], 460 [73], 461 [76]
Lattice mode	495	---
2^{nd} order lattice mode	~790	---
2^{nd} order lattice mode	~1075	---
O-H bend, lattice OH	~1400	---
O-H bend, layer H_2O	1590-1620	---
O-H bend, free H_2O	1630	---
O-H stretch, free H_2O	~3240, ~3380, 3515	---
O-H stretch, lattice OH/layer H_2O	3590, 3620, 3642-3650	3625 [68], 3650-3653 [69], 3657 [72], 3656 [73], 3637 [76]
Infrared		
Lattice mode	---	400 [58], 380 [61]
Lattice mode	---	461 [25], 474 [28], 460 [58], 480 [61], 480 [63]
Lattice mode	≤ 650-670	662 [25], 645 [28], 625 [58], 650 [61], 650-655 [63]
Combination lattice mode	835	---
Combination lattice mode	1055	1055 [25]
O-H bend, lattice OH	1380-1390	1400 [25]
O-H bend, lattice OH	1480-1490	1540 [25]
O-H bend, layer H_2O	1600	1640 [25], 1650 [38], 1650 [58], 1600 [61], 1615-1620 [63]
O-H bend, free H_2O	1630	---
O-H stretch, free H_2O	3220/3240, 3380/3390, 3500/3515	~3400 [28], 3350 [38], 3350 [58], ~3500 [61], ~3500 [63], 3450 [78]
O-H stretch, lattice OH/layer H_2O	3570, 3600-3640	~3600 [28], ~3600 [61]

2.3.7. Nitrate Bands

From the XPS elemental analysis, nitrate bands are only expected in the vibrational spectra of sample α_2. Free nitrate has D_{3h} symmetry and four vibrational modes: ν_1 at 1050 cm^{-1} (A_1', IR-inactive), ν_2 at 831 cm^{-1} (A_2'', Raman-inactive), ν_3 at 1390 cm^{-1} (E'), and ν_4 at 720 cm^{-1} (E') [164]. In solution, the $\nu_1$band becomes weakly IR-active and the ν_3 band splits into a doublet at 1356 and 1410 cm^{-1}, both of which are weakly Raman-active. This split results from rotation and is therefore only expected if the chemical environment allows free rotation. Further, these bands can shift and split into additional modes when nitrate interacts with cations to form ion pairs [165].

The Raman spectra of sample α_2 show all four nitrate modes (Figure 2.7) with the most intense peak at 1047 cm^{-1} (ν_1) and the IR spectra also show all four free nitrate peaks (Figure 2.9) with the strongest peak at 1340 cm^{-1} (ν_2). The hydrated intercalation region is considered to be amorphous and can vary considerably in size, based on the variability of the c-dimension of the unit cell [34]. Since these four nitrate modes are very similar to solution nitrate, it is most likely that the nitrate ions are located in the interlayer space.

There are additional nitrate peaks close to the first three nitrate modes in the IR spectra, which implies that nitrate exists in two distinct chemical environments. It is noteworthy that the second ν_1 IR peak intensity is greater than the corresponding, hydrated nitrate peak, whereas in the Raman spectra, the additional mode is much less intense than the hydrated nitrate peak. This indicates that there are two sets of selection rules and confirms the presence of two types of nitrate, rather than peak splitting from ion-pairing effects. The change in selection rules also demonstrates that the second position in the crystal reduces the symmetry below D_{3h}. It is unclear

whether the second type of nitrate has a different orientation within the interlayer space or whether it substitutes lattice hydroxide.

Previous authors have assigned the IR peaks differently [64]. However, the relative intensities of the four modes in the Raman and IR spectra confirms that the nitrate peaks are correctly identified in the present work.

From this work, the incorporation of nitrate anions into at least two distinct chemical environments in α-$Ni(OH)_2$ can been identified by examining the Raman and IR spectra. Thus, applied research on this material will now have a method to rapidly determine any links between changes in performance or stability and the inclusion of nitrate anions in these environments.

2.3.8. Sulfate Bands

From sample preparation and XPS elemental analysis, sulfate bands are expected only in the vibrational spectra of sample α_1. The IR spectra show weak features at 980 cm^{-1} and 1120 cm^{-1} that are similar to the positions of the ν_1 and ν_3 modes of free sulfate (*cf.* 981 cm^{-1} and 1104 cm^{-1}, respectively [164]). By analogy to the nitrate bands discussed above, this may indicate that sulfate is in the hydrated interlayer space. A second pair of bands is more strongly observed in the Raman and IR spectra at 1060 cm^{-1} and 1170 cm^{-1}, which suggests that sulfate ions are incorporated in some chemical environment that shifts the peaks to higher frequency.

Additional bands, corresponding to ν_2 and ν_4 respectively, are measured by Raman at 520 cm^{-1} and both IR and Raman at 685 cm^{-1}. These are slightly higher than expected for free sulfate (*cf.* 451 cm^{-1} and 613 cm^{-1}, respectively [164]), hence, they correspond to the peaks at 1060 cm^{-1} and 1170 cm^{-1}. The Raman spectra also show a combination of ν_1 and ν_2 at 1590 cm^{-1}, however this is not observed by IR. The high degree of structural disorder hinders further investigation

and it cannot presently be concluded whether some anions are incorporated into the α-$Ni(OH)_2$ structure.

Similar to the findings for nitrate anions, my work establishes a method to measure sulfate anions in α-$Ni(OH)_2$ using Raman or IR spectroscopy. This will allow future studies to correlate the presence of sulfate anions to changes in behaviour of an electrode or catalyst.

2.3.9. Fluorescence

The strong background signal observed in the Raman spectra of both β films and sample α_1 (Figure 2.4i) indicates that the samples are fluorescent. Fluorescence is also observed from the air-formed NiO_x on the substrate but it is relatively weak. The fluorescence arises from the electronic structure of the Ni^{II} cations, which have $3d^8$ valence configurations and octahedral coordination of OH^- anions. Ideally, in the ground state ($^3A_{2g}$) the three highest occupied orbitals have t_{2g} symmetry and there are unpaired, spin-aligned valence electrons in two, singly occupied e_g orbitals. However, these orbitals can be greatly affected by small distortions of the octahedral geometry.

The crystal field splitting parameter and the Racah B parameter for β-$Ni(OH)_2$, assuming ideal octahedral geometry, have been reported: Δ_o = 9,000 cm^{-1} and B = 925 cm^{-1} [166]. Yu *et al.* present reflectance data for precipitated $Ni(OH)_2$ and observe peaks at ~670 nm and ~385 nm [39], which correspond to the ν_2 ($^3A_{2g} \rightarrow {}^3T_{1g}$) and ν_3 ($^3A_{2g} \rightarrow {}^3T_{2g}$) transitions calculated for the β phase [166]. Two additional peaks can be seen at ~740 nm and ~320 nm that are likely from α-$Ni(OH)_2$, although, the study does not provide conclusive evidence regarding this assignment [39]. Formally, the d-d transitions are forbidden by the Laporte rule, whereas such transitions are allowed if the crystal becomes asymmetric, *i.e.*, if crystal disorder increases [167]. An additional

transition is observed above 33,000 cm^{-1} (below 300 nm) that, based on its intensity, is from a charge transfer transition [39].

In the case of α-$Ni(OH)_2$, fluorescence is not observed for sample α_3, which signifies that α-$Ni(OH)_2$ is not inherently fluorescent and suggests the fluorescent background in sample α_2 may arise from disorder or changes in the electronic structure due to foreign Cl^- anions. In the case of β-$Ni(OH)_2$, both samples are fluorescent, however, they are also both partly disordered. Therefore, it is unknown whether the material is inherently fluorescent or whether more crystalline samples do not show a fluorescent background signal.

2.3.10. Disorder

The current body of literature can be simplified by considering two phases, α and β, with varying types and degrees of disorder. Turbostratic, or randomly-oriented layer, structures can occur for α-$Ni(OH)_2$ samples, where adjacent layers are separated by amorphous H_2O. Regarding β-$Ni(OH)_2$, there is one kinetically stable layer orientation that forms by stacking faults during precipitation and during aging of α to β, as observed by XRD. The anions in the Ni^{II} salt can incorporate into the α-phase, as observed by XPS, Raman and IR spectroscopy. Different degrees of hydration can occur, which is observed by large H_2O bands in the Raman and IR spectra. Finally, other factors such as crystallite size, point defects, stacking faults etc. are expected to affect the spectroscopic properties of the materials, such as whether second-order transitions appear in Raman measurements. In the case of stacking fault disorder, only the XRD peaks associated with the c-axis broaden, whereas other types of disorder cause all the diffraction peaks to broaden equally. However, the strong internal O-H stretching modes and the first order lattice transitions provide no evidence of any true additional crystal phases other than α and β.

These results show that changes in activity between samples that had previously been ascribed to the presence of intermediate phases actually arises from various types and degrees of structural disorder. By simultaneously, but separately, monitoring disorder from the incorporation of foreign ions, hydration and crystal defects such as stacking faults, changes in the performance and stability of catalysts and electrodes can be linked with their true origin. This will allow for more systematic and more directed development of improved materials for devices.

2.4. Conclusions

This work presents a unified and simplified re-examination of previous spectroscopic investigations and demonstrates that one need only consider two phases (α and β) of $Ni(OH)_2$. Highly crystalline samples of α-$Ni(OH)_2$ may be impossible to produce because its layered structure minimizes is free energy by adopting some degree of disorder. However, highly crystalline samples of β-$Ni(OH)_2$ can be prepared, although the structure can also show disorder. For the first time, all of the Raman and IR-active lattice modes of β-$Ni(OH)_2$ have been identified and assigned using factor group analysis.

Samples can range in disorder from: 1) incorporation of foreign ions, 2) hydration, and 3) crystal defects including stacking faults. The presence of foreign ions can be measured from characteristic vibrational modes, *e.g.* nitrate and sulfate anions, and/or by elemental analysis methods, such as XPS, *e.g.* chloride anions. Vibrational modes provide more detail on subtle changes in chemical environment, *e.g.* nitrate was shown to occupy two distinct chemical environments in α-$Ni(OH)_2$. Hydration affects the intensity of water bands in Raman and IR spectra. Increased disorder from crystal defects can be observed by the increased intensities of

higher order vibrational modes in Raman and IR spectra and from the strong fluorescent backgrounds in the Raman spectra. Mechanical stress within the crystal is measured by observing small shifts in frequency of the internal vibrational modes. For example, at various locations within the sample or between similar samples. Further, stacking faults in β-$Ni(OH)_2$ samples can be measured by the presence of additional O-H stretching modes at 3601 cm^{-1} and 3652 cm^{-1} in the Raman and IR spectra, respectively. This type of disorder broadens only the XRD peaks involving the c-axis, whereas other types of disorder and small crystallite effects broaden all of the diffraction peaks equally. By examining different types of disorder individually, future studies on applications of $Ni(OH)_2$ will be able to link desired behaviour with its structural origin.

Whereas thin films of α- and β-$Ni(OH)_2$ are difficult to detect or differentiate by other techniques, such as XRD and XPS, the two phases are easily distinguished from their strong internal O-H stretching modes at 3581-3640 cm^{-1}. The value of this is clear: For example, a re-examination of previous work reveals evidence of mixed samples from IR spectroscopy where XRD only detected the β-phase [25]. Thus, Raman or IR spectroscopy can be used to rapidly identify $Ni(OH)_2$ films by measuring these vibrational modes, which act as a fingerprint for pure and mixed samples.

This chapter provides the groundwork to determine which $Ni(OH)_2$ phase, or in the case of a mixture, the relative amount of each phase, is present at an electrode or catalyst surface and, therefore, to correlate desired electrochemical or catalytic behaviour to a particular phase or degree of disorder. It also establishes a method to monitor change at the surface, *i.e.*, the stability of an electrode or catalyst, during prolonged use or storage. The practical application of these results to a chemical process will be demonstrated in the next chapter.

3. Applications of *In Situ* Raman Spectroscopy for Identifying Nickel Hydroxide Materials and Surface Layers During Chemical Aging

The contents of this chapter were adapted from the following peer-reviewed journal article [116]:

Hall, D.S., Lockwood, D.J., Poirier, S., Bock, C. & MacDougall, B.R. 2014 Applications of in Situ Raman Spectroscopy for Identifying Nickel Hydroxide Materials and Surface Layers during Chemical Aging. *ACS Appl. Mater. Interfaces* **6**, 3141-3149. (doi:10.1021/am405419k).

3.1. Introduction

The previous chapter demonstrated that vibrational spectroscopy may be used to rapidly evaluate the relative amount of each phase that is present in dry samples and to determine the types and extents of structural disorder. However, it also showed that drying $Ni(OH)_2$ samples for analysis introduces stress and can cause physical damage, such as cracking [87]. Hence, this work examines practical considerations for *in situ* Raman spectroscopy on wet samples. To do this I measured Raman spectra of pure and mixed α- and β-$Ni(OH)_2$ films that were fully immersed in water immediately after preparation. For comparison, the Raman spectra of comparable dried samples in air were also measured. In the process I discovered the unexpectedly rapid conversion of α-$Ni(OH)_2$ to β-$Ni(OH)_2$ by measuring the Raman spectra, *in situ*, during film aging in water at room temperature (22 °C).

3.2. Methods

3.2.1. Material Preparation

Metallic Ni foil (Alfa Aesar, ≥ 99 %, 0.127 mm) electrodes (1 cm × 2 cm) were attached to Ni wire (Alfa Aesar, 99.9 %, 0.065 mm diameter) by electric arc welding. The wire and one end of the electrode were covered with Teflon tape. The Ni foil substrates were washed with acetone and ethyl alcohol before they were sonicated in high purity water (Millipore MilliQ, 18.2 MΩ cm). Immediately after, the substrates were cleaned in an acid bath (50 % v/v acetic acid, 30 % phosphoric acid, 10 % sulfuric acid, 10 % nitric acid, 85 ºC) for 30 s then rinsed again with excessive amounts of high purity water.

The α-$Ni(OH)_2$ films were formed by applying -2.5 mA cm^{-2} for 10 min in 0.1 M $Ni(NO_3)_2 \cdot 6H_2O$ (Alfa Aesar, ≥ 98 %). A Ni wire (10 cm long) served as a counter electrode.

Electrochemical treatments were performed using a Solartron Analytical 1470E multistat controlled with MultiStat software (v. 1.5a, Scribner Associates Inc.). The solution concentration was selected to allow for efficient precipitation as outlined in previous studies [87, 117]. The current density and deposition times were selected to form α-$Ni(OH)_2$ films expected to be sufficiently thick (~5 μm, see section 2.2.4) to be identifiable by the spectroscopic methods. The β phase sample was prepared by aging an α-$Ni(OH)_2$ sample in 30 % (w/w) KOH (Fisher Scientific, ACS certified) for 185 h at 90 °C. The β-phase sample was rinsed after aging and stored in water at 22 °C. The sample preparation is very reproducible, as discussed in chapter 2 and Ref. [87].

3.2.2. Raman Spectroscopy

The Raman measurements were performed at room temperature (22 °C) employing 1 mW of 457 nm laser light (Cobalt Twist diode-pumped solid state laser) for excitation in a backscattering geometry using the confocal microscope with a 100× objective on a Jobin-Yvon T64000 triple spectrometer operated in the subtractive mode and equipped with a back-illuminated Si charge-coupled-device detector. A relatively short excitation laser wavelength (λ) was employed to increase the experimental intensities. The Raman scattering cross-section is proportional to λ^{-4}. Further, a blue laser is expected to fully penetrate the films, some of which possess a green coloration. Sample measurements were repeated (three spectra were collected for each standard material) to ensure that weak Raman peaks (they usually were also broad peaks) could be positively identified above the background noise level at three locations on the sample. Further details of the measurements were described in section 2.2.4 and in Ref. [87]. The *in situ* Raman spectra were collected using a 100× immersion lens and the same microscope.

3.2.3. α-Ni(OH)$_2$ Film Aging

A freshly prepared α-Ni(OH)$_2$ film was thoroughly rinsed and completely immersed in high purity water at 22 °C. For the Raman measurements, the sample was periodically transferred to a Petri dish filled with high purity water such that the samples were completely immersed. The sample remained wet at all times to avoid the mechanical strain and cracking that occurs when such films dry [87]. Each measurement was repeated to ensure that Raman peaks were consistent at two locations on the sample. Immediately following each analysis, the sample was returned to the original aging container filled with water.

3.3. Results and Discussion

3.3.1. Raman Spectroscopy of Ni(OH)$_2$ Films Immersed in Water

The Raman spectra of the Ni(OH)$_2$ films, as measured in water, show the expected background water components due to backscattering from the laser beam as it traverses the water between the lens and the sample. The spectra also contain fluorescence components, which appear as broad background peaks (Figure 3.1a). The intensity of the fluorescence from β-Ni(OH)$_2$ is greater than it is from α-Ni(OH)$_2$, which is consistent with my previous observations from dry samples [87]. The convolution of the water and sample peaks makes it difficult to properly interpret the raw data as collected. In order to deconvolute the data, the fluorescence components were estimated using B-spline functions and subtracted from the raw data (Figure 3.1a). The best results were obtained by working with a frequency range that extends at least several hundred cm^{-1} above and ~1000 cm^{-1} below the water O-H stretching bands. Such fluorescence may occur when there is an electronic transition with lower energy than the

excitation laser used. Generally, the laser is absorbed and the analyte is excited into a high energy state. Following vibrational relaxation, the analyte emits a photon at the fluorescent wavelength. The fluorescence components observed in my spectra peak at 2900 – 3200 cm^{-1} in Raman shift, which corresponds to a fluorescence maximum at ~530 nm. This does not match the known visible absorption bands of β-$Ni(OH)_2$ at ~670 nm and ~385 nm [39, 166]. Thus, it is unclear whether the fluorescence from β-$Ni(OH)_2$ is intrinsic to the material or whether it arises from structural disorder. Nevertheless, fluorescent components are consistently present in the Raman spectra of β-$Ni(OH)_2$ materials [87]. It is possible to avoid the fluorescence completely by instead using an excitation laser with a longer wavelength than the known band-gap of ~670 nm (*e.g.*, 785 nm). However, as noted, the Raman scattering intensity is proportional to λ^{-4}. Thus, the use of 785 nm would reduce the Raman signal by a factor of 9, compared with the 457 nm excitation used for this work. Since several of the peaks in this work are near the detection limit, I decided that it was preferable to remove the fluorescence computationally than to reduce the instrument's sensitivity and detection limit by using a far-red or an infrared laser.

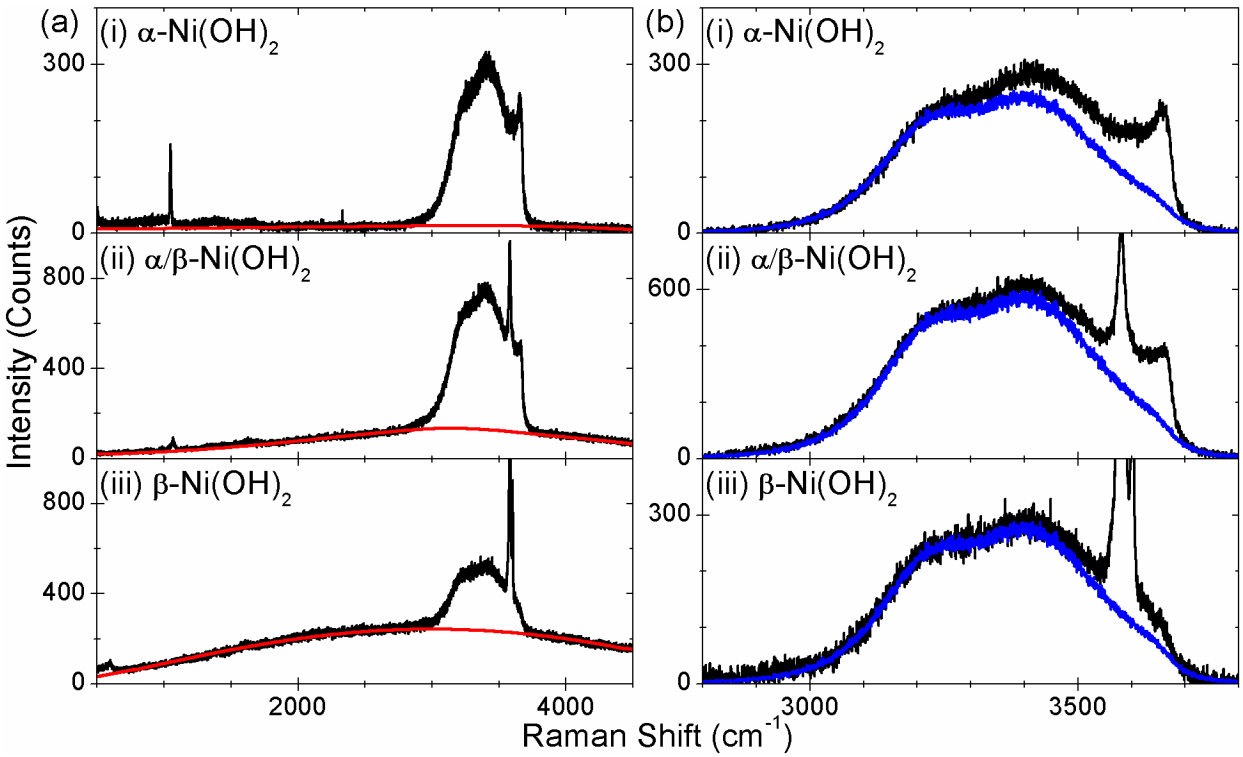

Figure 3.1 Raman spectra collected from samples immersed in water: (a) The fluorescence background components were first estimated (red) and then subtracted; (b) a reference water spectrum was then rescaled (blue) and subtracted to remove the background water components to reveal features due solely to the sample under investigation. Figure 3.2 shows the resulting spectra.

After the fluorescent components were removed, the resultant spectra contain the $Ni(OH)_2$ peaks superimposed with the water background components (Figure 3.1b). A reference water spectrum was collected under the same experimental conditions as the $Ni(OH)_2$ samples. The reference spectrum was then scaled to match the intensities of the background water components in the sample measurements by minimizing the residuals over the frequency range 2900 – 3150 cm^{-1}. The water components were then subtracted to yield the *in situ* spectra for the wet $Ni(OH)_2$ films (Figure 3.2 a). The resultant peak positions, widths and intensities match well my previous assignments for the O-H stretching modes and of α- and β-$Ni(OH)_2$ for dry samples [87]. The wet-sample results are summarized in Table 3.1.

Table 3.1 Peak frequencies and widths for the O-H stretching modes of the wet-sample spectra shown in Figure 3.2a.

	α				β			
	$\tilde{\nu}$ cm^{-1}	Width	Peak Assignment	$\tilde{\nu}$ cm^{-1}	Width	Peak Assignment		
						Mode	Parity	
(i)	~3330	broad	Layer H_2O[b]					
	~3500	broad	Layer H_2O[b]	---	---	---	---	
	3605 sh[a]	medium	Lattice OH					
	3659	medium	Lattice OH					
(ii)	~3375	broad	Layer H_2O[b]	3520	sharp	A_{1g} – acoustic	even	
	~3490 sh	medium	Layer H_2O[b]	3581	sharp	A_{1g}	even	
	3665	medium	Lattice OH	3601 sh	sharp	disordered	even	
				3629	very sharp	A_{2u} (TO)[c]	odd	
				3636	very sharp	disordered (TO)[c]	odd	
				3640	very sharp	A_{2u} (LO)[c]	odd	
				3652 sh	sharp	disordered (LO)	odd	
(iii)				3523	sharp	A_{1g} – acoustic[c]	even	
				3562 sh	sharp	A_{1g} – acoustic	even	
				3582	very sharp	A_{1g}	even	
	---	---	---	3601	very sharp	disordered	even	
				3630	sharp	A_{2u} (TO)[c]	odd	
				3640 sh	sharp	A_{2u} (LO)[c]	odd	
				3653	sharp	disordered (LO)	odd	

[a]sh = shoulder

[b]The layer H_2O modes comprise broad convolutions of several modes. Further, the reported positions of these bands vary considerably between samples [87]. Therefore, the listed peak frequencies are rather imprecise and are provided as approximate values only.

[c]The signal-to-noise ratios of these features are very low. Each reported mode was observed in three spectra collected from different areas of the samples and were identified prior to any data smoothing. Further, the positions of these modes closely agree with literature values [87]. These peaks are therefore included in this table. They were not, however, considered during further analysis of the results on account of their low intensities.

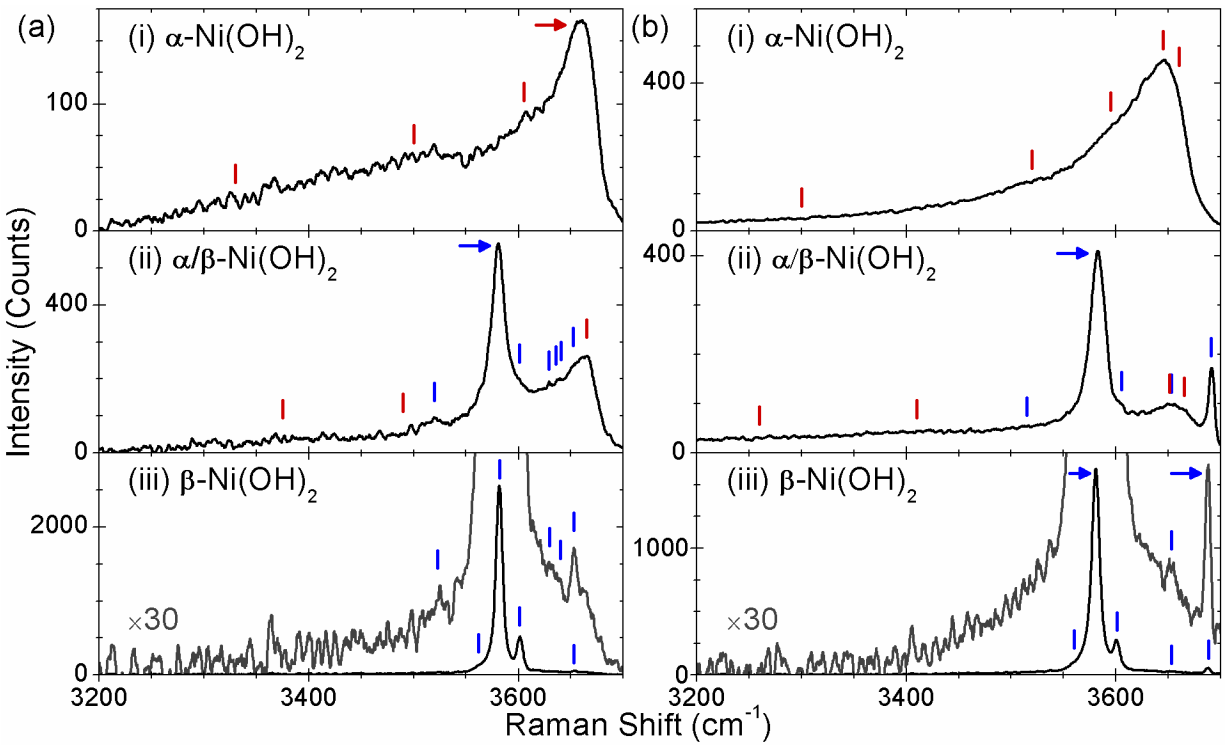

Figure 3.2 Raman spectra were collected from (a) wet samples immersed in water and (b) dry samples in air. An α-$Ni(OH)_2$ sample was electro-precipitated, transferred to water and immediately analyzed (a-i). A duplicate α-$Ni(OH)_2$ sample was prepared, immediately dried in air and then analyzed for comparison (b-i). A mixed phase sample was prepared by aging α-$Ni(OH)_2$ in room temperature water and was analyzed while still wet (a-ii). This sample was subsequently dried in air and then re-analyzed for comparison (b-ii). A β-$Ni(OH)_2$ sample was prepared by aging α-$Ni(OH)_2$ in hot KOH solution (sample β_3 in section 2.2.1). The sample was transferred to water and analyzed while still wet (a-iii). This sample was subsequently dried and then re-analyzed for comparison (b-iii). The spectra were smoothed using a Savitzky-Golay filter. The α phase and β phase components listed in Tables 3.1 and 3.2 are identified by red arrows and blue tick marks, respectively. Select spectra are enlarged by a factor of 30 to show additional detail.

All of the α- and β-phase $Ni(OH)_2$ Raman modes are now well-established and the lattice modes at frequencies < 500 cm^{-1} have been previously studied in detail [29, 66, 67, 71, 73, 77, 87, 168-170]. However, these low frequency modes are not presented or discussed here for the following reasons. It has previously been demonstrated that several of the lattice modes of α-$Ni(OH)_2$, β-$Ni(OH)_2$ and NiO overlap in mixed-phase samples. Thus, the lattice mode vibrational region can be difficult to interpret correctly when studying such mixed-phase materials, as was done here. Further, the measured Raman intensities of these modes are quite low as compared to the O-H stretching mode peaks, and they are especially so for the case of the very thin surface layers investigated here. In contrast, the well-resolved O-H stretching modes have been recommended previously for characterizing mixed-phase α- and β-$Ni(OH)_2$ samples. Further, the O-H stretching modes generally have a greater Raman scattering intensity [87], which is of particular importance for *in situ* measurements on thin films, where the signal-to-noise may be quite low. The objective of the present work is to develop reproducible methods that are applicable for a wide variety of applications, including analyses in the presence of high matrix interference or of very limited quantities of $Ni(OH)_2$. Thus, this work primarily focuses on recording and interpreting the frequency range 3000 – 3700 cm^{-1}. However, it is noteworthy that future investigations may further test the hypotheses and conclusions presented in this work by examining the lower frequency Raman modes.

To test the validity of my data treatment method, I collected Raman spectra from analogous dry samples in air for comparison purposes (Figure 3.2b). I find that there is good agreement of the Raman peak positions between the *in situ* measurements of the films immersed in water, after the background components have been removed, and the measurements of the dry films collected in air. The peak intensities, however, vary between the wet and dry samples.

These variations are readily observed by comparing the relative intensities of the α- and β-phase components from the mixed-phase sample (Figure 3.2b-i/b-ii). Further, the spectra also exhibit several subtle differences. In particular, the dry β-$Ni(OH)_2$ sample exhibits an additional mode at 3690 cm^{-1}, which has previously been attributed to a surface feature [67, 87]. Bernard *et al.* proposed that the O-H stretching mode of hydroxide groups at the surface is at higher energy than for groups opposed by adjacent layers [67]. When the sample is wetted, the surface hydroxyl groups are opposed by H_2O, *i.e.*, they become hydrated. This is expected to lower the frequency of this surface O-H stretching mode and increase the peak width, relative to a dry sample. Bernard *et al*. suggest that the frequency of hydrated surface O-H groups is similar to either the bulk O-H stretching mode (*i.e.*, A_{1g}) or to that of free H_2O [67]. This proposition is consistent with my results, since the peak at 3690 cm^{-1} is completely absent from my measurements of samples immersed in water. Furthermore, this feature is present in both the mixed α/β and pure β phase samples, but it is absent in the spectra of the pure α phase sample. Hence, I conclude that this peak corresponds to dry, *i.e.*, non-hydrated, β-$Ni(OH)_2$ surface hydroxyl groups. The α and β phase components observed in the dry-sample Raman spectra are summarized in Table 3.2.

Table 3.2 Peak frequencies and widths for the O-H stretching modes of the dry-sample spectra shown in Figure 3.2b.

	α			β			
	$\tilde{\nu}$ cm^{-1}	Width	Peak Assignment	$\tilde{\nu}$ cm^{-1}	Width	Peak Assignment Mode	Parity
(i)	3300 sh[a]	broad	Layer H_2O[b]				
	3520 sh	medium	Layer H_2O[b]				
	3595 sh	medium	Lattice OH	---	---	---	---
	3645	medium	Lattice OH				
	3660 sh		Lattice OH				
(ii)	~3260	broad	Layer H_2O[b]	3515 sh	sharp	A_{1g} – acoustic	even
	~3410	broad	Layer H_2O[b]	3583	sharp	A_{1g}	even
	3651	medium	Lattice OH	3605	sharp	disordered	even
	3665 sh	medium	Lattice OH	3653	sharp	disordered (LO)	odd
				3691	very sharp	surface	even
(iii)				3560	sharp	A_{1g} – acoustic	even
				3581	very sharp	A_{1g}	even
	---	---	---	3601	very sharp	disordered	even
				3653	sharp	disordered (LO)	odd
				3688	sharp	surface	even

[a]sh = shoulder

[b]The layer H_2O modes comprise broad convolutions of several modes. Further, the reported positions of these bands vary considerably between samples [87]. Therefore, the listed peak frequencies are rather imprecise and are provided as approximate values only.

After removing the fluorescence and background water components, the O-H stretching modes of thin $Ni(OH)_2$ films in water can be readily identified. There is no clear tendency for the absolute peak intensities under the same excitation wavelength (457 nm) and power (1 mW) to be greater for either the wet or dry samples. There are several factors that affect these absolute intensities, including differences in refractive indices between water and air as well as different optical properties of the standard and immersion microscope lenses used for the measurements. Thus, one may consider differences in the Raman scattering intensity for samples measured under the same conditions (*i.e.*, both wet or both dry) but not between the two different experimental setups. Dry β-$Ni(OH)_2$ exhibits an additional surface O-H stretching mode. However, I did not observe any loss in spectral detail by measuring the spectra *in situ*. There are several weak features included in Tables 3.1 and 3.2 that are consistent with literature values for odd-parity or combination transitions of the O-H stretching modes (*e.g.,* the disordered (LO) mode at 3653 cm^{-1}) [87]. However, these bands are scarcely above the detection limit of the instrument and are therefore of limited practical value for characterizing such thin films of $Ni(OH)_2$. In contrast, the principle Raman-active O-H stretching modes at ~3660 cm^{-1} and 3581 cm^{-1} for α- and β-$Ni(OH)_2$, respectively, have very high Raman scattering intensity. Previously, I have demonstrated that these O-H stretching bands of the lattice OH groups are sufficient for the identification of pure and mixed-phase $Ni(OH)_2$ samples *ex situ*, and that they can provide considerable structural information [87]. Hence, the results of the present work support that Raman spectroscopy has the potential to monitor structural changes during chemical or electrochemical treatments *in situ*.

3.3.2. In Situ Raman Spectroscopy of Film Aging in Room Temperature Water

To explore the practical implementation of *in situ* Raman spectroscopy on $Ni(OH)_2$ materials, I monitored the aging process of α-$Ni(OH)_2$. In alkaline media, α-$Ni(OH)_2$ slowly transforms to β-$Ni(OH)_2$.

$$\alpha - Ni(OH)_2 \cdot \frac{2}{3}H_2O \rightarrow \beta - Ni(OH)_2 + \frac{2}{3}H_2O \quad \textbf{(2)}$$

This process is well-studied in alkaline media [35] and in the mother liquor [171] after precipitation of α-$Ni(OH)_2$ by the basificatio-n of a Ni(II) salt. Further, the aging process is typically conducted at high temperatures ($T \geq 85$ °C), whereas I monitored the phase transformation in water at room temperature (22 °C). I am only aware of one previous investigation of this process in pure water. However, in order to collect X-ray diffraction and IR measurements, the researchers periodically removed and dried their samples [61]. It has since been demonstrated that drying such films causes mechanical stress and cracking [87]. 'Aging' may also refer to the transformation of an α-$Ni(OH)_2$ electrode to β-$Ni(OH)_2$ by voltammetric cycling between $Ni(OH)_2$ and NiOOH [71, 172]. My measured spectra, visible in Figure 3.3a, contain the expected fluorescence and background water components. These were estimated using the methods discussed in the previous section and then removed to produce the spectra shown in Figure 3.3b.

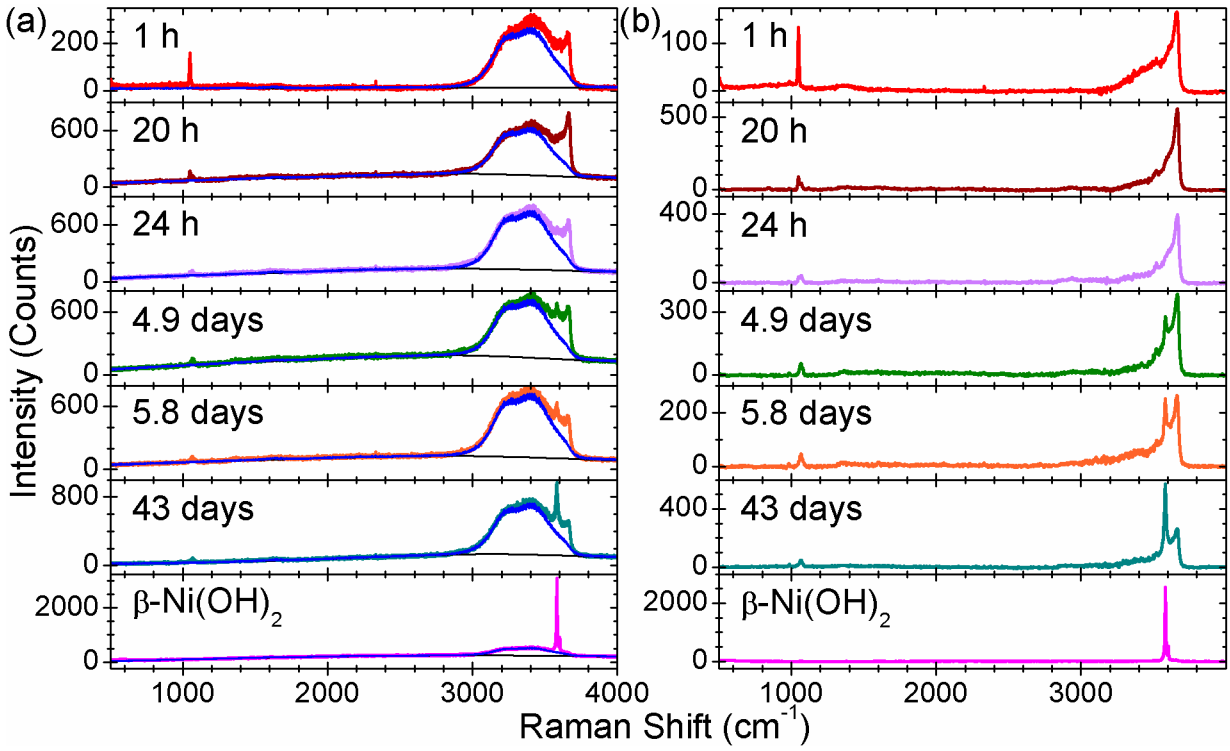

Figure 3.3 An α-$Ni(OH)_2$ film was immersed in room temperature water immediately after preparation and Raman spectra were collected periodically, *in situ*, to monitor the film aging process. A standard β-$Ni(OH)_2$ film immersed in water was analyzed for comparison. (a) The spectra are shown, as measured, and the fluorescence and background water components were estimated using the method illustrated in Figure 3.1. (b) The processed spectra are shown after the fluorescence and background water components were removed.

I previously recommended the use of the O-H stretching modes as a 'fingerprint region' for characterizing α and β-$Ni(OH)_2$ materials [87]. This region is shown expanded in Figure 3.4. The characteristic Raman modes for the α (~3660 cm^{-1}) and β (A_{1g}, 3581 cm^{-1}) phases are indicated by vertical black lines on the graph. The phase transformation is easily observed, qualitatively, from the changing relative peak areas of these α and β-$Ni(OH)_2$ modes. The α to β phase transition is quite slow in room temperature water. At higher temperatures, I expect that the interlayer water migrates out of the layers more quickly, which results in faster reaction kinetics.

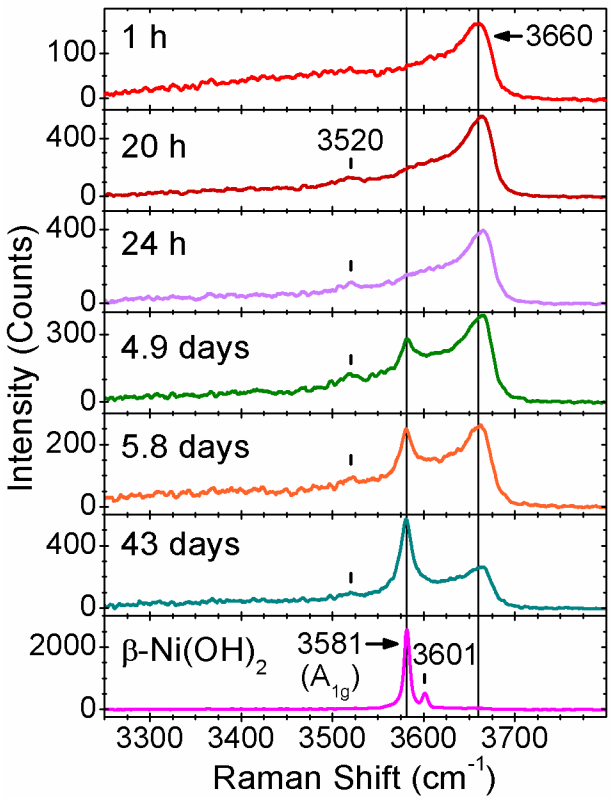

Figure 3.4 The O-H stretching region of the *in situ* Raman spectra shown in Figure 3.3b. The characteristic α-$Ni(OH)_2$ (3660 cm^{-1}) and β-$Ni(OH)_2$ (3581 cm^{-1}) O-H stretching modes are indicated by vertical black lines. Two other peaks discussed in the text are denoted by tick marks and their frequencies are indicated in the figure.

It remains unclear what role, if any, is served by using an alkaline aging solution rather than neutral water. One possibility is that by increasing the ionic strength of the solution, the thermodynamic favorability of adding water to the aging solution increases. This is analogous to the effect that electrolyte concentrations have on the osmotic pressures across a membrane. The use of a concentrated electrolyte solution for aging α-$Ni(OH)_2$ may therefore increase the energy difference between the initial and final states. According to transition state theory, if a decrease in the energy of the final state lowers the reaction rate, it must be by decreasing the rate of the reverse reaction. Thus, if the addition of an electrolyte to the aging solution indeed increases the dehydration rate, then water moves from the aging solution back into the partially dehydrated material during the aging process. However, further study is necessary to assert this conclusion with confidence. The aging process has been proposed to proceed via dissolution and subsequent re-precipitation in slightly acidic media (pH = 4 buffer solution) [64]. However, the solubility of $Ni(OH)_2$ in neutral and alkaline media ($7 < pH < 14$) is very low, which makes a dissolution/ precipitation mechanism unlikely for the samples examined in this work.

The β-$Ni(OH)_2$ A_{1g} peak, which appears at 3581 cm^{-1} after 4.9 days, is broader (FWHM $\cong$ 17 cm^{-1}) than the corresponding peak from the reference material (FWHM $\cong$ 8 cm^{-1}). Further, the peak maximum is 0.7 – 1.0 cm^{-1} below the position in the spectrum of the reference material. After 20 h, the α-$Ni(OH)_2$ peak is blue-shifted to ~3665 cm^{-1} and a broad feature appears at 3520 cm^{-1}. To explain these observations, I created a simple schematic to represent the essential geometric changes to the crystal structures during the phase transformation (Figure 3.5). I postulate that the hydroxyl groups near the α/β phase boundary are subject to compressive and tensile forces, respectively. These stresses are consistent with measured peak shifts and the broadening of the β-$Ni(OH)_2$ A_{1g} peak. I further propose that water molecules near the phase

boundary are in a new and chemically distinct environment, which may give rise to the peak at 3520 cm^{-1} and would be consistent with the disappearance of this peak after the phase transition is complete.

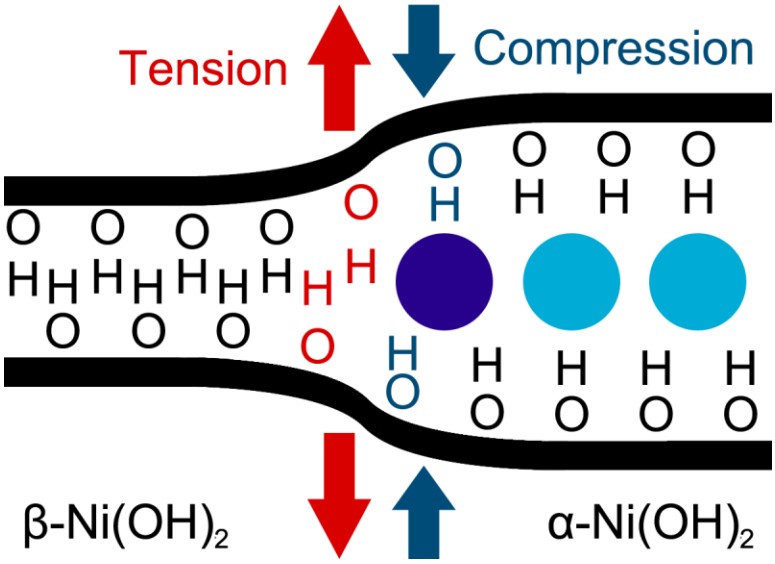

Figure 3.5 Schematic representation of the α-β phase boundary during aging. Tensile stress red-shifts the β-$Ni(OH)_2$ O-H stretching mode and compressive stress blue-shifts the α-$Ni(OH)_2$ O-H stretching mode. Water molecules situated near the phase boundary (dark blue) are expected to have different vibrational frequencies than those in the bulk α-$Ni(OH)_2$ material (light blue).

The Raman peak that corresponds to β-$Ni(OH)_2$ stacking fault disorder, at 3601 cm^{-1}, is absent in all of my measurements that were collected during aging. I may therefore conclude that either stacking faults occur at a later stage of the phase transformation or that stacking faults may be avoided by aging samples in room temperature water.

This work primarily focuses on the O-H stretching modes because of their high Raman scattering intensity, relative to the lower frequency lattice modes. However, it is known that counterions from precursor salts used for precipitation, such as nitrate anions from the $Ni(NO_3)_2$ used in this study, are often incorporated into the α-$Ni(OH)_2$ structure during synthesis. Further, nitrate anions incorporated into the α-$Ni(OH)_2$ structure have been observed as intense, prominent features in the vibrational spectra of $Ni(OH)_2$ materials previously [64, 87]. After 1 h of aging, I observe a peak at 1049 cm^{-1} (Figure 3.6), which matches the ν_1 stretching mode of free nitrate, *i.e.*, the fully dissociated solution species [164]. At 20 and 24 h, I observe a peak at 845 cm^{-1}, which corresponds with the ν_2 mode of free nitrate [164], and a weak feature at 1120 cm^{-1}, which I attribute to a combination that involves a nitrate mode. For example, the nitrate ν_4 mode (720 cm^{-1}) and an IR-active lattice mode of α-$Ni(OH)_2$ (380 – 400 cm^{-1}) [58, 61] could yield a Raman-active combination at 1120 cm^{-1}. The emergence of the ν_2 and combination modes indicates that aging introduces structural disorder that relaxes the selection rules.

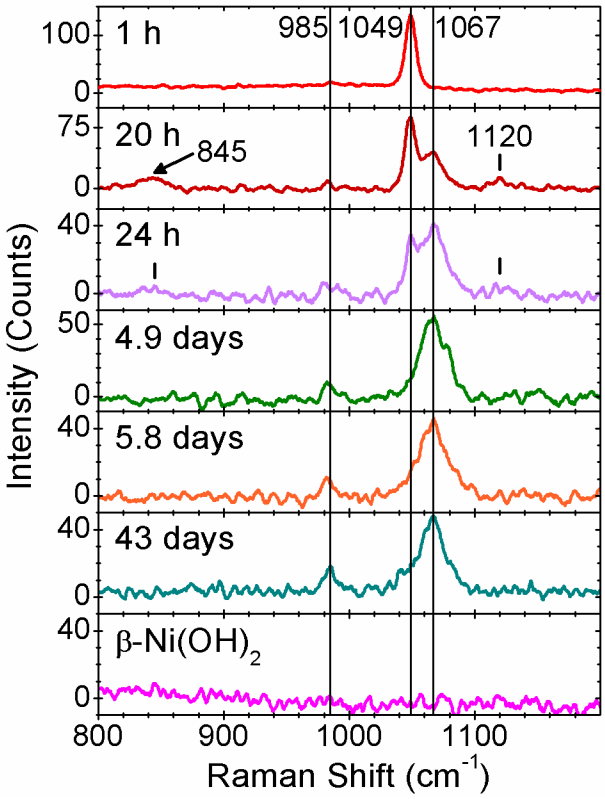

Figure 3.6 The intermediate frequency range of the *in situ* Raman spectra shown in Figure 3.3b. The peaks at 985 cm^{-1}, 1049 cm^{-1} and 1067 cm^{-1} are indicated by vertical black lines. Two other peaks discussed in the text are denoted by tick marks and their frequencies are indicated in the figure.

I previously suggested that nitrate anions sit within the intercalated water planes of the α-$Ni(OH)_2$ structure (section 2.3.7 and Ref. [87]). In fact, the peak frequencies in the present measurements are closer to those of the free nitrate anion than the spectra that I reported from dry samples. For example, the ν_1 mode of free nitrate is at 1050 cm^{-1} and I measured a peak at 1049 cm^{-1} from these wet samples, whereas from dry samples I previously reported a peak at 1047 cm^{-1} [87, 164]. Further, the nitrate peaks from dry samples were broader than I observe from my wet samples and than is typical of free nitrate bands. Thus, there is greater similarity between nitrate in the interlayer space and in solution for wet samples than there is for dry samples. This supports a model in which, for dry samples, the interlayer water molecules are 'frozen' in place, whereas for wet samples, the intercalated water has a certain amount of mobility that resembles solution.

I further postulated that nitrate anions may also occupy lattice hydroxyl sites, which corresponded to an additional set of nitrate peaks. These peaks, notably the intense ν_1 mode at ~997 cm^{-1}, are, however, absent from all of the spectra in the present work, which may indicate that nitrate is quickly (< 1 h) expelled from the lattice hydroxyl positions and replaced by hydroxide anions from the interlayer water.

The ν_1 mode intensity decreases considerably over the first 24 h of aging and no nitrate peaks are visible after 4.9 days. This rapid removal of the nitrate anions indicates a relatively high diffusivity, which further supports the hypothesis that nitrate impurities reside within the loosely defined hydration planes rather than tightly bound lattice sites in the $Ni(OH)_2$ sheets. During the same time period, the intensity of the α-$Ni(OH)_2$ O-H stretching mode more than triples (Figure 3.4). This indicates that early into the aging process, the presence of nitrate anions in the intercalation space creates structural disorder that decreases the O-H stretching mode

intensity. For example, one can imagine that the substitution of water molecules with large nitrate anions would warp and deform the $Ni(OH)_2$ sheets along the crystallographic c-axis. The high potential energy of this proposed initial state is expected to make the structure relatively unstable and, hence, may explain the quickness of the nitrate anions' expulsion.

After 20 h, I observe a previously unreported peak at 1067 cm^{-1} (Figure 3.6). After the peak's initial appearance, its position, intensity and width are approximately constant over 43 days of aging. Although the peak is close to the ν_1 stretching mode of free carbonate at 1063 cm^{-1} [164], I do not observe any other carbonate modes. Further, the peak is sharper than is typical of combination modes. Hence, I propose that this peak corresponds to a Raman-allowed second order transition of the E_u (TO) β-$Ni(OH)_2$ mode, which has been reported at 520 – 550 cm^{-1} [87]. I also observe a peak at 985 cm^{-1}, which I attribute to the second order transition of the IR-active α-$Ni(OH)_2$ lattice mode at 495 cm^{-1} [87].

In summary, I applied *in situ* Raman spectroscopy to monitor the conversion of α-$Ni(OH)_2$ to β-$Ni(OH)_2$ in room temperature water. The need to dry the samples for analysis was avoided by performing the measurements *in situ*. The aging reaction was easily monitored using the characteristic O-H stretching modes for α- and β-$Ni(OH)_2$ at 3660 cm^{-1} and 3581 cm^{-1}, respectively. The high Raman scattering intensity of these two modes makes them ideal for monitoring chemical and electrochemical processes, even on very thin samples. The dehydration process introduced lattice stress, caused the appearance of higher order lattice modes (985 cm^{-1} and 1067 cm^{-1}), blue-shifted the α-$Ni(OH)_2$ O-H stretching mode, and red-shifted and broadened the β-$Ni(OH)_2$ A_{1g} mode. I propose a simple schematic of the phase boundary and consider mechanical forces to explain these observations and to predict a new, intermediate water O-H stretching mode, which I ascribe to a new peak observed at 3520 cm^{-1}. Nitrate anions that were

incorporated in the α-$Ni(OH)_2$ structure during electrochemical precipitation were mostly removed after a day, which indicates that they have high diffusivity and supports the hypothesis that nitrate anions sit within the intercalation space.

Although the details of the aging process may be more fully examined by measuring all of the Raman modes, including the less intense, lower frequency lattice modes, this work demonstrates that considerable information may be practically attained from $Ni(OH)_2$ materials by measuring only the most intense modes. In particular, the identification of the α- and β-$Ni(OH)_2$ components (from the modes at 3660 cm^{-1} and 3581 cm^{-1}, respectively), the identification of stacking fault disorder in the β-phase (from the mode at 3601 cm^{-1}), the general structural disorder (from O-H stretching mode widths, especially for the β-phase), and the incorporation of polyatomic ions (*e.g.*, the intense nitrate ν_1 band at ~1050 cm^{-1}) may be precisely measured in real-time. On account of the high Raman intensity of all of these spectral features, the methods presented in this work may be implemented even for very minute amounts of material or in the presence of very high matrix interference. Future work may extend the application of *in situ* Raman spectroscopy to $Ni(OH)_2$ materials to include the measurement of ultrathin surface layers ($< 10^{-7}$ m) and the less intense lattice modes. Previous work has successfully utilized surface-enhanced Raman spectroscopy (SERS) to measure such ultrathin $Ni(OH)_2$-containing materials and surface layers, including several of the lattice modes [46, 71, 73, 169, 170]. However, the relative SERS mode intensities are generally difficult to predict and can vary considerably from IR and Raman spectroscopy. Therefore, future spectroscopic investigation utilizing SERS, beyond the scope of the present work, may allow the hypotheses and conclusions presented in this article to be further scrutinized.

3.4. Conclusions

In situ Raman spectra were collected and processed from $Ni(OH)_2$ films that were fully immersed in water. The fluorescence and background water spectral features that were also observed can be removed, in that order, using typical spreadsheet or graphical analysis software. The resultant spectra are similar, but non-identical, to those obtained from comparable dry samples. Notably, dry β-$Ni(OH)_2$ samples exhibit an additional feature at 3690 cm^{-1} from surface O-H stretching modes. Although the absolute peak intensities vary between wet and dry samples, there was no loss in spectral detail from measuring the samples wet. Thus, Raman spectroscopy is suitable for measuring structural changes *in situ* during chemical or electrochemical treatments.

Raman spectroscopy was applied to monitor the spontaneous conversion of α-$Ni(OH)_2$ to β-$Ni(OH)_2$ in room temperature water. By monitoring this aging process *in situ*, I avoided the physical damage that would have resulted from drying samples for analysis. The transformation from α- to β-$Ni(OH)_2$ was easily monitored from the relative intensities of the characteristic O-H stretching modes at 3660 cm^{-1} and 3581 cm^{-1}, respectively. Nitrate anions that were incorporated in the α-$Ni(OH)_2$ structure during electrochemical precipitation were mostly removed after a day. The dehydration process introduced lattice stress, as evidenced by the appearance of higher order lattice modes (985 cm^{-1} and 1067 cm^{-1}), the blue-shift of the α-$Ni(OH)_2$ O-H stretching mode, and the red-shift and broadening of the β-$Ni(OH)_2$ A_{1g} mode. I propose a schematic of the α-β phase boundary during aging (Figure 3.5) and predict a new water O-H stretching mode, which may be ascribed to a new peak at 3520 cm^{-1}. Although this aging process is conventionally performed in concentrated alkaline media at high temperature, I observe it also occurs quite simply in room temperature water. The α to β phase transition is quite slow at room temperature,

which demonstrates the necessity for elevated temperatures. It remains uncertain what role is served by using an alkaline aging solution, although the presence of an electrolyte may serve to lower the energy of the product.

To date, my work on $Ni(OH)_2$ materials has demonstrated the potential for vibrational spectroscopy to provide information on the proportions of α- and β-$Ni(OH)_2$ and their fine structural details with high sensitivity. FT-IR may be utilized to rapidly characterize dry $Ni(OH)_2$, whereas Raman spectroscopy offers greater spectral resolution and is well-suited for *in situ* measurements. Considerable information may be attained from only the most intense Raman modes, making these methods suitable even for very minute amounts of material or in the presence of high matrix interference.

4. Electrochemistry of Metallic Nickel in Alkaline Media

The contents of this chapter were adapted from the following peer-reviewed articles [40, 173]:

Hall, D.S., Bock, C. & MacDougall, B.R. 2013 The Electrochemistry of Metallic Nickel: Oxides, Hydroxides, Hydrides and Alkaline Hydrogen Evolution. *J. Electrochem. Soc.* **160**, F235-F243. (doi:10.1149/2.026303jes).

Hall, D.S., Bock, C. & MacDougall, B.R. 2013 Surface Layers in Alkaline Media: Nickel Hydrides on Metallic Nickel Electrodes. *ECS Trans.* **50**, 165-179. (doi:10.1149/05031.0165ecst).

4.1. Introduction

A problem faced by Ni-based electro-catalysts is that the hydrogen evolution reaction (HER) activity of Ni cathodes is significantly greater on fresh electrodes than after several hours of electrolysis [13-18]. To investigate the decrease in HER activity during alkaline electrolysis, this chapter examines the electrochemistry of smooth metallic Ni electrodes in basic solutions near the reversible hydrogen electrode (RHE) potential. By using smooth electrodes, I establish the electrode processes that are also expected to occur on high surface area Ni catalysts. I also avoid the instrumental complications that arise due to very large currents, which are typical for high surface area electrodes.

Furthermore, industrial electrolysers are often subject to transient current reversal, especially during initiation and shut-down. It is important to evaluate whether temporary anodic currents at a Ni catalyst will have adverse short- or long-term effects on its HER activity. Hence, this study also considers the electrode processes on smooth Ni electrodes up to 1.6 V_{RHE}, which is well into the oxygen evolution reaction (OER) region, and probes whether the Ni catalyst can be returned back to its original state.

Years of investigation have provided many clues to the identification of the electrochemical reactions on metallic Ni in basic media and yet these electrode processes have remained uncertain. The voltammetric features in these conditions have been attributed to the oxidation and reduction of nickel hydrides [18, 135-137], nickel oxides and nickel hydroxides [37, 149, 174-178]. In this work, I intend to present a clarified interpretation of the electrode processes on Ni in alkaline media that is supported by voltammetric, XRD and X-ray photoelectron spectroscopy (XPS) experiments as well as the published literature. The identification of the electrochemical reactions that occur at high currents and in strong alkaline

media is believed to provide the basis for the consideration of methods that will improve the activity and stability of the electrodes.

4.2. Experimental Methods

4.2.1. Electrode Preparation

All voltammetric experiments used electrodes prepared from a metallic Ni rod (Alfa Aesar, ≥ 99 %, 3.2 mm diameter) embedded in epoxy resin so that only one flat, circular face was exposed to the electrolyte solution. All XPS experiments used metallic Ni foil (Alfa Aesar, 99.5 %, 0.787 mm thick) electrodes (1 cm × 2 cm). Electrodes were mechanically polished using 320 grit SiC paper followed by 9 μm polycrystalline diamond, 3 μm polycrystalline diamond (Buehler MetaDi Supreme) and 0.05 μm Al_2O_3 (Buehler MasterPrep) suspensions. XPS electrodes were then attached to Ni wire (Alfa Aesar, 99.9 %, 0.065 mm diameter) by electric arc welding. Electrodes were rinsed and sonicated in high purity water (Millipore Milli-Q, 18.2 MΩ cm).

All X-ray diffraction (XRD) measurements used metallic Ni foil (Alfa Aesar, ≥ 99 %, 0.127 mm) electrodes (1 cm × 0.5 cm) that were attached to Ni wire by electric arc welding. The electrodes were washed with acetone, washed with ethyl alcohol and then sonicated in high purity water (Millipore Milli-Q, 18.2 MΩ cm). Immediately after, the substrates were cleaned in an acid bath [50 % (v/v) acetic acid, 30 % phosphoric acid, 10 % sulfuric acid, 10 % nitric acid, 85 °C] for 30 s and then rinsed again using excessive amounts of high purity water.

4.2.2. Electrochemical Experiments

For the 0.1 M KOH and 1 M NaOH solutions, a standard three-compartment glass cell was used while for the 30 % (w/w) KOH solution, a three-compartment Teflon cell was utilized. The working compartment was air-tight and purged with Ar gas (grade 5.0) or electrolytically generated H_2 gas (Parker Hannifin H2PEM-165L, 99.9999 %). A Pt foil (≥ 3 cm^2) served as the counter electrode. For the galvanostatic experiments, a saturated calomel electrode (SCE) served as the reference electrode [E = -1.158 V_{RHE} (30 % KOH)/E = -1.064 V_{RHE} (1 M NaOH)] and for the voltammetric experiments, a Hg/HgO reference was prepared with the same solution as the bulk electrolyte (E = -0.926 V_{RHE}). The RE was separated from the working compartment by a Luggin capillary. In the glass cell, the CE and RE compartments were separated from the working compartment by glass frits.

Voltammetric measurements were performed using a Solartron Analytical 1470E multistat controlled with MultiStat software (v. 1.5a, Scribner Associates Inc.). Galvanostatic treatments were performed using a Solartron Analytical 1287 potentiostat with CorrWare software (v. 3.3c, Scribner Associates Inc.).

Electrochemical impedance spectroscopy (EIS) measurements were conducted to estimate the Ohmic drop of the voltammetric measurements and were performed using a Solartron 1260 controlled with ZPlot (v. 3.3c, Scribner Associates Inc.). Data was fit to an equivalent circuit consisting of solution resistance (R_s) in series with parallel charge transfer resistance and double layer elements to estimate the Ohmic loss (IR drop). A constant-phase element was used for the double layer to account for the expected frequency dispersion [179]. The data fit the published generalized model well and the R_s was in the range 2 – 3 Ω.

4.2.3. X-ray Diffraction (XRD)

Following electrochemical treatments, samples were rinsed with high purity water and immediately transferred to a Bruker AXS low background, air-tight sample holder (A100B138-B141) that was purged with Ar. Samples were analyzed using a Bruker AXS D8 DISCOVER diffractometer. Fixed incidence (5°) measurements were taken at 0.02° point^{-1} and 3 s point^{-1} using a Cu Kα X-ray source [$\lambda(K\alpha_1)$ = 1.541 Å; $\lambda(K\alpha_2)$ = 1.544 Å].

4.2.4. X-ray Photoelectron Spectroscopy (XPS)

Samples were analyzed with a Kratos Analytical Axis Ultra DLD equipped with a mono Al Kα X-ray source. High-resolution spectra of the Ni 2p and the C 1s regions were collected at 20 eV pass energy. All spectra were collected at a 54° take-off angle. Spectra were processed with CasaXPS (v. 2.3.16dev95, Casa Software Ltd.) using Shirley background corrections and the Ni 2p peak positions and widths for Ni metal, NiO, β-$Ni(OH)_2$ and for the β-NiOOH decomposition product, $Ni_3(OH)_4O_2$, reported by Biesinger *et al* [159]. The qualitative differences between the Ni 2p peaks for α and β-$Ni(OH)_2$ reported by Hall *et al.* were considered [87]. Measured binding energies were adjusted to compensate for the shift that arises from a buildup of electrostatic charge by setting the adventitious hydrocarbon C 1s peak to a binding energy of 284.8 eV [159].

4.3. Results and Discussion

4.3.1. Nickel Absorption and Nickel Hydrides

The HER activity was measured on a freshly polished Ni electrode and on Ni that was held for 2 – 4 h at -1 V_{RHE} (uncorrected for Ohmic loss) to establish that electrode deactivation

occurs (Figure 4.1). Freshly polished electrodes show a large degree of variability, possibly introduced by the rapid blocking of the electrode surface by H_2 gas bubbles and by the rapid HER deactivation process. Near the RHE potential, the slope of the overpotential against logarithmic current density for a slow potential sweep [1 mV s^{-1} starting at -1 V_{RHE} (IR uncorrected)] is ~200 mV dec^{-1} and the exchange current density is ~10^{-3} A cm^{-2}. After 2 – 4 h of H_2 evolution at -1 V_{RHE} (IR uncorrected), the slope near the RHE potential is largely unaffected. However, the intercept decreases by an order of magnitude to ~10^{-4} A cm^{-2}. At potentials below -0.5 V_{RHE}, the slope is ~400 mV dec^{-1}. The presence of two slopes may indicate different reaction pathways in each potential range or it may indicate different rate-determining steps for a single, multi-step reaction pathway. After 12 – 24 h of H_2 evolution, the slope is about 400 mV dec^{-1} over the entire potential range and the intercept is ~10^{-3} A cm^{-1}. This indicates that the surface state is completely changed and it may be possible that only one reaction pathway occurs. It is noteworthy that the results below -0.4 V_{RHE} are very similar after 2 – 24 h of H_2 evolution, which may indicate that the reaction pathways and rate-determining steps are the same in this potential range. The results from these measurements cannot be considered true Tafel parameters, because they were measured by a slow scan rather than steady-state polarization. Furthermore, slopes greater than 120 mV dec^{-1} at room temperature are anomalously high, rather than true Tafel, slopes. However, these results demonstrate that electrode deactivation can negatively affect the HER on Ni cathodes by an order of magnitude or more after just one day of electrolysis. The transition between reaction pathways confirms that the chemical state of the electrode surface changes in the HER region. To determine the source of electrode deactivation, I discuss voltammetric and *ex situ* surface characterization results and consider the possible electrode processes within the HER region.

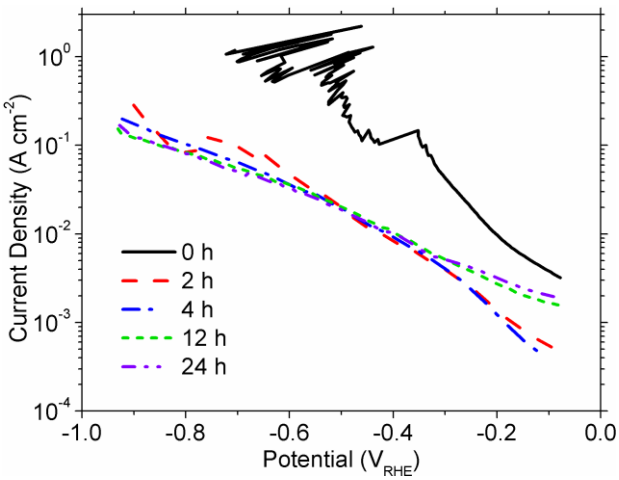

Figure 4.1 The HER activity of a freshly polished Ni electrode and Ni electrodes held at -0.5 A cm^{-2} for various time periods as measured at 1 mV s^{-1} in H_2-purged 30 % (w/w) KOH. The Ohmic loss (IR drop) was estimated

The standard reduction potentials for several possible electrode processes near and below the RHE potential were summarized to consider the source of the electrode deactivation (Table 4.1, Figure 4.2). I do not include a potential for α-$Ni(OH)_2$ because its value has not been reported. However, it is known that α-$Ni(OH)_2$ transforms to β-$Ni(OH)_2$ in alkaline media [87]. Because this aging process is spontaneous, the free energy must decrease, *i.e.*, $\Delta G < 0$, and it is concluded that the reduction potential of α-$Ni(OH)_2$ is positive to that of β-$Ni(OH)_2$.

I have established several regions of interest during voltammetry, indicated numerically in Figure 4.3, which will be referenced throughout the remainder of this work. Cyclic voltammetry (CV) on Ni in 0.1 M to 30 % (w/w) KOH and in 0.1 M to 1 M NaOH solutions are nearly identical when using a pH-independent reference electrode, although minor shifts in peak positions have been reported for different concentrations [176]. The cathodic peak (9) in Figure 4.3b is highly-dependent on the upper potential limit, hence it is not observed in Figure 4.3a, as further discussed in section 4.3.2.

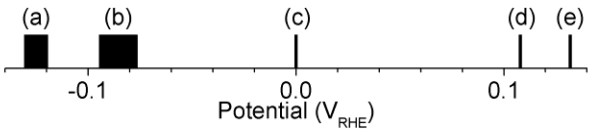

Figure 4.2 Reduction potentials of electrode processes close to the RHE potential. The letters correspond to the half-reactions listed in Table 4.1.

Table 4.1 Reversible electrode potentials for processes discussed in this study. Potentials are separated by a slash, where there is a range of possible values. The letters (first column) correspond to Figure 4.2.

	Potential V_{RHE}	**Reaction**	**Ref.**
(a)	-0.12/-0.13	$Ni_{(s)} + x\ H_2O_{(l)} + x\ e^- \rightleftharpoons \beta\text{-}NiH_{x(s)} + x\ OH^-_{(aq)}$, $x = 0.60 - 0.65$	[180]
(b)	-0.075/-0.095	$Ni_{(s)} + x\ H_2O_{(l)} + x\ e^- \rightleftharpoons \alpha\text{-}NiH_{x(s)} + x\ OH^-_{(aq)}$, $x = 0.01 - 0.03$	[180]
(c)	0.000	$2\ H_2O_{(l)} + 2\ e^- \rightleftharpoons 2\ OH^-_{(aq)} + H_{2(g)}$	
(d)	0.108[a]	$\beta\text{-}Ni(OH)_{2(s)} + 2\ e^- \rightleftharpoons Ni_{(s)} + 2\ OH^-_{(aq)}$	[181, 182]
(e)	0.132[b]	$NiO_{(s)} + H_2O_{(l)} + 2\ e^- \rightleftharpoons Ni_{(s)} + 2\ OH^-_{(aq)}$	
	1.229	$O_{2(g)} + 2\ H_2O_{(l)} + 4\ e^- \rightleftharpoons 4\ OH^-_{(aq)}$	
	1.37/1.40[c]	$\beta\text{-}NiOOH + H_2O_{(l)} + e^- \rightleftharpoons \beta\text{-}Ni(OH)_{2(s)} + OH^-_{(aq)}$	[80]

[a]The measurement predates the discovery of α-$Ni(OH)_2$ in 1966 [26], so it is assumed that the researchers used high purity, crystalline β-$Ni(OH)_2$.

[b]Calculated from the free energies of formation of $NiO_{(s)}$ and $H_2O_{(l)}$ [183, 184]. The potential for non-stoichiometric NiO_x is expected to be different.

[c]The exact potential depends on the structural order of the electrode material.

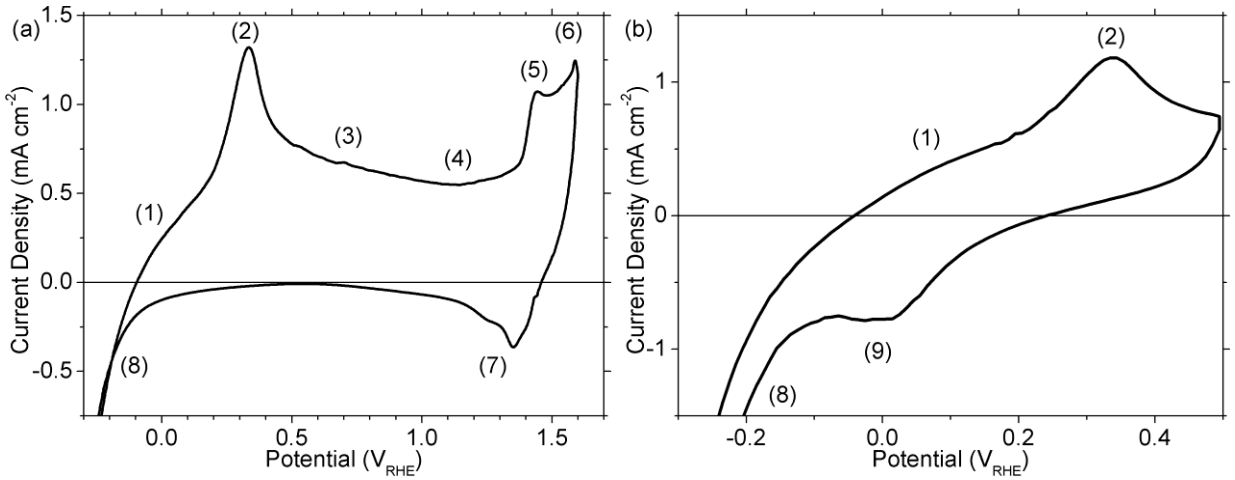

Figure 4.3 CVs of freshly polished Ni electrodes held at -300 mV_{RHE} for 60 s then scanned at 100 mV s^{-1} in Ar-purged 0.1 M KOH to upper potential limits of (a) 1.6 V_{RHE} and (b) 0.5 V_{RHE}. The numbers denote the voltammetric regions discussed throughout this work.

The anodic processes in regions (1) and (3) are found to be affected by the cathodic pre-treatment of the electrode prior to potential cycling. If the electrode is held at a potential negative to that of the RHE, the anodic current densities at regions (1) and (3) increase with longer holding times whereas the actual charge associated with peak (2) appears largely unaffected (Figure 4.4). For initial holding times longer than ~10 min, at -300 mV_{RHE}, the change in anodic current density of region (3) is less pronounced, although a very diffuse peak is observed at ~0.8 V_{RHE}. At such long holding times, the anodic charge at peak (2) appears to decrease slightly. However, this decrease may arise from the changing shape of the large background current that spans regions (1) and (3).

Furthermore, the anodic current densities in regions (1) and (3) also depend on the initial potential chosen for the CVs (Figure 4.5). For initial potentials below -0.1 V_{RHE}, the charge associated with peak (2) reaches a maximum. In contrast, the current densities in regions (1) and (3) increase as the starting potential decreases. For starting potentials positive to 0.2 V_{RHE}, the anodic peak (2) is completely absent. Similar results on the effect of the initial potential and holding times on the voltammetry of Ni electrodes have been reported using 1 M KOH [177] and 0.5 M NaOH solutions [131].

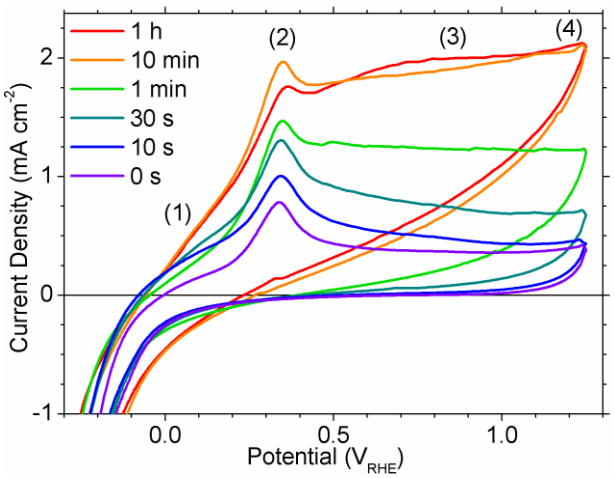

Figure 4.4 Freshly polished Ni electrodes were held at -300 mV_{RHE} for various periods then scanned at 100 mV s^{-1} in Ar-purged 0.1 M KOH. The numbers denote the voltammetric regions discussed throughout the text.

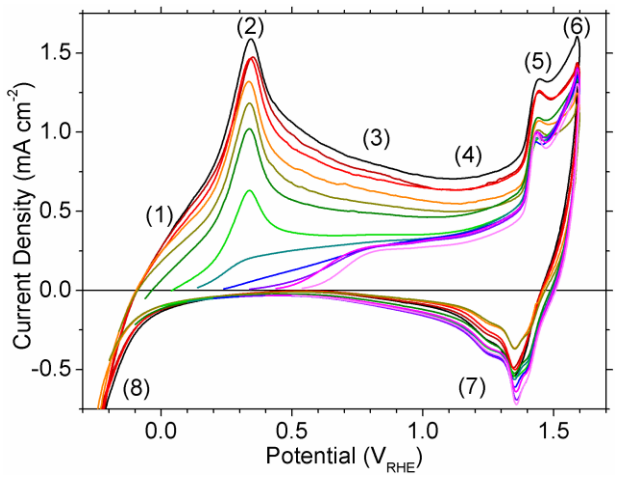

Figure 4.5 Freshly polished Ni electrodes were held at -600 $mV_{RHE} \leq E \leq +500$ mV_{RHE} for 60 s then cycled at 100 mV s^{-1} in Ar-purged 0.1 M KOH.

The anodic currents in the regions (1), (2) and (3) are sometimes attributed to the formation of a nickel oxide or hydroxide film of limited thickness [13, 37, 174-176, 178, 181, 185]. The observed properties of voltammetric peak (2) are consistent with this argument (see section 4.3.2), but this explains neither the dependence of the current density of regions (1) and (3) on the cathodic pre-treatment time and potential nor the breadth of these anodic features. Thus, I consider an alternate explanation, namely, the incorporation of hydrogen into the Ni metal [14, 18, 137, 186]. The amount of hydrogen incorporated into the material depends on the time and rate of its absorption, the latter of which depends on the cathodic overpotential. Upon scanning the potential to more positive values, the incorporated hydrogen is oxidized at the electrode surface. This process is limited by the solid-state diffusion of hydrogen to the surface and, thus, a broad voltammetric feature is observed rather than a well-defined peak. I observe that the current density of the oxidation process in region (3) is approximately proportional to the scan rate raised to the exponent of 0.83 (Figure 4.6a). This scan-rate dependence neither fits a surface process (exponent of unity) nor a process that is limited by linear diffusion (exponent of one half). Gravimetric measurements, collected with an electrochemical quartz crystal microbalance (EQCM), have shown that the electrode mass decreases during a forward potential sweep in region (1), which supports the proposal that incorporated H is removed from the structure in this region. During potential cycling in this general potential range, gravimetric measurements form a closed loop, which indicates that no electrode dissolution occurs. This study also showed that alkali cations are not involved in the surface electrochemistry below ~1.2 V_{RHE} [187]. This allows free comparison between experiments in NaOH and KOH solutions, although ionic strength differences, and thus differences in the activity of OH^-, are relevant at very high concentrations [188].

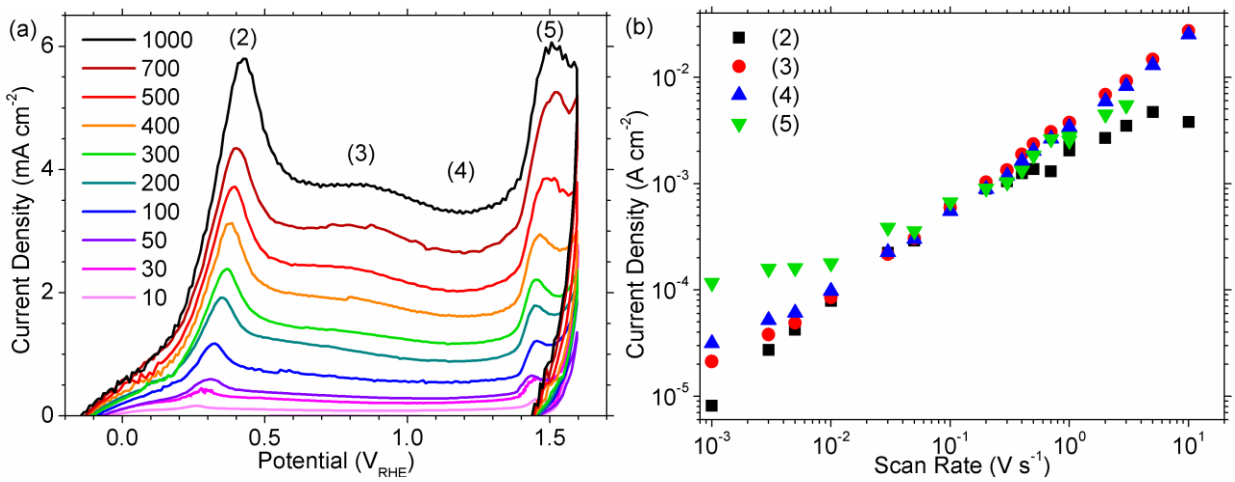

Figure 4.6 Freshly polished Ni electrodes were held at -300 mV_{RHE} for 60 s then scanned positive at different rates in Ar-purged 0.1 M KOH. (a) Current-potential profiles with the scan rates indicated in mV s^{-1}. (b) The current density of the first anodic peak [(2), ■], 850 mV_{RHE} [(3), ●], 1200 mV_{RHE} [(4), ▲] and the second anodic peak [(5), ▼] recorded during the forward scan.

From the hydrogen absorption model presented thus far, one would expect that if the forward scan is reversed within region (3), the anodic current will not immediately cease since it is primarily controlled by diffusion rather than by the overpotential. The current density is seen to drop quickly on scan reversal. However, the current remains anodic during the reverse scan (Figure 4.7), which is consistent with oxidation of incorporated H. The hydrogen oxidation current after reversal is larger for electrodes initially held longer in the cathodic potential region, which can be explained by an increase in hydrogen content (Figure 4.4). The remainder of the anodic current during the forward scan in region (3) is attributed to a concurrent anodic process, which is potential-dependent. This is partially explained by the existence of variable, potential-dependent stable hydrogen concentrations as proposed by Conway *et al* [137] and previously measured for pure and mixed α/β-NiH_x electrodes below -100 mV_{RHE} [180]. However, this alone seems insufficient to rationalize the potential-dependence and, hence, I propose that oxidation of the nickel metal also contributes to the net anodic current within region (3), which further complicates the scan-rate dependence observed in Figure 4.7. This oxidation process is discussed in detail in section 4.3.2.

To recover the oxidation currents in regions (2) and (3) after the first cycle, one must scan to sufficiently negative potentials (Figure 4.7). Note that the current density in region (3), proposed to correspond to the oxidation of absorbed hydrogen, is not fully restored even when the lower scan limit is the same as the initial potential. This is because I did not hold the electrodes at the negative limit after the first cycles and, thus, the amounts of hydrogen in the electrodes was lower than during the initial scans.

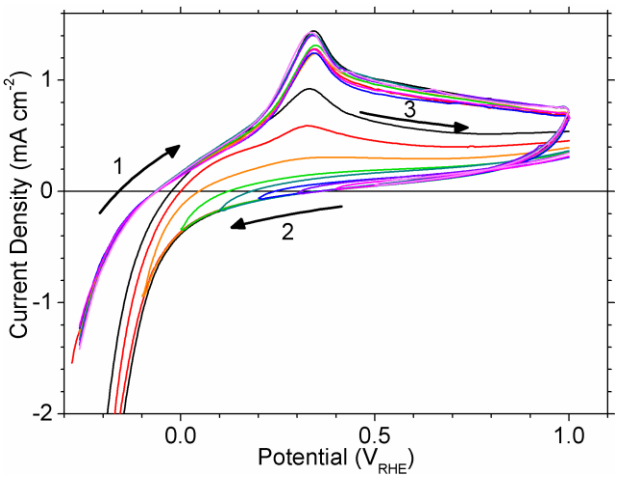

Figure 4.7 Ni electrodes were held at -0.3 V_{RHE} for 60 s then cycled at 100 mV s^{-1} in Ar-purged 0.1 M KOH. The scan direction was reversed at various lower limits.

The incorporation of H into Ni electrode materials has been proposed to occur by either H permeation into interstitial sites in the Ni metal [17, 186, 189, 190] or by a phase transition to a nickel hydride [18, 131, 135-137]. However, there is some dispute regarding whether a true bulk hydride phase can be formed under these conditions [133]. There are two bulk phases, α and β, which draw their nomenclature from the palladium hydrides [142]. β-NiH_x has a fcc lattice structure with the H atoms in the octahedral sites and $x = 0.6 \pm 0.1$ [143]. The β phase lattice parameter is ~6 % greater than that of Ni metal [143, 144]. The lattice parameter of α-NiH_x is only slightly expanded relative to Ni metal (less than ~1 %), supporting the general belief that it is isostructural with α-PdH_x [145, 146]. The H atoms in α-PdH_x occupy the octahedral interstitial sites and $x \leq 0.03$ [142, 145]. The full dimensional and energetic sequence of nickel hydrides has been discussed previously [133].

The XRD pattern of a freshly polished electrode shows the expected fcc Ni (111) and (200) peaks (Figure 4.8a).The diffraction peaks appear as doublets because the incident X-ray is split by spin-orbit coupling into $K\alpha_1$ ($2p_{3/2} \rightarrow 1s$) and $K\alpha_2$ ($2p_{1/2} \rightarrow 1s$) components. The weak (220) peaks at 76.32° and 76.54° were also observed. The diffraction peaks shown in Figure 4.8 were fit using the Lorentzian curve shape and the parameters listed in Table 4.2.

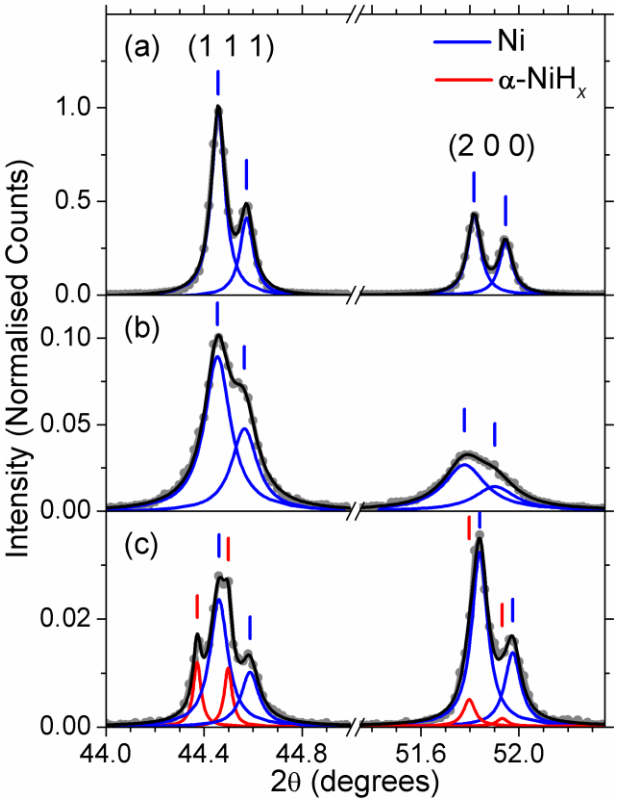

Figure 4.8 XRD patterns (●) of (a) chemically polished Ni foil and Ni electrodes treated galvanostatically at -0.5 A cm^{-2} for (b) 141 h (5.9 days) in 1 M NaOH and (c) 66.5 h (2.8 days) in 30 % (w/w) KOH. The y-scale is normalised to the most intense peak in (a). Measurements were performed *ex situ* in an air-tight sample holder that was purged with Ar. The fitted Lorentzian peaks and the cumulative line shapes are shown as solid lines. The curve parameters are listed in Table 4.2.

Table 4.2 Lorentzian parameters used to fit the XRD peaks shown in Figure 4.8 and the derived lattice spacing and unit cell parameters. Pairs of peaks arising from the split Cu $K\alpha_1$ and $K\alpha_2$ X-ray lines were fit with the same full-width half maximum (FWHM) value.

Sample	**Peak Centre** 2θ (degrees)	**FWHM** (degrees)	**Area**	**R^2**	**(h k l)**	**d (Å)**	**a (Å)**
(a)	44.458	0.067	1575.04	0.9958	(1 1 1)	2.036	3.527
	44.574		667.73				
	51.817	0.064	648.78	0.9949	(2 0 0)	1.763	3.526
	51.946		427.04				
(b)	44.455	0.127	269.79	0.9978	(1 1 1)	2.036	3.527
	44.565		144.66				
	51.778	0.204	127.91	0.9970	(2 0 0)	1.764	3.529
	51.902		67.30				
(c)	44.372	0.039	10.84	0.9965	(1 1 1)	2.040	3.533
	44.499		9.84				
	44.461	0.088	48.76		(1 1 1)	2.036	3.526
	44.588		20.85				
	51.797	0.057	6.70	0.9920	(2 0 0)	1.764	3.527
	51.932		1.96				
	51.840	0.079	59.69		(2 0 0)	1.762	3.524
	51.975		25.29				

Ni was cathodically charged by applying -0.5 A cm^{-2}. I chose this large geometric current density to accelerate the electrode deactivation. Ni that was charged in 1 M NaOH produces much weaker and broader diffraction lines than observed for the untreated sample (Figure 4.8b, Table 4.2). The (200) peak positions are shifted slightly, relative to Ni, whereas the (111) peaks are not. XRD peak widths generally originate from the combined effects of the detector resolution, crystallite size and non-uniform lattice strain. I disregard the first factor because the samples were analyzed using the same diffractometer. The latter two effects can be differentiated by the Williamson-Hall analysis method, however, at least three strong diffraction peaks are needed to properly conduct this analysis [191]. Nevertheless, Figure 4.8b qualitatively shows that a structural change in the Ni metal occurs during cathodic charging, which supports that H is incorporated into the material. I expect that H atoms move most rapidly into the electrode along grain boundaries and dislocation defects, where the diffusivity is the greatest, *i.e.*, by short-circuit diffusion, and more slowly by diffusion into the lattice [192]. This is consistent with the results of Soares *et al.*, who found that the electrode deactivation occurs more gradually for electrodes that have been annealed [18]. That is, the annealing decreases the number of defects and grain boundaries, which decreases the H atom diffusivity/mobility. The origin of the (2 0 0) peak shift is unknown. The samples were not perfectly flat, thus, the relative peak intensities between samples are not quantitative.

Ni charged cathodically in 30 % (w/w) KOH shows an additional pair of (111) peaks, which correspond to ~0.2 % lattice parameter expansion relative to metallic Ni (Figure 4.8c, Table 4.2). Because two pairs of peaks are observed, rather than a broadened, shifted pair of peaks, I know that there are two distinct crystallographic phases present. Hence, I propose that the H concentration near the grain edges builds up and, when the H concentration exceeds some

critical value, metallic Ni transforms to α-NiH_x. The formation of nickel hydrides has previously been observed to act as a barrier to further H diffusion [17]. Thus, the grain centres remain metallic Ni and the Ni diffraction peaks are sharper than for Ni charged in milder conditions. These results suggest that the rate of H absorption into Ni electrodes increases with solution alkalinity.

Soares *et al*. have provided the only other direct evidence of electrochemically formed bulk NiH_x in alkaline media without the addition of agents, such as thiourea [$SC(NH_2)_2$] and arsenic trioxide (As_2O_3), that are known to promote hydride formation [18, 133]. Electrodeposited Ni was cathodically charged (-0.3 A cm^{-2}) for 2 h in 30 % (w/w) KOH and weak β-NiH_x (1 1 1) and (2 0 0) XRD peaks were measured [18]. My attempts to emulate these results only yielded Ni and α-NiH_x diffraction peaks (Figure 4.8c). However, I now believe that my results differed because the electrode thicknesses were different. I utilized thicker electrodes (~127 μm thick) in my experiments and the diffusion of H deep into the material prevented the H concentration at the surface from increasing sufficiently to form the β-NiH_x phase. Soares *et al.* used very thin Ni electrodes (~15 μm thick) and, hence, the H content of the metal accumulated and concentrations along the grain boundaries increased rapidly during charging. Thus, the surface H concentrations increased sufficiently that β-NiH_x formed at the surfaces of their electrodes. I now conclude that the results of Soares *et al.* are indeed consistent with my own and it is reasonable to assume that the α-NiH_x phase also formed at their electrode surfaces, as a precursor to the β-NiH_x phase. However, since only the bases of the Ni peaks are visible in their reported XRD patterns and since their detector resolution was lower than mine, one cannot determine whether any α-NiH_x remained at the surface or whether it was completely consumed during the formation of the β-NiH_x phase [18].

The incorporation of H into Ni electrodes may explain the observed decrease in HER activity after several hours of electrolysis. The HER activity on freshly polished metallic Ni electrodes is quite high (Figure 4.1). With time, the H content of the electrode increases, which causes structural disorder, similar to what I observed in my XRD patterns (Figure 4.8b). This disorder may cause the decreased intercept observed in Figure 4.1 after 2 – 4 h of H_2 evolution. The change of the slope below -0.4 V_{RHE} after 2 – 4 h of H_2 evolution indicates that there is a change in the rate-determining step, either because the HER is a multi-step reaction or because the reaction pathway changes. For example, the slope may be related to the concentration of H at the electrode surface, which depends on the potential-dependent rate of H incorporation and on the diffusion of H in the material. In this interpretation, the region $\eta < -0.4$ V_{RHE} corresponds to greater H content at the surface, which could affect the kinetic parameters by an increase in structural disorder or by a phase transformation at the surface. For longer charge times, *e.g.*, 12 – 24 h, more H is expected to have accumulated and hence, the slope and intercept that corresponds to greater H content are observed across the entire potential range. This hypothesis is consistent with my findings, although it is only one possible explanation. More detailed studies are needed to clarify the cause of the observed changes of the slope and intercept. Nevertheless, the results in this work support that H incorporates into Ni electrodes during the HER and that the resultant structural effects at the surface, *i.e.*, increased disorder and phase transformations, negatively affect the kinetics of the HER.

I conclude from the voltammetric and XRD evidence that during the HER in alkaline media, H diffuses into metallic Ni electrodes. This introduces structural changes and can lead to the formation of α-NiH_x and β-NiH_x phases. Even though the latter has only been observed on a very thin electrode in concentrated KOH, it is reasonable to believe that this phase could form in

industrial electrolysers, which use concentrated KOH, apply very large current densities and typically operate for over 10 years. The incorporation of H into Ni electrodes can adversely affect the kinetics of the HER in alkaline media. Above the RHE potential, incorporated H oxidizes as it diffuses to the electrode surface. However, other, concurrent processes can make experimental results difficult to interpret.

4.3.2. Nickel Oxide and Nickel Hydroxides

Industrial electrolysers are often subject to transient current reversal, especially during initiation and shut-down. Thus, I considered the anodic processes on Ni and the effect they may have on a catalyst's HER activity. Anodic currents from the oxidative removal of incorporated H, discussed in section *3.1*, have often been attributed to oxide and hydroxide formation. Further, recent studies offer new insight on the phases of $Ni(OH)_2$ and can be used to re-interpret older reports. This section considers the Ni(II) species that form on metallic Ni electrodes in alkaline media and clarifies the voltammetric assignments (Figure 4.3, Table 4.3).

Table 4.3 The proposed electrode processes corresponding to the numerical regions indicated in Figure 4.3.

Region	Electrode Process(es)
(1)	H incorporated in the Ni metal oxidizes and dissolves into solution
(2)	Metallic Ni oxidizes to NiO_x and α-$Ni(OH)_2$
	H incorporated in the Ni metal oxidizes and dissolves into solution
(3)	H incorporated in the electrode material oxidizes and dissolves
	The NiO_x/α-$Ni(OH)_2$ layer is chemically modified and thickens
(4)	The NiO_x/α-$Ni(OH)_2$ layer thickens
	β-$Ni(OH)_2$ forms electrochemically and/or by aging of α-$Ni(OH)_2$
	H incorporated in the Ni metal oxidizes and dissolves into solution
(5)	α/β-$Ni(OH)_2$ oxidize to β-NiOOH
	The underlying NiO_x layer thickens
	H_2O/OH^- adsorbs and oxidizes to adsorbed oxygen species
(6)	H_2O/OH^- is oxidized to O_2 (OER)
(7)	The Ni(3) oxyhydroxide layer reduces to β-$Ni(OH)_2$
	Adsorbed oxygen species reduce and desorb
(8)	β-$Ni(OH)_2$, NiO_x and α-$Ni(OH)_2$ reduce to Ni[a]
	H_2O is reduced to H_2 (HER)
(9)	NiO_x and α-$Ni(OH)_2$ reduces to Ni[a, b]

[a]The surface layer on Ni may not fully reduce due to small amount of unreactive surface oxide-hydroxide, as discussed in section *3.2*.

[b]At more positive upper limits, the surface layer is chemically modified to contain β-$Ni(OH)_2$ and it reduces at more negative overpotentials, within region (8).

It is known that an air-formed oxide, 6 – 8 Å thick, rapidly forms on Ni metal that has been mechanically or electro-polished [44]. The details of this surface layer and the passive layers that form on Ni electrodes immersed in various electrolytes have been studied extensively, although there is no consensus on their compositions [42, 46, 193, 194]. MacDougall and Cohen observed reflection high energy electron diffraction (RHEED) peaks on electropolished Ni from non-stoichiometric NiO_x, $x \geq 1$, with ~2 % lattice parameter expansion [44]. I observed a weak Raman peak from NiO (or NiO_x) on chemically polished Ni (section 2.3.3 and Ref. [87]). Raman spectroscopy cannot usually detect very thin surface layers; however, this particular peak arises from a magnetic transition and is very sharp and intense [160]. The XPS spectra of mechanically polished Ni indicate that there is a NiO component (Figure 4.9a-i, b), which I assume is indistinguishable from NiO_x by this method. The XPS spectra also reveal a $Ni(OH)_2$ component that was not observed by RHEED or Raman spectroscopy [44, 87]. Using the XPS line shape for a β-$Ni(OH)_2$ component, the fitted curve does not exactly match the data at 858 – 859 eV (Figure 4.9a-i), similar to what is reported for α-$Ni(OH)_2$ deposits (section 2.3.2 and Ref. [87]). The α phase typically adopts a high degree of structural disorder, hence it may not be possible to detect very thin α-$Ni(OH)_2$ films by RHEED or by Raman spectroscopy. Medway *et al.* observed X-ray scattering evidence consistent with a layered surface structure in the sequence Ni|NiO|$Ni(OH)_2$ [41]. Since β-$Ni(OH)_2$ has sharper diffraction features than α-$Ni(OH)_2$, the absence of any β phase RHEED peaks indicates that it is not present in the air-formed film [44]. Therefore, from the combined results of XPS, RHEED, Raman spectroscopy and X-ray scattering, I conclude that the air-formed oxide on mechanically polished Ni surfaces is a bilayer composed of α-$Ni(OH)_2$ underlaid by non-stoichiometric NiO_x.

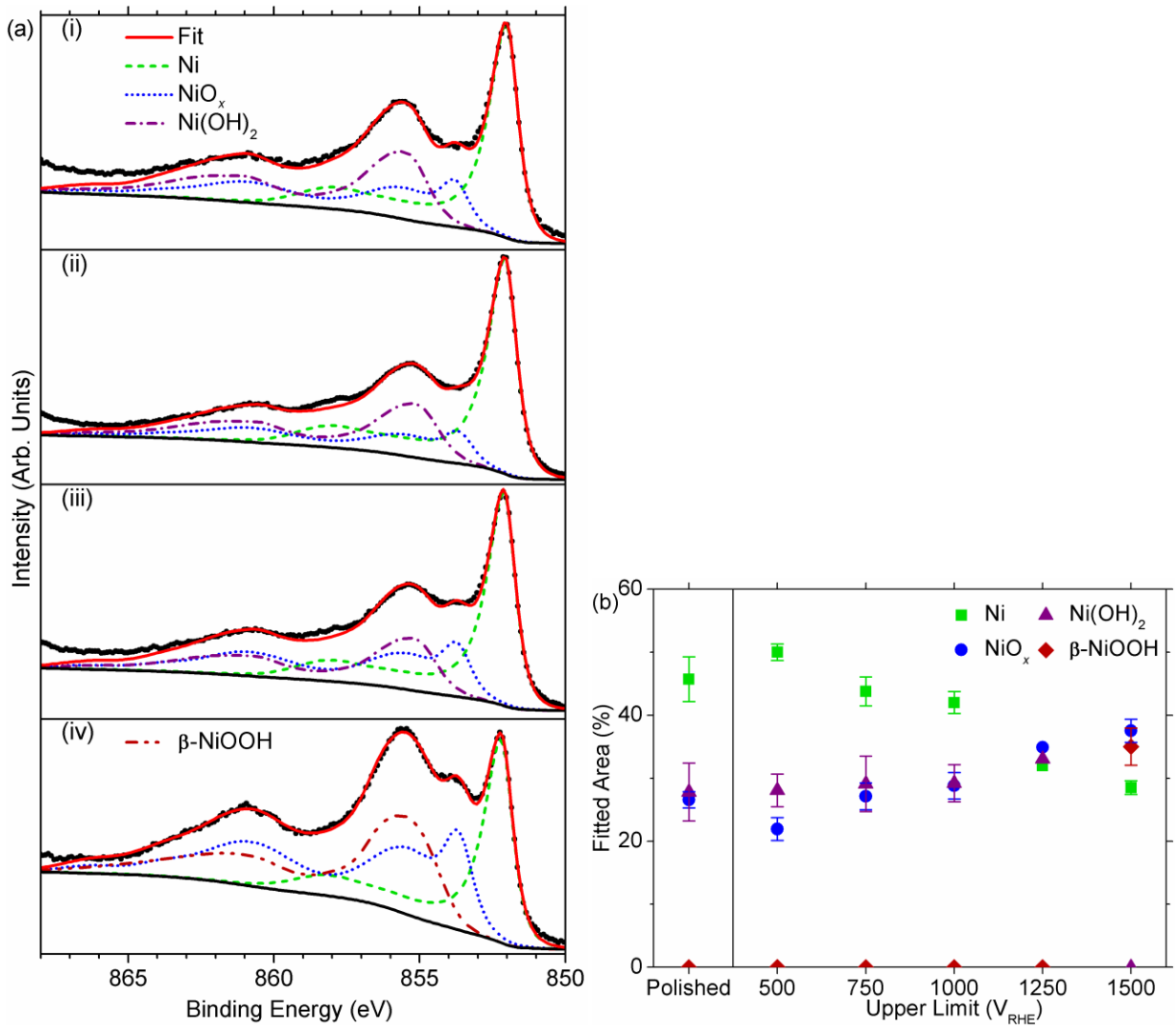

Figure 4.9 (a) Ni $2p_{3/2}$ X-ray photoelectron spectra (●) for (i) mechanically polished Ni and Ni electrodes held at -300 mV_{RHE} for 60 s in Ar-purged 0.1 M KOH then scanned at 100 mV s^{-1} to (ii) 0.5 V_{RHE}, (iii) 1.0 V_{RHE} or (iv) 1.5 V_{RHE}. Spectra were curve-fitted with Ni (- - -), NiO (• • •), β-$Ni(OH)_2$ (– • –) and β-NiOOH (– • • –) components using the line shapes and method of Biesinger *et al* [159]. (b) The surface oxidation state from the curve-fitted component area percentages of Ni (■), NiO_x (●), $Ni(OH)_2$ (▲) and β-NiOOH (♦). Each sample was analyzed at three spots. The data points show the average values and the error bars each span one standard deviation.

I measured the open circuit potential (E_{OC}) of mechanically polished Ni in argon-purged, alkaline solutions at about 0.4 – 0.5 V_{RHE}, which is consistent with previous reports [177]. The reversible potential of the α-$Ni(OH)_2$ surface component is not known exactly, however, it is greater than 0.108 V_{RHE} (see section 4.3.1). The non-stoichiometric NiO_x surface layer likely contains Ni^{2+} vacancies, similar to passive NiO_x layers [194], which would create a fractional Ni(III) character and, hence, may increase the E_{OC} above that of ideal NiO (0.132 V_{RHE}).

On the first reverse potential scan after electrode immersion, a cathodic peak nearly identical to peak (9) is observed and it has been shown that the electrode mass decreases [195]. Ellipsometry measurements during this first reverse scan show that the surface layer is mostly removed at about -300 mV_{RHE}, although, a small surface layer remains [178]. There is no evidence supporting the possibility of a true metal-solution interface in alkaline solution, however, the existence of a small amount of unreactive nickel oxide-hydroxide does not change myinterpretation of the voltammetric features. It may, however, affect the scan-rate dependences of some processes and the catalytic activity for the HER on Ni.

On the basis of reversible potentials (Table 4.1), it has been suggested that the voltammetric peaks (2) and (9) correspond to the formation and reduction, respectively, of a Ni(II) species [13, 37, 175, 176, 181], while other studies specify that the oxidation product is α-$Ni(OH)_2$ [149, 174, 178, 185]. There are three possible oxidation products – NiO_x, α-$Ni(OH)_2$ and β-$Ni(OH)_2$ – and rationalizing electrochemical data is further complicated by the range of possible disordered structures that $Ni(OH)_2$ electrode materials can adopt [87]. The partial reduction of the air-formed oxide must occur before the anodic peak (2) can be observed [177, 185]. Aging the polished electrodes in alkaline electrolyte prior to voltammetry experiments decreases the charge under the anodic peak (2) [177]. X-ray scattering shows that the surface

layer thickens, relative to the air-formed film, upon immersion in alkaline solution [41]. Further, it is well-established that α-$Ni(OH)_2$ gradually transforms to β-$Ni(OH)_2$ in alkaline media. The β phase is generally more crystalline and is more stable in alkaline media than the α phase [87], so it may be reasonable to assume that the β phase reduces at more negative potentials than α-$Ni(OH)_2$, although this cannot be stated with certainty unless the thermodynamic and kinetic parameters are known. Thus, more negative overpotentials or longer treatment times are required to remove the air-formed layer after it has been aged in alkaline solution because the layer is more stable and/or the surface layer has thickened. Since the surface layer must be removed for peak (2) to occur, fractional reduction of the surface layer would subsequently result in a fractional anodic current density at (2).

Ellipsometry measurements performed during a forward voltammetric sweep in 0.1 M KOH show that an oxide and/or hydroxide film forms at peak (2) [42]. Ultraviolet/visible (UV/vis) range reflectance measurements performed *in situ* during a forward voltammetric sweep in 0.1 M NaOH show that new reflectance peaks develop at anodic peak (2) [196]. Gravimetric measurements show the electrode mass increases in region (2), although the mass of the oxidation product is obscured by the concurrent removal of H from the Ni metal [187, 195]. These results show that a Ni(II) surface layer forms at peak (2).

The UV/vis reflectance data collected during forward potential sweeps in region (2) have been used to create a reference spectrum for α-$Ni(OH)_2$ [196]. However, the reported reflectance features are very broad and there are no reports of the typical reflectance spectra for the possible surface layers, *i.e.*, NiO_x, α-$Ni(OH)_2$ and β-$Ni(OH)_2$ materials. Further, the possible effects of structural disorder on the reflectivity spectra are unknown. Thus, there is insufficient evidence to conclusively determine the composition of the surface layer at the voltammetric region (2). As

such, I used the results of the spectroscopic investigation of $Ni(OH)_2$ materials in the previous chapter (and Ref. [87]) to re-examine the *in situ* surface-enhanced Raman spectroscopy (SERS) results reported by Melendres and Pankuch [46]. The authors collected SERS spectra on Ni electrodes in 0.1 M NaOH during 1 h potentiostatic treatments at various potentials. I note that it is possible that some α-$Ni(OH)_2$ may have chemically transformed to β-$Ni(OH)_2$ during the 1 h treatment periods. Also, the O-H stretching modes of H_2O are convoluted with their data over the frequency range 3000 – 3700 cm^{-1}. Further, the surface selection rules for SERS are difficult to predict and are often quite different than for conventional Raman spectroscopy. With these caveats in mind, the reported spectrum for an electrode held at region (2) contains weak Raman peaks at ~450 cm^{-1} and ~800 cm^{-1}, which I here ascribe to a lattice mode and a 2nd order lattice mode of α-$Ni(OH)_2$. There is a very weak feature at ~510 cm^{-1} that I ascribe to NiO_x. I make the assumption that the non-stoichiometric material has the same vibrational modes as a stoichiometric NiO sample [46]. Melendres and Pankuch report a broad feature at ~3630 cm^{-1}, which I now attribute to the O–H stretching modes of α-$Ni(OH)_2$. It is known that the two phases of $Ni(OH)_2$ are most easily differentiated by the O–H stretching region and that β-$Ni(OH)_2$ has stronger vibrational features than α-$Ni(OH)_2$ [87]. Hence, the β phase is either absent or, at most, present as a very minor component of the surface film in this region. Thus, from my re-examination of the SERS results of Melendres and Pankuch I conclude that the surface layer formed at region (2) contains α-$Ni(OH)_2$ and NiO_x components. As such, the UV/vis spectrum reported by Hahn *et al.* is not a true reference spectrum for α-$Ni(OH)_2$ and the biphasic nature of the film explains the breadth of their reported reflectance features [196].

I observe that the anodic maximum of peak (2) is proportional to the scan rate raised to the exponent 0.76 (Figure 4.6). To simplify the problem, one can attribute the current in region

(3) entirely to H oxidation. If the average anodic current in region (3) is subtracted from region (2) the exponent of the scan-rate dependence of peak (2) is ~0.5, *i.e.*, the square root of the scan rate. This suggests that the surface oxidation is limited by the linear diffusion of either OH^-/O^{2-} anions into the surface layer or Ni^{2+} cations out to the electrode-solution interface.

It has been suggested that the hydroxide film thickens and transforms to β-$Ni(OH)_2$ in the potential regions (3) and (4) [149, 174, 178]. The intensities of XPS (Figure 4.9b), ellipsometric and UV/vis features support that during a forward potential sweep the surface layer indeed thickens in regions (3) and (4) at an approximately constant rate [42, 46, 196]. I again re-examine the SERS spectra collected during voltammetry by Melendres and Pankuch [46]. The absence of any sharp SERS features in the O–H stretching region [46] indicates that there is very little, if any, β-$Ni(OH)_2$ present at the surface in voltammetric region (3). I here assign the reported SERS peaks to α-$Ni(OH)_2$ (456 cm^{-1}, ~800 cm^{-1} and ~3630 cm^{-1}) and NiO_x (512 cm^{-1}). In the SERS spectrum collected on an electrode that was held in potential region (4), sharp peaks are visible at ~3580 cm^{-1} and ~3635 cm^{-1} [46]. I now conclude that these peaks correspond to the β-$Ni(OH)_2$ A_{1g} and A_{2u} modes, respectively. The A_{2u} mode is not normally active in Raman spectroscopy [87]. However, the surface selection rules can cause 'IR-active' modes to appear in SERS spectra. The presence of a large fluorescent background in the reported SERS spectrum [46], which is characteristic of the Raman spectra of β-$Ni(OH)_2$ films [87], supports this assignment. There is also a broad underlying feature at ~3635 cm^{-1}, which I attribute to an α-$Ni(OH)_2$ component. The β phase typically has more intense Raman signals than α-$Ni(OH)_2$ [87], hence, the β-$Ni(OH)_2$ peak at 3635 cm^{-1} likely only represents a minor component. The 2nd order peak at ~800 cm^{-1} is weaker in region (4), which indicates that the surface layer becomes more ordered. The transformation of α-$Ni(OH)_2$ to β-$Ni(OH)_2$ may not be observable from the lattice

modes, since the surface selection rules are unknown and both materials have vibrational modes at ~450 cm^{-1}. The voltammetric properties of the subsequent peaks (5) and (7) are consistent with a surface layer that contains both α and β-$Ni(OH)_2$ components by the end of region (4). Structural disorder and an underlying NiO_x film are expected to influence the optical properties of the surface layer and, thus, ellipsometry was unable to confirm the surface species [42]. During a forward potential sweep in regions (3) and (4), the electrode mass is unchanged because incorporated H is removed while the film thickens [187, 195].

The voltammetric behaviour after the first cycle depends on the upper and lower limits. For more positive limits, the film requires more negative potentials to reduce. This is attributed to a more stable surface layer with greater crystallinity and higher β-$Ni(OH)_2$ content. For insufficiently negative lower limits, only small cathodic currents are observed (Figure 4.7). During the reverse scan H is incorporated in to the electrode and the mass increases slightly. During the forward scan the electrode mass decreases slightly as the incorporated H is removed [195].

In summary, from voltammetric, XPS and literature evidence, I find that polished Ni electrodes have a thin, air-formed bilayer of NiO_x and α-$Ni(OH)_2$. This surface layer can be mostly removed cathodically at peak (9), although aging in basic solution makes this layer more difficult to remove. Anodic peak (2) corresponds to the formation of α-$Ni(OH)_2$ and NiO_x. The anodic charge under this peak has been used to estimate surface roughness [131, 149]. However, I recommend that this should only be used for an approximate value because of the complex factors that affect this region and the poorly defined unit cell parameters of α-$Ni(OH)_2$ [34, 35]. The surface film thickens in regions (3) and (4). In region (4), some β-$Ni(OH)_2$ is formed, either electrochemically or by the chemical aging of the α-$Ni(OH)_2$ component.

4.3.3. Nickel Oxyhydroxides

The anodic peak (5) is attributed to the formation of β-NiOOH, which I observe by XPS analysis (Figure 4.9a-iv). This phase cannot be measured *ex situ* because it decomposes in ambient conditions. Rather, the decomposition product, $Ni_3(OH)_4O_2$, was characterized as per Biesinger *et al.* and Grosvenor *et al* [159, 197]. Thus, one cannot conclude from XPS results alone that the anodic peak (5) corresponds to the formation of β-NiOOH, rather than $Ni_3(OH)_4O_2$. The local maxima in Figure 4.9a-iv (855.5 eV and 860.9 eV) are slightly higher than I observe for $Ni(OH)_2$ samples (855.3 eV and 860.7 eV). Further, the voltammetric features match those reported by Visscher and Barendrecht, who observed the formation of β-NiOOH by *in situ* ellipsometry [42]. A β-$Ni(OH)_2$ component was not used while fitting these spectra because any Ni(II) is expected to have mostly oxidized. Further, it is difficult to deconvolute β-$Ni(OH)_2$ and β-NiOOH components in XPS spectra. The presence of a NiO_x component is consistent with a previously reported underlying layer that thickens at more positive potentials, well into the OER region [41].

I observe that the anodic maximum of peak (5), background-corrected using region (4), is proportional to the scan rate raised to the exponent of ~0.6 (Figure 4.6b), which could indicate that the reaction is diffusion-limited. Indeed, the oxidation of β-$Ni(OH)_2$ is largely agreed to be limited by the movement of H^+ through the material to the electrode-solution interface [77], which would yield an exponent of 0.5. Conversely, the mechanism for α-$Ni(OH)_2$ oxidation is unknown.

The conversion of $Ni(OH)_2$ electrode materials to NiOOH is used extensively for the anodes of secondary alkaline batteries, including NiCd and NiMH [82]. At sufficiently positive potentials, β-NiOOH overcharges and forms γ-NiOOH, which contains alkali cations and is often

described to fractionally contain Ni(IV) [35]. This latter phase is not expected at the upper scan limits used in this work and is not observed in my XPS spectra.

On potential scan reversal, I observe two cathodic peaks in region (7) from the removal of adsorbed O species and the reduction of β-NiOOH to β-$Ni(OH)_2$ [35, 42]. Reduction of β-NiOOH yields only β-$Ni(OH)_2$ and the shapes of the reduction peaks in region (7) do not change on cycling (Figure 4.10) [42]. However, the oxidation peak (5) is sharper after the first cycle. Thus, the broad voltammetric peak during the first cycle corresponds to the oxidation of α-$Ni(OH)_2$, whereas the sharp peak during subsequent scans is from the oxidation of β-$Ni(OH)_2$. The charge associated with peaks (5) and (7) increase with cycling, presumably because the repeated lattice contraction and expansion from oxidation and reduction exposes more of the underlying metal.

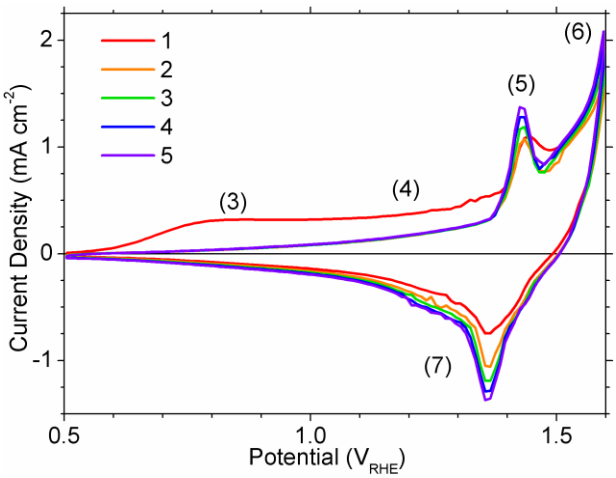

Figure 4.10 A freshly polished Ni electrode was held at 500 mV_{RHE} for 60 s then cycled at 100 mV s^{-1} in Ar-purged 0.1 M KOH. The cycle numbers are indicated on the figure.

During the reverse potential scan, there is a small anodic current density between ~0.3 to ~0.7 V_{RHE} from the oxidation of incorporated H. The magnitude of this current is considerably less than for electrodes that are not cycled through the Ni(II)/Ni(III) redox region (*e.g.* Figure 4.4 vs. Figure 4.5), which demonstrates that the H diffusivity of the compact, crystalline β-$Ni(OH)_2$ layer is much lower than it is for a disordered α-$Ni(OH)_2$ surface layer.

4.4. Conclusions

Table 4.3 summarizes the electrode processes in the potential regions indicated in Figure 4.3. The complexity of the voltammetry of metallic Ni in basic media results from the oxidation of H_2O/OH^-, Ni, NiH_{abs}, NiO_x and α/β-$Ni(OH)_2$ species during the forward scan and the reduction of H_2O/OH^-, β-NiOOH, α/β-$Ni(OH)_2$ and NiO_x during the reverse scan. Many of these processes occur concurrently and depend on the electrode history. The transformation of α-$Ni(OH)_2$ to β-$Ni(OH)_2$ and the various types and degrees of structural disorder further increase the complexity of this electrochemical system.

The decrease in HER activity on metallic Ni cathodes with time appears to be attributable to the incorporation of H into electrode material. During prolonged cathodic polarization in alkaline electrolyte solutions, α-NiH_x and β-NiH_x may form at the electrode surface. The addition of hydridic H into the electrode alters the electronic structure near the electrode/solution interface and adversely affects the HER activity. Reported voltammetric evidence at 77 °C is consistent with H incorporation [198], although, further investigation is needed to determine whether α- or β-NiH_x can form at the temperatures typically used for industrial electrolysis (*i.e.* 50 – 80 °C [5]).

Transient anodic currents can occur at the cathode in industrial electrolysers during initiation and shut-down, thus, I have assessed the oxidation processes on smooth Ni and their potential impact on the cathode's performance. The oxidation products have negligible solubility in alkaline media and, from the recovery of peak (2) after cathodic treatment, they are observed to reduce back to the initial state at about -300 mV_{RHE} (Figure 4.7). However, lattice expansion and contraction occurs on cycling, which creates mechanical stress and roughens smooth Ni electrodes. This may increase the electrochemical surface area, which would actually improve an electrode's performance. However, the mechanical strain may damage or destroy high surface area materials. Although there is no lasting chemical change from transient anodic currents, cathodes must be able to endure repeated expansion and contraction at the surface.

Voltammetry on metallic Ni electrodes in alkaline solution is very difficult to reproduce to a satisfactory degree of precision, even if solutions are replaced and electrodes are polished between each experiment. Such difficulties dealing with Ni in alkaline media have been stressed previously [151]. I now understand that the accumulation of H, relatively deep within the electrode, causes experimental drift. Hence, strict adherence to random experimental order is very important to avoid systematic errors and electrodes should be regularly cut or polished with a coarse abrasive to remove as much of the affected surface material as possible. Finally, electrodes may require periodic replacement to collect sufficiently high quality data for fundamental studies.

5. Surface Area Measurements on Nickel Electrodes

The contents of this chapter were adapted from the following peer-reviewed article [199]:

Hall, D.S., Bock, C. & MacDougall, B.R. An Oxalate Method for Measuring the Surface Area of Nickel Electrodes. *J. Electrochem. Soc.* **161**, H787-H795 (doi:10.1149/2.0711412jes).

5.1. Introduction

In general, the measured activity of an electro-catalyst is directly proportional to the electrochemical surface area (A_{ECSA}), the interfacial surface area that is available for a pure Faradaic reaction that is activation-controlled. Therefore, it is desirable to have an objective method to compare electro-catalysts such that surface roughness effects may be examined separately from chemical considerations (reaction mechanisms and transition energies). The simplest approach is to first measure the A_{ECSA} values of different catalysts and then divide this by their geometric areas to find the surface roughness [147]. Since the electrode activities are directly proportional to A_{ECSA}, the catalytic properties may be compared by dividing the measured activities by the A_{ECSA} values to obtain the real current densities (*e.g.*, Ni_xZn_y [19] and Ni_xMo_y [20, 21]). However, this first requires a method to accurately measure A_{ECSA}.

The purpose of the work in this chapter is to develop a new method to measure the surface area of nickel electrodes, *in situ*, with improved accuracy and precision. A novel approach is presented that utilizes the addition of solution oxalate and the measurement of a surface-limited process with highly unusual voltammetric characteristics.

5.2. Experimental Methods

5.2.1. Electrode Preparation

Voltammetric experiments utilized electrodes prepared from a metallic Ni rod (Alfa Aesar, ≥ 99 %, 3.2 mm diameter) embedded in epoxy resin so that only one flat, circular face was exposed to the electrolyte solution. Electrodes that were used for subsequent characterization by Fourier transform infrared (FT-IR) spectroscopy were prepared from metallic Ni foil (Alfa Aesar, 99.5 %, 0.787 mm thick) electrodes (1 cm × 2 cm). Electrodes were

mechanically polished using 320 grit SiC paper followed by 9 μm polycrystalline diamond, 3 μm polycrystalline diamond (Buehler MetaDi Supreme) and 0.05 μm Al_2O_3 (Buehler MasterPrep) suspensions, unless otherwise noted. Foil electrodes (for FT-IR) were partially covered with Teflon tape and the lower, exposed portion was fully immersed into the electrolyte solution during electrochemical measurements. Electrodes were rinsed and sonicated in high purity water (Millipore Milli-Q, 18.2 MΩ cm) prior to their use.

5.2.2. Electrolyte Solution Preparation

Electrolyte solutions were prepared immediately prior to electrochemical experiments (< 4 h) using KOH pellets (Fisher Scientific, ACS grade), oxalic acid dihydrate (Fisher Scientific, ACS grade), and high purity water.

5.2.3. Electrochemical Measurements

Electrochemical measurements were conducted in a standard three-compartment glass cell. The working compartment was air-tight and purged with Ar gas (grade 5.0) or with electrolytically generated H_2 gas (Parker Hannifin H2PEM-165L, 99.9999%). A Pt foil (≥ 3 cm^2) served as the counter electrode. A saturated calomel electrode (SCE) served as the reference electrode. This reference was chosen for its stable measurements and fast response, which was important for high scan-rate voltammetry experiments. For most experiments in this work, the sample chamber was purged with H_2 to allow regular measurements of the SCE potential against the reversible hydrogen electrode (RHE) to correct for junction potential effects and drift. Typical values from these potential measurements were used to estimate the SCE potential for

the experiments that utilised Ar as the purge gas. The RE was separated from the working compartment by a glass frit.

Voltammetric measurements were performed using a Princeton Applied Research 273a potentiostat controlled with CorrWare software (v. 3.3c, Scribner Associates, Inc.).

5.2.4. Attenuated Total Reflectance (ATR) Fourier Transform Infrared (FT-IR) Spectroscopy

The FT-IR measurements were performed at room temperature using a Bruker IF66/s spectrometer equipped with an ATR accessory and a deuterated triglycine sulfate (DTGS) detector. The optical chamber was purged with nitrogen to minimize the interference from water and carbon dioxide. Spectra were collected with OPUS software (v.5.0, Bruker Optik GmbH). Measurements were taken from several points on each sample and averaged.

5.3. Results and Discussion

The purpose of this work is to establish a new method to measure the A_{ECSA} of nickel electrodes with high accuracy and precision. The method presented involves the addition of an oxalate salt to an alkaline electrolyte solution and the formation of an adsorbed oxalate layer. However, the method presented in this work is significantly different from those reviewed by Trasatti and Petrii [147]. These literature methods involved measuring the Coulombic charge from the underpotential deposition (UPD) of a metal ad-layer [200-203] or from the electrochemical adsorption or desorption of an adsorbed surface layer [204-207]. In my method, the formation of an oxalate ad-layer is utilized to stabilize the surface nickel hydroxide and limit its growth to a single layer. The Faradaic oxidation and reduction of this stabilized $Ni(OH)_2$ and

NiOOH surface layer is measured and the corresponding Coulombic charge is then used to calculate A_{ECSA}.

In this chapter, first the choice of oxalate as the adsorbing species is rationalized. This is followed by general observations of the effect of solution oxalate on the alkaline electrochemistry of nickel. The validity of the experimental methods is then discussed. Voltammetric and spectroscopic evidence is presented to conclusively demonstrate that solution oxalate adsorbs onto the oxidized nickel hydroxide surface. Next, the effect of the voltammetric scan rate on the ad-layer formation is discussed with emphasis on the formation and measurement of a single layer. Finally, my method for measuring A_{ECSA} is presented with a discussion of the accuracy and precision of this new technique.

5.3.1. Solution Oxalate as a Candidate Molecule for Surface Adsorption

The oxalate anion ($C_2O_4^{2-}$) is a versatile chelating ligand that forms solid dihydrate chains with several divalent metals, including Mg, Mn, Fe, Ni, and Zn. For Ni(II), α-$NiC_2O_4 \cdot 2H_2O$ is the most common and stable polymorphic structure (Figure 5.1a, Table 5.1) [208]. In these metal complexes, the oxalate molecule adopts a planar (D_{2h}) configuration. However, the free anion in solution adopts a twisted conformation with a dihedral angle close to 90° (D_{2d}, Figure 5.1b). The energy difference between the two conformers is very small, ~17 – 25 kJ mol^{-1} [209, 210]. As a ligand, oxalate adopts a variety of twisted conformations (D_2) such that the O–O distance adjusts to best match the cationic size. That is, the oxalate anion is planar or near-planar when bonded to small cations, whereas it is twisted when bonded to larger cations [210]. In addition to being a versatile chelating agent, oxalate is known to adsorb on a wide variety of metal oxide, hydroxide and oxyhydroxide surfaces (see Section 3.5 for several examples). As with the solution

complexes, oxalate adjusts its dihedral angle, and therefore the O–O spacing, to match the size and spacing of the substrate (*e.g.*, ferrihydrite [211] and anatase [212]). This makes oxalate a very versatile adsorbate compound.

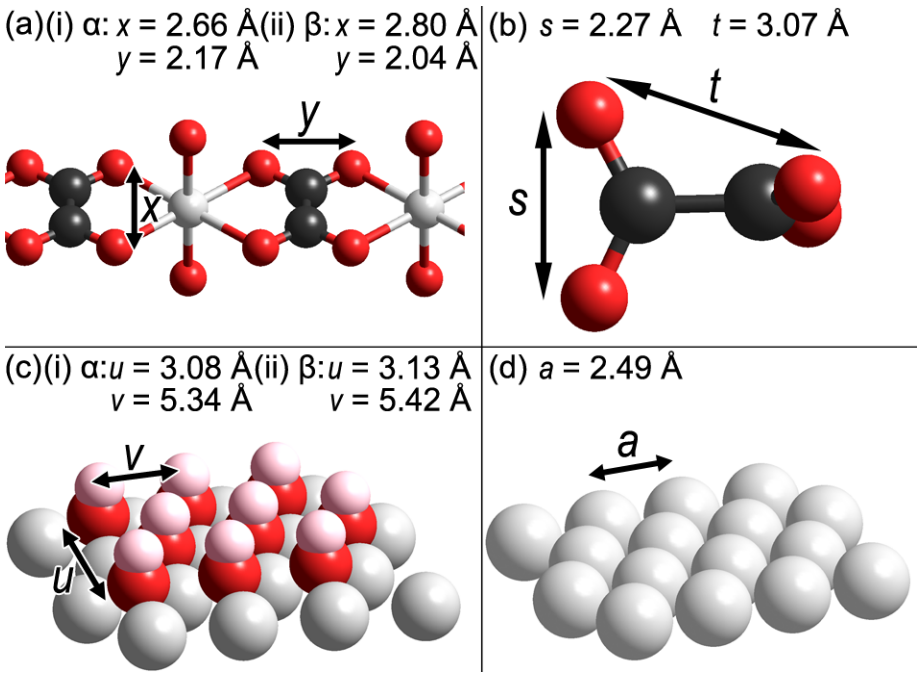

Figure 5.1 (a) A segment of a $NiC_2O_4 \cdot 2H_2O$ chain. The O–O distances are shown for the two polymorphs, (i) α and (ii) β (bond lengths and angles from Deyrieux et al. are summarized in Table 5.1)[208]. H atoms (axial H_2O) are not shown. (b) The most stable structure of the free oxalate anion in water, as calculated by Gao and Lui at the B3LYP/6-31+G** level [213]. The O–O distances are indicated. (c) The $Ni(OH)_2$ (001) surface. The O–O distances are shown for the two polymorphs, (i) α and (ii) β (atomic positions from Ref. [51] and [53]). H positions are not known for α-$Ni(OH)_2$. (d) The (111) surface of the fcc Ni metal. Legend: grey = Ni, red = O, black = C, pink = H.

Table 5.1 The bond lengths and bond angles for the two forms of $NiC_2O_4 \cdot 2H_2O$ reported by Deyrieux *et al* [208].

	α		**β**	
Bond Lengths (Å)				
$C_1 - C_2$	1.331	± 0.036	1.320	± 0.032
$C_1 - O_1$	1.271	± 0.034	1.260	± 0.028
$O_1 - O_2$	2.662	± 0.066	2.797	± 0.016
$O_1 - O_3$	2.165	± 0.041	2.042	± 0.011
$Ni - O_1$	2.069	± 0.026	2.164	± 0.014
$Ni - O(H_2O)$	2.025	± 0.020	2.049	± 0.012
Bond Angles				
$C_1 - C_2 - O_2$	121° 35'	± 2° 37'	[a]125° 52'	± 1° 28'
$O_1 - Ni - O_2$	80° 04'	± 1° 09'	80° 30'	± 0° 57'
$Ni - O_1 - C_1$	108° 23'	± 1° 51'	103° 53'	± 1° 00'

[a]Deyrieux *et al.* report this bond angle = 107° 16'. However, the sum of the bond angles in the five-membered ring (C – C – O – Ni – O) should be exactly 540°, whereas the sum from their values is only 502° 48'. From the bond lengths, this angle (*i.e.* the $C_1 - C_2 - O_2$ angle) was determined to be the incorrect parameter. The value in the chart is the corrected value that I calculated.

In alkaline media, nickel electrodes typically form a nickel hydroxide surface layer [40]. Therefore, the geometric match between oxalate and nickel hydroxide was then considered (Figure 5.1c). It was found that the O–O spacing in oxalate compounds and nickel hydroxides are similar (Table 5.2), especially when considering the variability of the O–O spacing in oxalate complexes. It is therefore possible that oxalate may adsorb onto a $Ni(OH)_2$ (001) surface by substituting surface hydroxide groups and forming five-membered rings. Thus, it was decided that oxalate is a good candidate species for adsorption onto nickel electrodes in alkaline media.

Table 5.2 The interatomic distances for nickel(II) oxalate, solution oxalate and nickel(II) hydroxide.

	Interatomic Distance (*Å*)				
	$NiC_2O_4 \cdot 2H_2O$		$C_2O_4^{2-}$	$Ni(OH)_2$	
	α[208]	**β**[208]	aq.[213]	**α**[53]	**β**[51]
$O_1 - O_2$	2.66	2.80	3.07	3.08	3.13
$O_1 - O_3$	2.17	2.04	2.27	5.34	5.42
Ni – O	2.07	2.16	N/A	2.05	2.12

5.3.2. General Effect of Solution Oxalate on the Alkaline Voltammetry of Nickel

Having established oxalate as a likely candidate for adsorption onto an oxidized nickel electrode, the effect of the addition of an oxalate salt to an alkaline electrolyte on the voltammetry of nickel was measured (Figure 5.2). It can be qualitatively assessed that the solution oxalate has only a minor effect on the forward scan up to about 1.35 V_{RHE}. The slight differences in the anodic current density in this potential range may be attributed to either the solution oxalate or simply to experimental errors. It is noted that the voltammetric behaviour in this potential region is greatly affected by very small differences in electrode pretreatment and history [40, 151]. Therefore, if the oxalate salt does affect the formation of a Ni(II) surface layer in this potential range, its role is presumably a subtle one, such as a distinct chemical process that occurs after the surface layer's electrochemical formation.

Above 1.35 V, the effect of solution oxalate on the voltammetry is marked. The anodic peak at 1.48 V, which corresponds to the oxidation of surface $Ni(OH)_2$ to NiOOH, is shifted to the more negative potentials by about 80 mV, its width is decreased, and the peak current density is more than quadrupled. Beyond this unusually sharp peak, there is a slightly increased current density, relative to the scan measured in the absence of solution oxalate, and the onset of the oxygen evolution reaction is observed. The increase may correspond to an asymmetric tail of the Ni(II)/Ni(III) oxidation peak or to slightly enhanced oxygen evolution in the presence of oxalate.

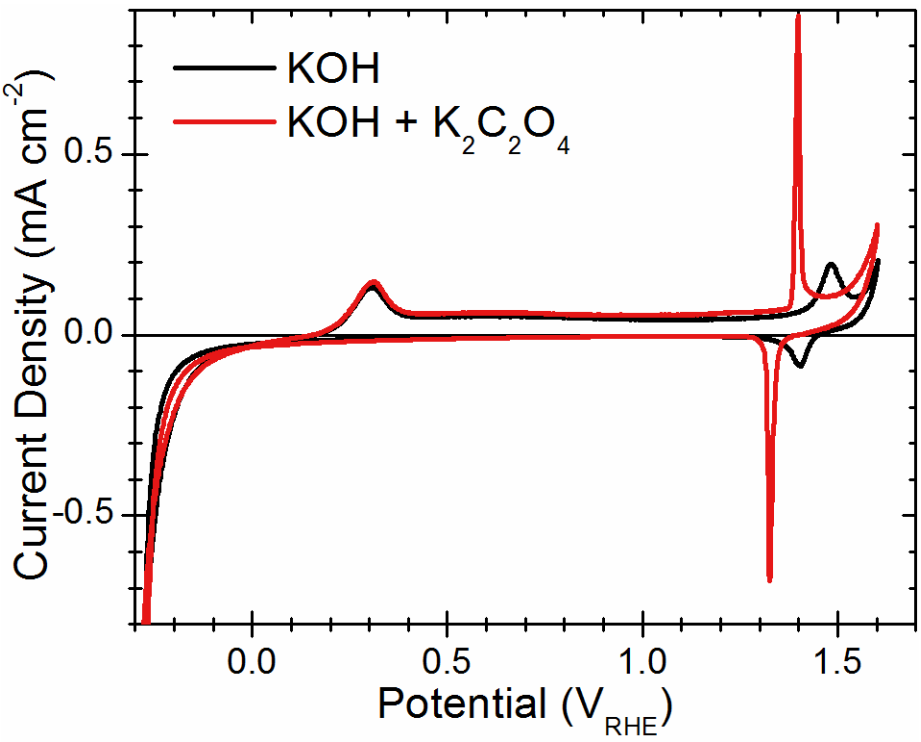

Figure 5.2Cyclic voltammetry was measured on a nickel electrode at 20 mV s^{-1}. The electrolyte solution contained either 0.10 M KOH or 0.10 M KOH and 0.08 M $K_2C_2O_4$. The solution was deaerated with H_2.

In the reverse potential scan, the NiOOH to $Ni(OH)_2$ reduction peak is likewise shifted to more negative potentials by about 80 mV in the presence of solution oxalate. Further, the peak width is greatly reduced, and the peak cathodic current density is increased by about a factor of seven. Continuing in the negative direction, there are no further clear effects of solution oxalate until the hydrogen evolution reaction onsets, near the RHE. Below this potential, there are several possible reactions, including the reduction of any surface oxide/hydroxide layers, the hydrogen evolution reaction, and absorption of hydrogen into the electrode [40]. The effect of solution oxalate on the voltammetry in this potential region is outside the scope of the present work, but it may involve these, and other, electrode processes.

5.3.3. Validity of the Voltammetric Measurements

It should be noted that the use of a saturated calomel reference electrode (SCE) in a chloride-free, alkaline electrolyte solution is generally a poor choice. However, when these experiments were initially measured with a mercuric oxide reference electrode (Hg/HgO) the response was too slow to accurately measure the sharp voltammetric peaks shown in Figure 5.2. This arises from the reference electrode's construction and impedance [214]. Thus, a trade-off was made and the SCE was employed, which provided considerably improved measurement rates. To minimize contamination, the reference was introduced immediately before measurements and the solution was changed frequently to prevent contamination with chloride anions. The use of the SCE also introduced an unknown junction potential, which was measured by de-aerating the solutions with hydrogen gas and measuring the potential of the reversible hydrogen electrode (RHE). This additionally accounted for the junction potential effect from the addition of the oxalate salt, which was typically ~10 mV. The junction potential effect from the

solution oxalate was similarly measured and was typically < 5 mV. In turn, it was then considered whether the introduction of hydrogen into the electrochemical system affected the electrochemistry of the system. This was qualitatively assessed by performing identical cyclic voltammetry measurements using either hydrogen or argon as the purge-gas. It is seen in Figure 5.3 that there are only slight differences between these two measurements. Note that slight potential shifts arise because the exact potential of the SCE reference was unknown in the solution deaerated with argon. Therefore, it is concluded that the characteristics of the anodic peak at 1.4 V in Figure 5.3 are attributable to the presence of solution oxalate, and are unaffected by the use of the SCE or hydrogen.

The effect of the solution oxalate concentration on the voltammetry is not shown, but as the concentration decreases below 0.08 mol L^{-1}, the position of the Ni(II)/Ni(III) peak shifts to more positive potentials and the width of the voltammetric peak increases. As the oxalate concentration approaches zero, the peak characteristics are similar to the oxalate-free condition. Therefore, the peak positions and widths shown in Figure 5.2 may be considered extreme cases. That is, these two peaks illustrate the high and low oxalate concentration limits. In concentrations exceeding 0.08 mol L^{-1}, there was no observed effect on the peak's position or width. Finally, it was observed that the most reproducible results were obtained by preparing the electrolyte solution immediately before, i.e., within a few hours of, voltammetric measurements.

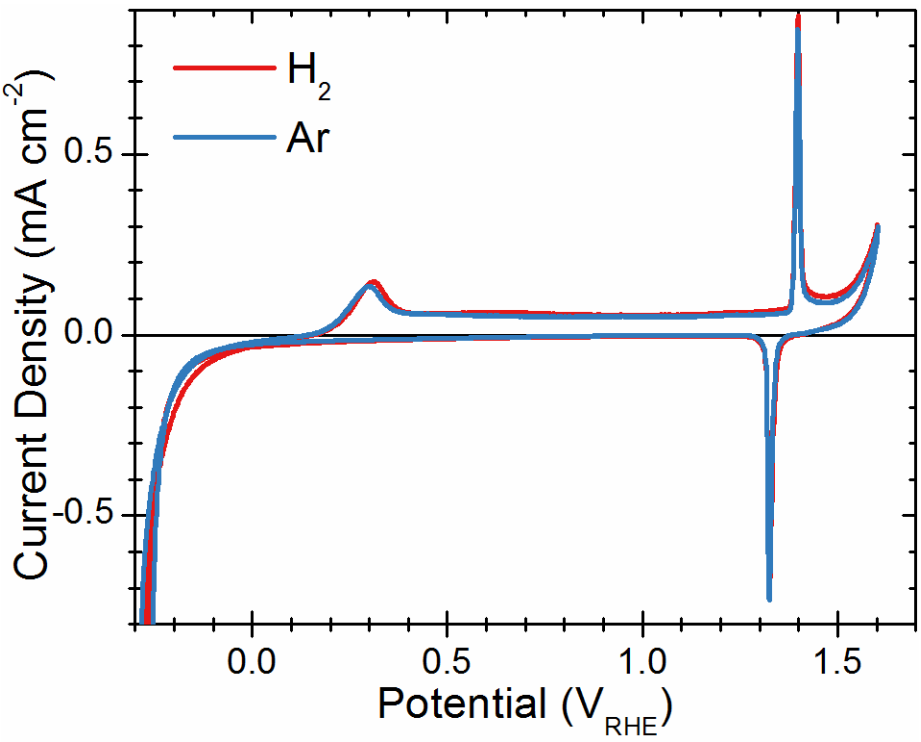

Figure 5.3 Cyclic voltammetry was measured on a nickel electrode at 20 mV s^{-1}. The electrolyte solution contained 0.10 M KOH and 0.08 M $K_2C_2O_4$ and was deaerated with either H_2 or Ar.

5.3.4. Voltammetric Evidence of the Adsorption of Oxalate

The effect of the addition of several organic compounds to alkaline electrolytes on the voltammetry of nickel has been studied previously. Test compounds have included various alcohols, amines and carboxylate species. For the most part, the presence of these species does not significantly affect the voltammetry below the formation of a surface NiOOH layer, at 1.4 – 1.5 V [215]. Insofar as the voltammetry is unaffected below 1.35 V, these literature results are similar to the present observations for the addition of solution oxalate. At more positive potentials, most of these organic solution species oxidize at the electrode surface, at or slightly below the diffusion-limited rate [215]. This is in contrast with the anodic peak in Figure 5.2, which qualitatively appears to be a surface-limited process.

The case may be considered in which electrode processes up to the Ni(II)/Ni(III) oxidation peak are unaffected by the presence of solution oxalate. Hence, the usual electrochemical behaviour will be briefly discussed. During a forward potential scan up to the anodic peak at 1.4 V, the nickel electrode surface is covered with an oxide/hydroxide bilayer of limited thickness. At high scan rates, the surface layer is composed of α-$Ni(OH)_2$ and the underlying layer is composed of non-stoichiometric NiO_x. At lower scan rates, the surface hydroxide is typically a mixture of α-$Ni(OH)_2$ and β-$Ni(OH)_2$, where the former phase is a layered, hydrated polymorph of the latter, which is typically the more compact and crystalline form [35, 40].

It may be postulated that solution oxalate does not directly participate in the surface electrochemistry, but rather it chemically adsorbs to the surface hydroxide as it forms. Therefore the oxidation peak at ~1.4 V does not correspond to the adsorption or desorption of solution oxalate, but rather to the oxidation of the oxalate-stabilized surface hydroxide. This hypothesis is

supported by considerable evidence of solution oxalate adsorbing to various metal oxides, hydroxides and oxyhydroxides (e.g., gibbsite, $Al(OH)_3$) [216]. In order to test this idea, an electrode was scanned to 1.35 V in an alkaline, oxalate-containing solution, at which point the electrode was removed and rinsed thoroughly for 30 s with high purity water. The electrode was then returned to the same solution or to a different solution that contained no solution oxalate. Finally, the potential scan was then resumed at the same scan rate. As shown in Figure 5.4, the oxidation peak at 1.4 V remained sharp, independent of the presence of solution oxalate. This experiment conclusively demonstrates that the position and the sharpness of the Ni(II)/Ni(III) anodic peak do not correspond to a reaction involving solution oxalate. The experiment does not, however, indisputably prove whether oxalate truly adsorbs on the surface, or whether its presence during the first voltammetric step chemically modified the surface layer in some other fashion. It is also observed that during the reverse scan, the reduction peak at 1.33 V also remains sharp in the absence of solution oxalate. Therefore, if the oxalate does adsorb onto the $Ni(OH)_2$ surface, it remains adsorbed after the oxidation peak at 1.4 V, which rules out the possibility of an oxidative stripping process.

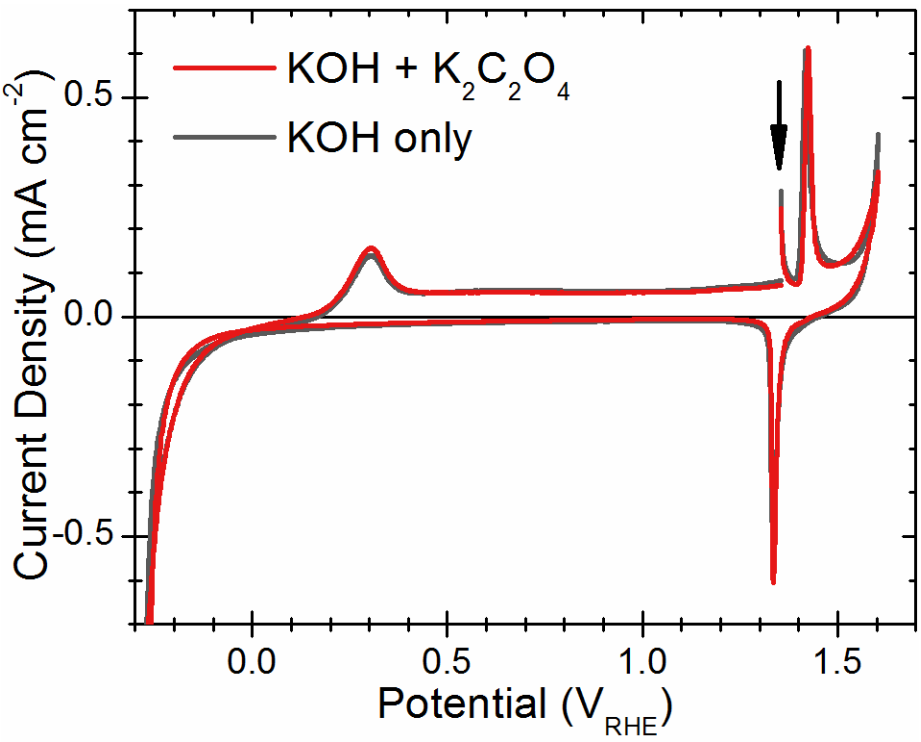

Figure 5.4 Cyclic voltammetry was measured on polished nickel electrodes at 20 mV s^{-1}. The electrolyte solution contained 0.10 M KOH and 0.08 M $K_2C_2O_4$ and was deaerated with H_2. The potential was scanned in the forward direction from -0.3 V_{RHE} to 1.35 V_{RHE} (indicated by the arrow), at which point the electrode was removed and rinsed for 30 s with deionized water. The electrode was then returned to the solution and the potential scan was resumed up to 1.6 V_{RHE} and then reverse-scanned to -0.3 V_{RHE}. The experiment was then repeated, except that after the rinsing step the electrode was placed in a solution that contained only 0.10 M KOH electrolyte (no $K_2C_2O_4$).

5.3.5. FT-IR Evidence of the Adsorption of Oxalate

To conclusively test the oxalate adsorption hypothesis, nickel foil electrodes were scanned to 1.35 V in alkaline solutions, with and without solution oxalate. Then, IR reflectance measurements were conducted to determine the nature of the surface layer. It has been suggested that the electrochemically formed α-$Ni(OH)_2$ surface component has a limiting thickness of two layers [149]. Therefore, the adsorbed oxalate layer is also limited to a maximum thickness of two layers. Therefore, conventional IR reflectance measurements are incapable of detecting these thin surface components. To overcome this limitation, attenuated total reflectance (ATR) FT-IR was employed, in which the IR beam is reflected many times through a high refractive index crystal. When a sample is pressed directly against the crystal surface, the IR beam evanesces into the surface layer and may be absorbed or reflected in the conventional sense. The results of these measurements are shown in Figure 5.5 and the peak assignments are listed in Table 5.3.

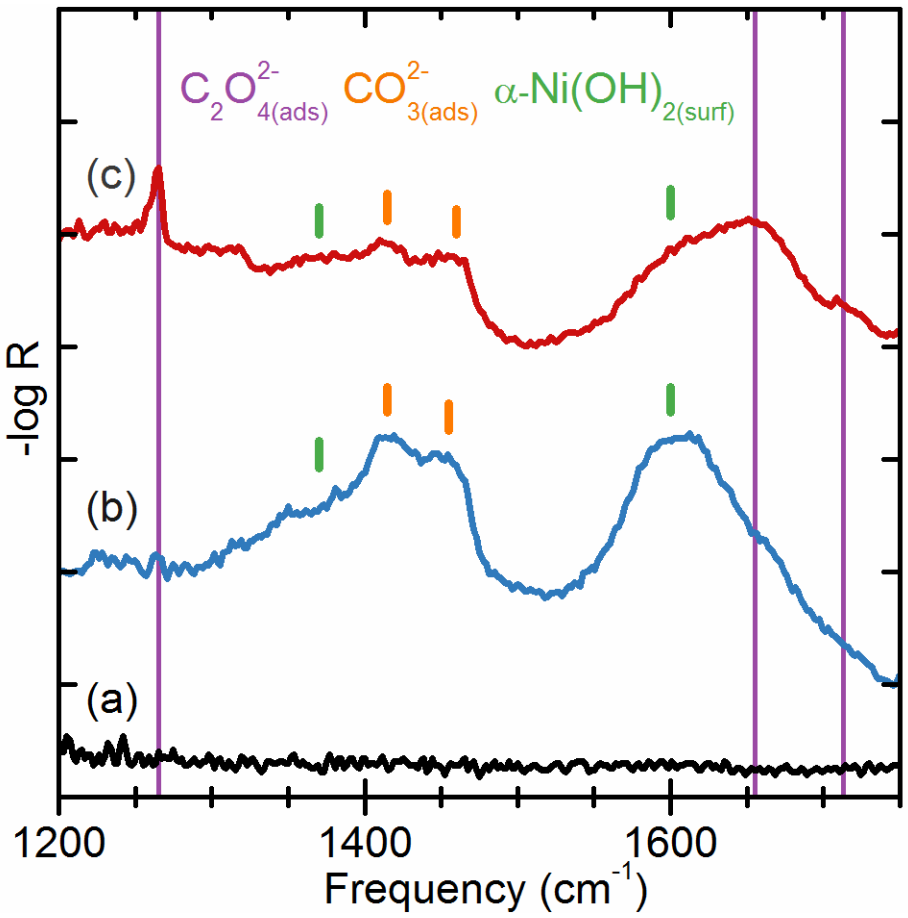

Figure 5.5 ATR-IR spectra of (a) the instrument zero, and collected from a polished nickel foil electrode scanned from -0.3 V to 1.35 V_{RHE} at 20 mV s^{-1} in electrolyte solution containing (b) 0.10 M KOH, or (c) 0.10 M KOH and 0.08 M $K_2C_2O_4$. Tick marks on the y-axis are spaced 0.0005 units apart. The peak assignments shown on the figure are summarized in Table 5.3.

Table 5.3 Infrared absorption peak assignments from ATR FT-IR measurements on Ni foil electrodes shown in Figure 5.5.

	Peak Position		
	(b)	(c)	Assignment
α-$Ni(OH)_{2(surf)}$	1370	1370	O–H bend, lattice OH
	1600	1600	O–H bend, layer H_2O
$CO_3^{2-}{}_{(ads)}$	1415	1415	ν_3, anti-symmetric stretch
	1455	1460	ν_3, anti-symmetric stretch
$C_2O_4^{2-}{}_{(ads)}$		1265	ν_a(C–O)
		1655	ν_a(C=O)
		1713	ν_s(C=O)

The IR peaks were assigned by consulting previous studies and by first considering the spectra collected from the sample prepared without any solution oxalate (Figure 5.5b). Previous ATR-IR investigations on several aluminum and iron oxide/hydroxide surfaces show that adsorbed carbonate ($CO_3^{2-}{}_{(ads)}$) has two strong peaks in this frequency region. These peaks are attributed to the ν_3 asymmetric stretching mode (E'), which is split into two bands in metal carbonates and in adsorbed carbonate species [217, 218]. Further, the ν_3 peak position is typically blue-shifted, relative to the corresponding free carbonate mode (1415 cm^{-1}) [164, 217, 218]. This is consistent with the observed peaks at 1415 cm^{-1} and 1455 cm^{-1}. There are also peaks that are assigned to a surface α-$Ni(OH)_2$ species at 1370 cm^{-1} and 1600 cm^{-1}. These modes arise from O-H bending modes of lattice hydroxide and associated water molecules, respectively. Another lattice hydroxide mode, previously reported at 1480-1490 cm^{-1}, is not observed in my spectra, but is likely just obscured by the adsorbed carbonate modes. Further, the asymmetry of the peak observed at 1600 cm^{-1} may be attributed to convolution with a previously reported peak at ~1630 cm^{-1} [87]. Finally, although a NiO_x component is expected at the electrode surface, NiO_x does not have any IR absorption bands in this frequency range [219]. These peak positions and assignments are listed in Table 5.3.

Next, the IR spectra collected from nickel electrodes prepared in the presence of solution oxalate were examined and the α-$Ni(OH)_{2(surf)}$ and $CO_3^{2-}{}_{(ads)}$ peaks were assigned (Table 5.3). Note that the absorbance of the adsorbed carbonate modes is considerably less from these samples than it is from those prepared in the absence of oxalate. The remaining IR peaks at 1265 cm^{-1}, 1655 cm^{-1} and 1713 cm^{-1} were then assumed to correspond to an adsorbed oxalate species.

Previously reported IR peak positions of oxalate adsorbed several metal oxide/hydroxide/ oxyhydroxide surfaces are summarized in Table 5.4. Note that some of these peaks show some

pH-dependence. For this work, the oxalate is expected to be fully deprotonated (pH_{sol} = 13, pK_{a1} = 1.25, pK_{a2} = 3.81) [22] and so, where applicable, the high pH limit was taken while composing Table 5.4. Most commonly, oxalate adsorbs via the formation of five-membered rings (–Ni–O–C–C–O–),termed mononuclear bidentate (MNBD) in the literature. This gives rise to the set of four modes listed in Table 5.4. The spectrum shown in Figure 5.5c clearly shows two of these modes, at 1265 cm^{-1} and 1713 cm^{-1}. A third peak is observed at ~1655 cm^{-1}, although it is convoluted with the O-H bending modes of the α-$Ni(OH)_{2(surf)}$ species. The fourth expected mode is not observed, but this may be attributed to a convolution with the adsorbed carbonate modes.

In summary, the voltammetric and ATR-IR measurements presented in this section conclusively demonstrate that during a forward voltammetric scan in an alkaline electrolyte that contains an oxalate salt, oxalate anions are indeed adsorbed on the electrochemically formed nickel hydroxide surface.

Table 5.4 Infrared absorption peak positions (cm^{-1}) for adsorbed oxalate on various surfaces.

Surface Formula	Mineral	Vibrational Mode(s) ν_a(C–O)	ν_s(C–O) + ν(C–C)	ν_a(C=O)	ν_s(C=O)	Ref.
Metal Oxides						
α-Al_2O_3	Corundum	1294	1425	1699	1720	[220]
Al_2O_3	[a]	1297	1424	1695	1720	[221]
TiO_2	Anatase	1279	1423	1682	1716	[222]
	Rutile	1275	1424	1679	1713	[222]
	[a]	1271	1424	1686	1711	[221]
α-Fe_2O_3	Hematite	1305	1423	1701	1720	[223]
$Fe_2O_3 \cdot xH_2O$	Ferrihydrite	1280	1412	1668	1708	[211]
ZrO_2	[a]	1284	1432	1673	1708	[221]
Ta_2O_5	[a]	1266	1406	1688	1711	[221]
Metal Hydroxides						
γ-$Al(OH)_3$	Gibbsite	1304	1414	1686	1721	[216]
$Cr_2O_3 \cdot nH_2O$ (n = 11,28)	N/A	1260	1410	1680	1710	[224]
α-$Ni(OH)_2$	N/A	*1265*	- - -	*1655*	*1713*	[b]
Metal Oxyhydroxides						
γ-AlOOH	Boehmite	1288	1413	1702	1722	[225]
	Beohmite	1286	1418	1700	1720	[220]
CrOOH	[a]	1309	1407	1672	1708	[226]
α-FeOOH	Goethite	1255	1427	1692	1713	[227]
γ-FeOOH	Lepidocrocite	1283	1430	1631	1710	[222]

[a]Crystallographic structure not reported

[b]This study

5.3.6. Effect of Potential Cycling on Surface Layer Composition

The reversibility of the Ni(II)/Ni(III) oxidation and reduction processes was tested by cycling through the anodic and cathodic peaks (Figure 5.6). It is known that cycling over this potential range in alkaline solution normally results in the gradual conversion of the reduced electrode mass from α-$Ni(OH)_2$ to β-$Ni(OH)_2$ and increases the thickness of the surface hydroxide [42]. In the context of the present work the specification of the surface layer as either the α- or β-phase may be an oversimplification. Nevertheless, the concept of a transformation from an initial structure to a more compact, crystalline one may be applied to interpret the results in Figure 5.6. The peak and half-wave potentials (Figure 5.6b) from the first 100 cycles indicate that as the surface hydroxide layer transforms, the electrode potential for the more crystalline material is slightly higher than for the initially formed surface layer. Even after 100 cycles, the effect of solution oxalate is clear and the peaks are > 40 mV negative to the oxalate-free positions in Figure 5.2. The peak widths (Figure 5.6c) are consistent with the transition from one pair of peaks to another. That is, they support the idea of an initially formed hydroxide that becomes more compact and crystalline upon cycling. Therefore, the experimentally observed peak widths may actually arise from the superposition of multiple voltammetric peaks, which explains the rise and fall of the peak widths in Figure 5.6c. It is noted that both the peak position and width of the cathodic peak level off more rapidly than those of the anodic peak.

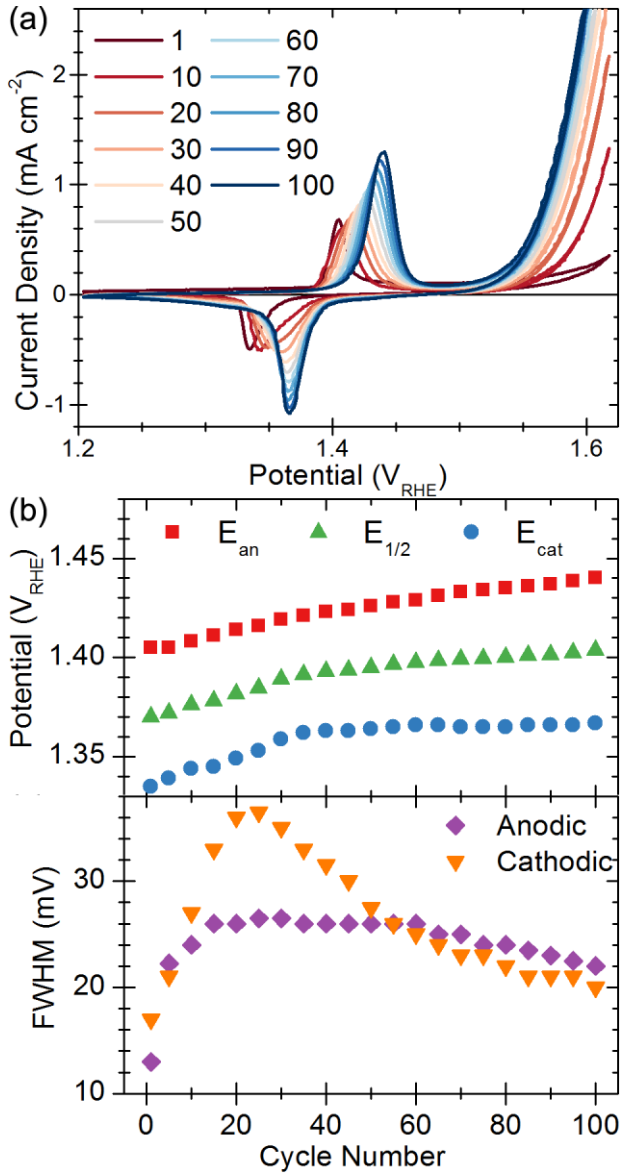

Figure 5.6 Cyclic voltammetry was measured on a polished nickel electrode at 20 mV s^{-1}. The electrolyte solution contained 0.10 M KOH and 0.08 M $K_2C_2O_4$ and was deaerated with H_2. The potential was scanned from -0.3 V – 1.2 V_{RHE} and then cycled between 1.2 – 1.6 V_{RHE}. (a) The cycle numbers are indicated on the graph with the corresponding voltammograms. (b) The anodic peak positions, half-wave potentials, and the cathodic peak positions as functions of cycle number. (c) The FWHM of the anodic and cathodic peaks as a function of cycle number.

5.3.7. Effect of Voltammetric Scan Rate

The effect of the potential scan rate on the voltammetry is qualitatively shown in Figure 5.7. The effect of the scan rate on the positions of the voltammetric peaks is shown in Figure 5.7c. At scan rates greater than 8 mV s^{-1}, the anodic peak potential increases at approximately 7.5 × 10^{-2} mV [mV s^{-1}]$^{-1}$ (i.e., 0.075 s). In contrast, the cathodic peak position is approximately constant at scan rates greater than about 30 mV s^{-1}. The effect of the scan rate on the full-widths at half maximum is shown in Figure 5.7d. Although there appears to be considerable scatter in the data shown in Figure 5.7d, it should be noted that the uncertainty of the measurement (about ±2 mV) appears as a large scatter relative to the very small FWHMs measured in this study. The FWHMs follow a similar trend for both the anodic and cathodic peaks, following a linear trend:

$$FWHM = (12.0 \pm 0.4)\, mV + (0.065 \pm 0.002)\, mV\, (mV\, s^{-1})^{-1} \quad \textbf{(3)}$$

Parameters are presented as the mean ± standard error of the regression (N = 47, R^2 = 0.949). Note that the FWHMs of the anodic peak for scan rates below 5 mV s^{-1} were omitted for this calculation because the widths of the anodic peak increases slightly at such slow scan rates. That being said, even at 1 mV s^{-1}, the FWHM remains quite sharp at 16 mV.

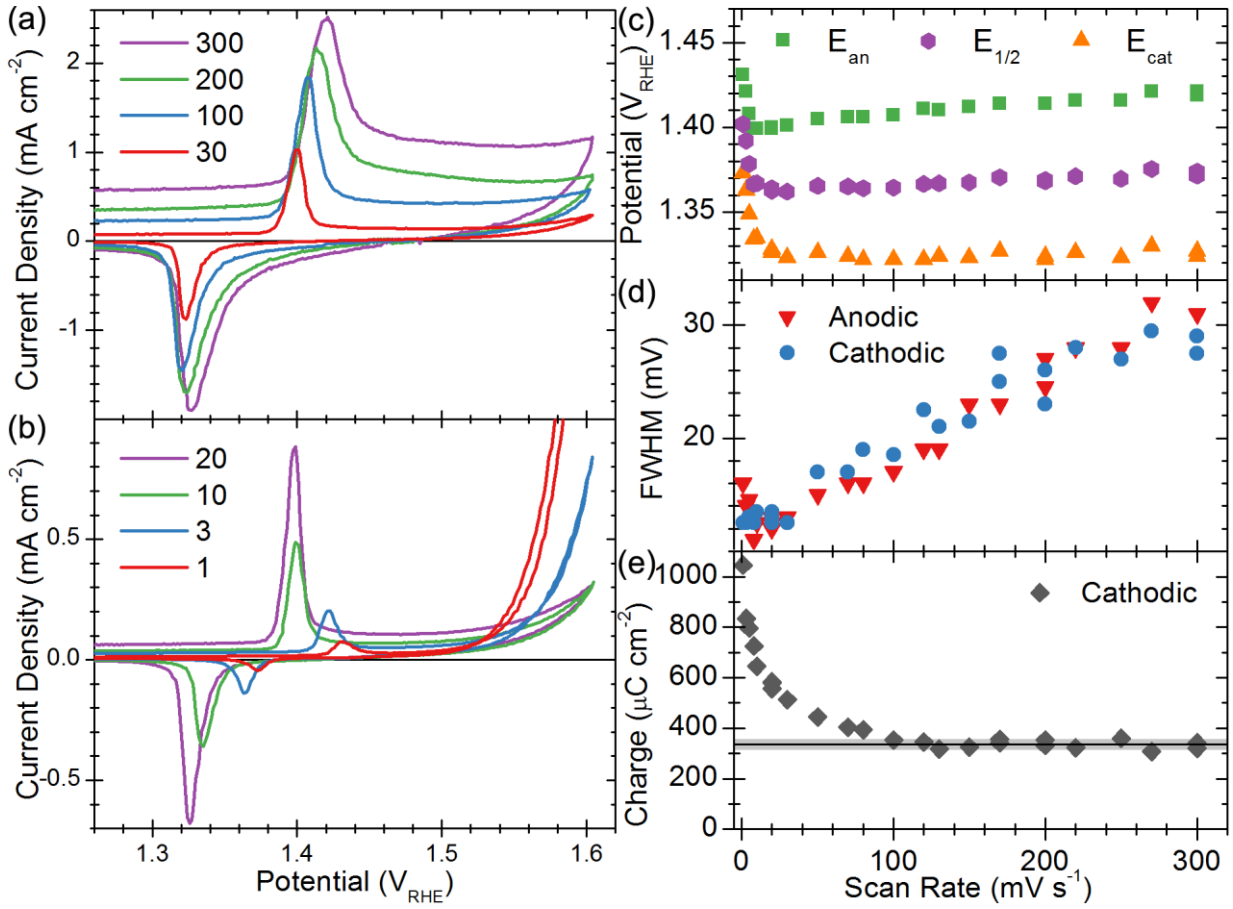

Figure 5.7 Cyclic voltammetry was measured on polished nickel electrodes in an electrolyte solution containing 0.10 M KOH and 0.08 M $K_2C_2O_4$. The solution was deaerated with H_2. (a-b) The potential was cycled between -0.3 V and 1.6 V_{RHE} at the scan rate indicated on the figure (in mV s^{-1}). (c) The positions of the anodic peak (E_{an}), the half-wave potential ($E_{1/2}$), and the cathodic peak (E_{cat}). (d) The FWHM of the anodic and cathodic peaks. (e) The Coulombic charge of the cathodic peak. The tangent (black line and shaded area), as calculated from scan rates ≥ 150 mV s^{-1}, is 336 ± 17 μC cm^{-2} (mean ± standard deviation).

The hypothesis presented in this work thus far is that the electrochemical formation of a nickel hydroxide surface layer occurs normally, i.e., the same as it would in the absence of oxalate. Solution oxalate is subsequently adsorbed onto the surface. The initial surface hydroxide has been presented as a disordered, exfoliated structure analogous to α-$Ni(OH)_2$. However, at slower scan rates, the surface typically consists of a mixture of α- and β-$Ni(OH)_2$ components. The existence of a mixed character surface layer at slower scan rates could explain the slight anodic peak broadening observed for scan rates below 5 mV s^{-1}. Further, the results of the cycling experiment discussed in the previous section and shown in Figure 5.6b show that the peak positions that correspond to a better ordered, β-like surface layer are at slightly higher potentials than for the α-like surface hydroxide. This is consistent with the shift to more positive peak positions at very slow scan rates (Figure 5.7c). Therefore at slower scan rates, the electrochemically formed surface layer has a greater β-like character, whereas at sufficiently fast scan rates, the surface layer may be considered to have exclusively α-like character.

The effect of the scan rate on the anodic charge under the Ni(II)/Ni(III) peak was difficult to investigate because of the large anodic background, attributed to the thickening of the underlying NiO_x layer and the onset of the OER above 1.23 V_{RHE}. Therefore, the cathodic charge associated with the reduction peak during the reverse scan was instead chosen for investigation. This reduction peak was integrated using a linear background, although the background current was very small during the reverse scan for all scan rates studied in this work. Figure 5.7e shows that the cathodic charge decreases with increasing scan rate until it reaches a minimum value between 100 – 150 mV s^{-1}. This minimum value was calculated from the measurements with scan rates ≥ 150 mV s^{-1} and is 336 ± 17 μC cm^{-2} (mean ± standard deviation, N = 10). The

relative standard deviation, 5.2 %, is quite small and may be largely attributed to the mechanical polishing regime used between measurements.

The larger Coulombic charges calculated at slower scan rates indicate that a thicker surface layer is formed at $\nu < 100$ mV s^{-1}. The y-intercept is estimated between 1150 – 1200 μC cm^{-2}, which corresponds to a surface hydroxide that is 3 – 4 layers thick. This estimate utilizes the theoretical value of 195 μC cm^{-2} and the experimentally measured electrode roughness of 1.78 that are calculated and discussed in section 5.3.8. Since the exact thickness is unknown, the low scan rate limit is unsuitable for surface area estimations.

The effect of slower scan rates was further examined by first scanning electrodes at a very slow scan rate, 2 mV s^{-1}, from -0.3 V to +1.35 V_{RHE}. Second, the scan was continued at 2, 20, or 200 mV s^{-1} (Figure 5.8). The results demonstrate that the peak and half-wave potentials are determined by the scan rate before the Ni(II)/Ni(III) oxidation peak, as well as the scan rate during the peak itself. The Coulombic charge, however, is predominantly determined by the scan rate before the peak, rather than the scan rate during the peak itself. This is consistent with the interpretation that, at slower scan rates, a thicker layer with mixed α/β-$Ni(OH)_2$ character forms, whereas at sufficiently fast scan rates a monolayer of α-$Ni(OH)_2$ is formed. However, this interpretation of the slow scan rate results remains unsatisfactory. In particular, the results in Figure 5.7d appear contradictory with those in Figure 5.7e. Whereas the FWHM is quite small at very low scan rates, which usually corresponds to a single layer, the Coulombic charge suggests that the thickness exceeds a monolayer. How then can a multi-layer structure give rise to such a sharp peak? To answer this, one may consider the unusual nature of α-$Ni(OH)_2$, especially its tendency to form unique layered structures. There are numerous literature reports of α-type nickel hydroxides intercalated with organic anions, including cetyltrimethylammonium

bromide,[228], dodecyl sulfate ,[12, 110, 118, 228-233] dodecylbenzene sulfonate,[231] p-aminobenzoate,[234] and Tween 80.[228] Several of these intercalation materials maintain the lattice vibrational modes of the α-$Ni(OH)_2$ parent structure. Furthermore, the Ni–Ni interatomic spacing is also very close to that of the parent materials. However, the presence of intercalated anions generally increases the interlayer spacing of the $Ni(OH)_2$ sheets, which minimizes the chemical interactions between layers. Therefore, the thicker surface layer that forms at slow scan rates may be better described as a supramolecular assembly of many highly ordered monolayers, loosely held together by water and oxalate. This interlayer region is expected to have good ionic conductivity, which would facilitate a rapid electrochemical transformation. This proposed multi-layer structure of oxalate-intercalated α-$Ni(OH)_2$ may well have a slightly different redox potential than the rapidly formed monolayer on the electrode surface. Furthermore, it would indeed have a greater Coulombic charge because of the increased number of Ni atoms. Finally, the high structural order of the individual $Ni(OH)_2$ sheets could still give rise to very sharp voltammetric features, due to rapid transformation from Ni(II) to Ni(III).

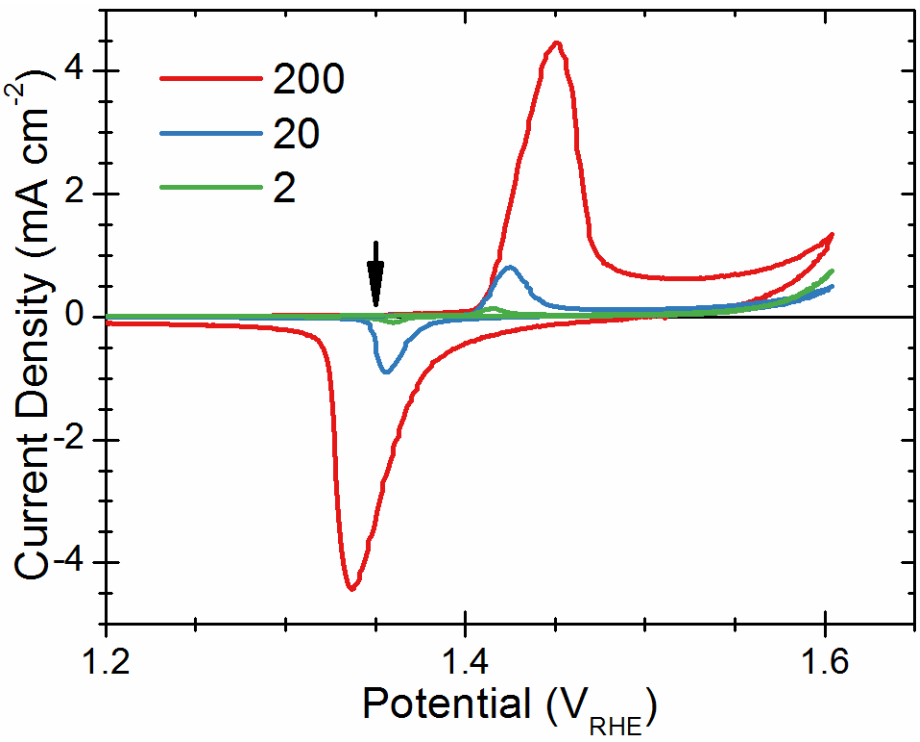

Figure 5.8 Cyclic voltammetry was measured on polished nickel electrodes in an electrolyte solution containing 0.10 M KOH and 0.08 M $K_2C_2O_4$. The solution was deaerated with H_2. The potential was scanned at 2 mV s^{-1} in the forward direction from -0.30 V – 1.35 V_{RHE}, at which point (indicated by the arrow) the scan was continued at 2 mV s^{-1}, 20 mV s^{-1} or 200 mV s^{-1}, as indicated on the graph.

5.3.8. A New Method of Surface Area Measurements on Nickel Electrodes

The voltammetric peaks in this work are exceptionally sharp, despite being measured on mechanically polished polycrystalline nickel. Previously reported peaks of similar sharpness involve surface layers formed on single crystal electrodes and are treated as rapid phase transitions at the surface [235]. For example, the FWHM of Pb underpotential deposition onto Pt (111) in the presence of HI can be as little as 5 mV [236]. In another example, voltammetric peak widths reported from the reductive desorption of several alkanethiols on Au(111) is 20 mV [237]. The sharpness of these peaks may be attributed to the formation or deformation of highly ordered surface layers on a single crystal face. This is commonly represented by the Frumkin adsorption isotherm, which introduces a lateral interaction parameter, f, to the Langmuir isotherm. Sharp voltammetric peaks occur when these lateral interactions are attractive in nature ($f < 0$) [141, 238]. For sufficiently strong lateral interactions, voltammetric sweeps may induce a rapid phase transformation at the surface [235, 238]. In general, electron transfer involving more than a monolayer or occurring on multiple crystal faces does not give rise to a single sharp peak. Moreover, such sharp peaks generally correspond to a quick transition from very low ($\theta \approx 0$) to very high ($\theta \approx 1$) surface coverage, rather than electron transfer involving only part of the surface layer [141].

These results are consistent with the oxidation and reduction on a particular surface orientation of $Ni(OH)_2$, which may be logical upon examination of the material's structure. Both α- and β-phases are composed of hexagonal sheets of $Ni(OH)_2$. If oxalate adsorbs onto the surface hydroxide as it forms, it would likely do so on the (001) face by substitution of lattice hydroxide sites. This may prevent the growth of adjacent layers, limiting growth of the $Ni(OH)_2$ sheets to within the plane defined by the crystallographic a- and b-axes (the ab-plane). Thus, the

resulting structure may be very generally represented as $Ni(OH)_{2-x}(C_2O_4)_{x(ads)}$, where $0 \leq x \leq 2$. This stoichiometry merely states the limiting cases of hydroxide substitution, whereas further investigation is necessary to determine the true value of x.

From the cycling experiment discussed in section 5.3.6, and the scan rate experiments discussed in Section 5.3.7, it is known that at sufficiently high scan rates, the surface layer is analogous to α-$Ni(OH)_2$ and from the layered structure, I assume that the surface area of this layer corresponds to the (001) orientation. It is reasonable to assume that the oxidation and reduction peaks correspond to the Ni(II)/Ni(III) redox pair and are therefore one-electron processes. I therefore used the limiting charge shown in Figure 5.7e and the unit cell parameters of α-$Ni(OH)_2$ to estimate the surface area of the polished electrode. From the hexagonal structure of the $Ni(OH)_2$ sheet, the area for each Ni atom is:

$$A = \frac{\sqrt{3}}{2} d^2 \qquad \textbf{(4)}$$

Where d is the Ni–Ni spacing (3.08 Å for α-$Ni(OH)_2$ and a = 3.13 Å for β-$Ni(OH)_2$) [34, 53]. Therefore, the calculated area is 8.22 $Å^2$ $atom^{-1}$, or 195 μC cm^{-2} for a planar electrode. Thus, the roughness factor of the mechanically polished electrode in this work is 1.72 ± 0.09 (mean ± standard deviation), which is a reasonable value. Note that the Ni–Ni spacing of β-$Ni(OH)_2$ is only 0.05 Å greater than in the α-$Ni(OH)_2$ structure, which corresponds to a 3 % difference in the estimated roughness factor (1.78). Furthermore, the Ni–Ni spacing of intercalated α-derivative materials is usually very close, within a few percent, to the spacing of the α-$Ni(OH)_2$ parent material. Therefore, the combined measurement error is estimated to be less than 10 %.

Clearly, further investigation is required to conclusively determine what occurs at slow scan rates. However, the low scan rate behaviour does not affect the interpretation of the high scan rate results. That is, when $\nu \geq 150$ mV s^{-1}, solution oxalate limits the growth of the surface

layer to a single layer, which can be utilized to estimate the value of A_{ECSA}. Therefore the addition of oxalate to an alkaline solution may be used to measure the electrochemically active surface area, *in situ*, with good accuracy and precision.

There remain several potential obstacles that require further experimentation before this method may be applied to real electrode systems. The selectivity of this method to nickel is unknown, which may affect measurements of mixed metal (Ni_xZn_y, etc.) and supported Ni electrodes. Further, it is unknown whether this method will be affected by prolonged hydrogen evolution, which is known to incorporate hydrogen atoms into the electrode material and, thus, alter the surface state.[40] It is also uncertain how the experimental parameters, such as potential scan rate and oxalate concentration, would need to be altered for measuring very high surface area electrodes (Ni foams, electrodeposited coatings, etc.). Alternatively, future work may utilize the method presented in this work on low surface area nickel electrodes to obtain reference values for the double-layer capacitance, C_{dl}, which may be measured on high surface area materials by EIS or potential-step methods. Once reference values are established, it will be possible to calculate the A_{ECSA} from the measured C_{dl} values.

5.4. Conclusions

A new method of measuring the electrochemically active surface area of nickel electrodes, *in situ*, is presented. The addition of 0.08 mol L^{-1} of an oxalate salt to the alkaline electrolyte solution shifts the half-wave potential of the Ni(II)/Ni(III) redox pair by about -80 mV. Further, the presence of solution oxalate decreases the corresponding voltammetric peak widths considerably. The sharpest peak observed in this work has a FWHM of just 11 mV, despite the use of mechanically polished polycrystalline nickel. Voltammetry demonstrates that

solution oxalate adsorbs onto the surface nickel hydroxide layer. The presence of adsorbed oxalate was confirmed by ATR-IR absorption peaks at 1265 cm^{-1}, 1655 cm^{-1}, and 1713 cm^{-1}. At slower scan rates, the composition of the surface hydroxide is of mixed α/β-$Ni(OH)_2$ character and its thickness is estimated between 3 – 4 layers thick. When scan rates of 150 mV s^{-1} or greater are employed, only a monolayer of α-$Ni(OH)_{2(surf)}$ forms. Although the Ni(II)/Ni(III) oxidation peak overlaps with the OER at higher scan rates, the cathodic peak is very well separated from other electrode processes. Therefore, this peak may be integrated with high precision using a simple linear background. Since this oxidation process apparently corresponds to a one-electron process for a single layer of an α-$Ni(OH)_2$-like surface layer, the unit cell parameters may be used to correlate experimentally measured Coulombic charge with an electrochemically active surface layer. By assuming a Coulombic charge of 195 μC cm^{-2}, the roughness factor of the electrodes used in this work was calculated to be 1.78 ± 0.09 (mean ± standard deviation).

In conclusion, this work has successfully established a method to measure the surface area of an electrode by simply adding oxalate to the alkaline electrolyte. The error of the measurements is estimated at less than 10 %. Furthermore, this error is primarily attributed to variations that arose from the mechanical polishing step between measurements, rather than imprecision of the measurement method.

6. General Conclusions

6.1. Specific Claims of Original Research

(1) All of the vibrational modes of β-$Ni(OH)_2$ predicted by factor group theory were assigned to experimentally measured IR and Raman peaks.

(2) A simplified model of the structures of $Ni(OH)_2$ materials is presented. This model consists of two fundamental phases (α and β) that may adopt various types and extents of structural disorder. This scheme unifies decades of spectroscopic and crystallographic investigations and rationalizes all observed IR- and Raman-active modes of α-$Ni(OH)_2$ and β-$Ni(OH)_2$ materials, including those caused by foreign ion incorporation, stacking fault disorder, hydration, and internal mechanical stress.

(3) From the IR and Raman spectra, it is concluded that nitrate anions incorporated into α-$Ni(OH)_2$ materials may occupy two distinct chemical environments: (a) the anions may reside within the interlayer region, which is chemically very similar to free solution, or (b) the anions may occupy a site with reduced symmetry, likely by substation with hydroxide anions.

(4) The vibrational spectroscopy methods described in this thesis may be used to quickly identify pure and mixed-phase samples of α- and β-$Ni(OH)_2$, either *in situ* or *ex situ*. It is concluded that the high intensity (Raman) or high absorbance (IR) O–H stretching modes serve as 'fingerprint' peaks.

(5) It was demonstrated that α-$Ni(OH)_2$ materials may be chemically transformed to β-$Ni(OH)_2$ by treatment in pure water at room temperature. Previously, this aging

process has primarily been studied in concentrated alkaline solutions at elevated temperatures (*e.g.*, 30 % KOH at 80 °C). The aging process occurs more slowly than it does at higher temperatures. From the Raman spectra, the β-$Ni(OH)_2$ product does not appear to have significant stacking fault disorder.

(6) It is observed that during chemical aging of nitrate-containing α-$Ni(OH)_2$ materials, the nitrate anions are very quickly removed (~1 day) relative to the phase transition (incomplete after 43 days).

(7) A simplified schematic of the α- to β-$Ni(OH)_2$ aging process is presented. Near the α/β phase boundary, internal mechanical stresses arise from the mismatch in the crystallographic c-parameters ($c_\alpha \approx 8.0$ Å, $c_\beta \approx 4.6$ Å), which cause the observed blue-shift and red-shift of the α- and β-$Ni(OH)_2$ O–H stretching modes, respectively. An additional Raman mode is predicted for water molecules situated near the phase boundary, which I ascribe to a new peak observed at 3520 cm^{-1}.

(8) I present the first direct evidence of α-NiH_x formed electrochemically in alkaline media. This is the first proof that this phase indeed can form from Ni metal in alkaline media and addresses a decades-old gap in the literature.

(9) It is concluded that when a nickel electrode is polarized in alkaline media near the RHE potential, H atoms are incorporated deep into the Ni material as interstitial impurities. At sufficiently high concentrations, α-NiH_x or β-NiH_x can form. The deactivation of Ni cathodes during prolonged hydrogen evolution is attributed to the presence of this interstitial H and the formation of these hydride phases.

(10) Previously unexplained voltammetric oxidation peaks measured on nickel electrodes in alkaline media are attributed to the oxidative removal of

incorporated H. This assignment rationalizes previously unexplained experimental irreproducibility and dependence on electrode history and pre-treatment.

(11) Transient current reversal of industrial electrolysers may form NiOOH surface layers on Ni electro-catalysts. This layer may then be reduced back to Ni metal, aside from a small amount of nickel oxide/hydroxide that may always be present at the electrode surface. However, repeated cycling of the oxidation state can change the surface roughness, which could negatively affect electro-catalyst performance.

(12) The addition of 0.08 M oxalate salt to a 0.1 M KOH alkaline electrolyte solution shifts the voltammetric peaks from the Ni(II)/Ni(III) oxidation/reduction by about -80 mV. Its presence also significantly increases the peak FWHM to $\leq$ 30 mV, despite the use of mechanically polished, polycrystalline Ni.

(13) ATR-IR measurements show that solution oxalate spontaneously forms a five-membered mononuclear bidentate ring with α- and β-$Ni(OH)_2$ surface layers, presumably on the (001) surface.

(14) At sufficiently fast potential sweep rates ($v \geq 150$ mV s^{-1}), the presence of at least 0.08 M oxalate limits the surface hydroxide growth to a single layer. The voltammetric reduction peak from this process may be utilized to measure the surface area of a Ni electrode by assuming a reference charge $Q_{ref} = 195$ μC cm^{-2}. The experimental error of this method is estimated at less than 10 %.

6.2. Specific Technical Contributions to the Research

I prepared all of the materials that were used in this thesis. This includes the electrochemically precipitated α-$Ni(OH)_2$, the chemically aged β-$Ni(OH)_2$, and the metallic nickel rod and foil electrodes. All Raman spectroscopy measurements were performed by Shawn Poirier (NRC). I jointly analyzed the Raman spectra with David Lockwood (NRC). I performed all FT-IR measurements, including the collection of the ATR-IR spectra. I jointly analyzed the FT-IR reflectance spectra in chapter 2 with David Lockwood. I analyzed the ATR-IR spectra in chapter 5. I performed all XPS measurements with technical assistance from David Kingston (NRC). I analyzed the measured spectra, including the curve-fitting. All XRD measurements were performed by Bussaraporn Patarachao with my input regarding experimental parameters. I analyzed the measured XRD patterns. I performed all electrochemical experiments and analyzed the data. Finally, I prepared all graphics, figures and data tables that appear in this thesis.

6.3. General Conclusions

The long-term motivation of this research is the development of better Ni-based electro-catalysts, especially for applications in electrolytic hydrogen production. Although further work is required, this thesis lays considerable groundwork necessary to achieve this ultimate goal through the characterization of known materials using spectroscopic and electrochemical methods. In the first half of this thesis, I utilized vibrational spectroscopy to characterize the two phases of $Ni(OH)_2$ and the possible types of structural disorder that they may adopt. Next, I applied these results and demonstrated how Raman spectroscopy may be utilized to identify and characterize $Ni(OH)_2$ materials and surface layers *in situ*. In the second half of this thesis, I fully rationalized the voltammetric behaviour of nickel electrodes in alkaline media and determined

that during prolonged hydrogen evolution, hydrogen is incorporated into the electrode material and causes electro-catalyst deactivation. Finally, I applied my knowledge from the previous sections to develop a voltammetric method of measuring the A_{ECSA} of nickel electrodes *in situ* via the addition of an oxalate salt to the electrolyte solution.

Using the spectroscopic methods developed in this thesis, the combined effects of $Ni(OH)_2$ microstructure, including the material phase and structural disorder, may be compared with practical properties, such as electro-catalytic activity. For example, work is ongoing to differentiate the effects of Fe impurities and $Ni(OH)_2$ phase on the activity of electro-catalysts for the OER [239]. In another example, the spectroscopic methods in this thesis were applied to identify structural disorder in $Ni(OH)_2$/carbon composite materials, under development as supercapacitors [240]. The additional benefits of being able to perform these measurements *in situ* will further facilitate advances in the study of $Ni(OH)_2$ materials and surface layers.

The results of the voltammetric investigation contained in this thesis may be utilized to address the problem of electrode deactivation during prolonged electrolytic hydrogen production. Using the conclusions from this thesis, future work may investigate how to suppress or eliminate electro-catalyst deactivation. The results have also found a general usefulness for identifying voltammetric peaks on Ni and Ni-based electrodes (*e.g.*, [11, 241]).

My new method of surface area measurement may be used to conduct truly objective comparisons of Ni-based electro-catalysts, either for hydrogen production, oxygen evolution, or any other process. One possible approach is to first utilize the new method presented in this thesis to compile a reference dataset with the C_{dl} of metallic Ni at different electrolyte solution concentrations and at various electrode potentials. Then, EIS measurements may be used henceforth as a facile method to measure A_{ECSA} with precision and accuracy. Furthermore, the

sharpness of the voltammetric features in the presence of solution oxalate is fundamentally interesting. To the best of my knowledge, such sharp voltammetric peaks have never before been measured on mechanically polished, polycrystalline electrodes. Rather, such narrow peak widths are typical of surface processes on single crystal surfaces. Therefore, these findings are a source of simple scientific curiosity.

To summarize, the motivation for the research is the continuing improvement of electro-catalysts for the electrolytic production of hydrogen. The results also have value for research into other applications, including photo-catalysis, secondary batteries, supercapacitors, electrochromic devices, and electro-catalysts for other applications. Using spectroscopic and voltammetric techniques, I have developed methods to directly address specific research problems. In conclusion, I hope that this work will be utilized to develop improved materials and devices with real commercial or industrial value.

7. References

1. Thompson, L., Barbier, F., Burns, L., Friedland, R., Kiczek, E., Nozik, A., Richmond, G., Shaw, R. & Wilson, D. 2013 Report of the Hydrogen Production Expert Panel: A Subcommittee of the Hydrogen & Fuel Cell Technical Advisory Committee. (Washington D.C., USA, United States Department of Energy.
2. Zeng, K. & Zhang, D. 2010 Recent progress in alkaline water electrolysis for hydrogen production and applications. *Progr. Energy Combust. Sci.* **36**, 307-326. (doi:10.1016/j.pecs.2009.11.002).
3. 2007 IEA Energy Technology Essentials: Hydrogen Production & Distribution. (International Energy Association.
4. Dunn, S. 2002 Hydrogen futures: toward a sustainable energy system. *Int. J. Hydrogen Energy* **27**, 235-264. (doi:10.1016/s0360-3199(01)00131-8).
5. Pletcher, D., Li, X. & Wang, S. 2012 A comparison of cathodes for zero gap alkaline water electrolysers for hydrogen production. *Int. J. Hydrogen Energy* **37**, 7429-7435. (doi:10.1016/j.ijhydene.2012.02.013).
6. Tang, X., Xiao, L., Yang, C., Lu, J. & Zhuang, L. 2014 Noble fabrication of Ni–Mo cathode for alkaline water electrolysis and alkaline polymer electrolyte water electrolysis. *Int. J. Hydrogen Energy* **39**, 3055-3060. (doi:10.1016/j.ijhydene.2013.12.053).
7. Hutton, L.A., Vidotti, M., Patel, A.N., Newton, M.E., Unwin, P.R. & Macpherson, J.V. 2010 Electrodeposition of Nickel Hydroxide Nanoparticles on Boron-Doped Diamond Electrodes for Oxidative Electrocatalysis. *The Journal of Physical Chemistry C* **115**, 1649-1658. (doi:10.1021/jp109526b).

8. McBreen, J. 2011 Nickel Hydroxides. In *Handbook of Battery Materials* (eds. C. Daniel & J.O. Besenhard), pp. 149-168, 2nd ed. Weinheim, Germany, Wiley-VCH Verlag GmbH & Co. KGaA.

9. Li, X., Walsh, F.C. & Pletcher, D. 2011 Nickel based electrocatalysts for oxygen evolution in high current density, alkaline water electrolysers. *Phys. Chem. Chem. Phys.* **13**, 1162-1167. (doi:10.1039/c0cp00993h).

10. Miao, Y., Ouyang, L., Zhou, S., Xu, L., Yang, Z., Xiao, M. & Ouyang, R. 2014 Electrocatalysis and electroanalysis of nickel, its oxides, hydroxides and oxyhydroxides toward small molecules. *Biosensors and Bioelectronics* **53**, 428-439. (doi:10.1016/j.bios.2013.10.008).

11. Siegert, M., Yates, M.D., Call, D.F., Zhu, X., Spormann, A. & Logan, B.E. 2014 Comparison of Nonprecious Metal Cathode Materials for Methane Production by Electromethanogenesis. *ACS Sustainable Chemistry & Engineering*. (doi:10.1021/sc400520x).

12. Wang, D., Yan, W. & Botte, G.G. 2011 Exfoliated nickel hydroxide nanosheets for urea electrolysis. *Electrochem. Commun.* **13**, 1135-1138. (doi:10.1016/j.elecom.2011.07.016).

13. Abouatallah, R.M., Kirk, D.W., Thorpe, S.J. & Graydon, J.W. 2001 Reactivation of nickel cathodes by dissolved vanadium species during hydrogen evolution in alkaline media. *Electrochim. Acta* **47**, 613-621. (doi:10.1016/s0013-4686(01)00777-0).

14. Machado, S.A.S., Tiengo, J., de Lima Neto, P. & Avaca, L.A. 1994 The influence of H-absorption on the cathodic response of high area nickel electrodes in alkaline solutions. *Electrochim. Acta* **39**, 1757-1761. (doi:10.1016/0013-4686(94)85161-1).

15. Makrides, A.C. 1962 Hydrogen Overpotential on Nickel in Alkaline Solution. *J. Electrochem. Soc.* **109**, 977-984. (doi:10.1149/1.2425216).

16. Rommal, H.E.G. & Moran, P.J. 1985 Time-Dependent Energy Efficiency Losses at Nickel Cathodes in Alkaline Water Electrolysis Systems. *J. Electrochem. Soc.* **132**, 325-329. (doi:10.1149/1.2113831).

17. Rommal, H.E.G. & Morgan, P.J. 1988 The Role of Absorbed Hydrogen on the Voltage-Time Behavior of Nickel Cathodes in Hydrogen Evolution. *J. Electrochem. Soc.* **135**, 343-346. (doi:10.1149/1.2095612).

18. Soares, D.M., Teschke, O. & Torriani, I. 1992 Hydride Effect on the Kinetics of the Hydrogen Evolution Reaction on Nickel Cathodes in Alkaline Media. *J. Electrochem. Soc.* **139**, 98-105. (doi:10.1149/1.2069207).

19. Chen, L. & Lasia, A. 1992 Study of the Kinetics of Hydrogen Evolution Reaction on Nickel-Zinc Powder Electrodes. *J. Electrochem. Soc.* **139**, 3214-3219. (doi:10.1149/1.2069055).

20. Chen, L. & Lasia, A. 1992 Hydrogen Evolution Reaction on Nickel-Molybdenum Powder Electrodes. *J. Electrochem. Soc.* **139**, 3458-3464. (doi:10.1149/1.2069099).

21. McKone, J.R., Sadtler, B.F., Werlang, C.A., Lewis, N.S. & Gray, H.B. 2012 Ni–Mo Nanopowders for Efficient Electrochemical Hydrogen Evolution. *ACS Catalysis* **3**, 166-169. (doi:10.1021/cs300691m).

22. 2014 *CRC Handbook of Chemistry and Physics (Internet Version 2014)*. 94 ed. Boca Raton, FL, USA: CRC Press/Taylor and Francis.

23. Kerfoot, D.G.E. 2000 Nickel. In *Ullmann's Encyclopedia of Industrial Chemistry* (Wiley-VCH Verlag GmbH & Co. KGaA.

24. Kuck, P.H. 2013 Nickel. In *Mineral Commodity Summaries* (U.S. Geological Survey.

25. Aghazadeh, M., Golikand, A.N. & Ghaemi, M. 2011 Synthesis, Characterization, and Electrochemical Properties of Ultrafine β-$Ni(OH)_2$ Nanoparticles. *Int. J. Hydrogen Energy* **36**, 8674-8679. (doi:10.1016/j.ijhydene.2011.03.144).

26. Bode, H., Dehmelt, K. & Witte, J. 1966 Zur Kenntnis der Nickelhydroxidelektrode-I. Über das Nickel(II)-Hydroxidhydrat. *Electrochim. Acta* **11**, 1079-1087. (doi:10.1016/0013-4686(66)80045-2).

27. Dhar, S.K., Ovshínsky, S.R., Gifford, P.R., Corrigan, D.A., Fetcenko, M.A. & Venkatesan, S. 1997 Nickel/metal hydride technology for consumer and electric vehicle batteries—a review and up-date. *J. Power Sources* **65**, 1-7. (doi:10.1016/s0378-7753(96)02599-2).

28. Gong, L., Liu, X. & Su, L. 2011 Facile Solvothermal Synthesis $Ni(OH)_2$ Nanostructure for Electrochemical Capacitors. *J. Inorg. Organomet. Polym. Mater.* **21**, 866-870. (doi:10.1007/s10904-011-9519-1).

29. Gourrier, L., Deabate, S., Michel, T., Paillet, M., Hermet, P., Bantignies, J.-L. & Henn, F. 2011 Characterization of Unusually Large "Pseudo-Single Crystal" of β-Nickel Hydroxide. *J. Phys. Chem. C* **115**, 15067-15074. (doi:10.1021/jp203222t).

30. Kober, F.P. 1965 Analysis of the Charge-Discharge Characteristics of Nickel-Oxide Electrodes by Infrared Spectroscopy. *J. Electrochem. Soc.* **112**, 1064-1067. (doi:10.1149/1.2423361).

31. Kober, F.P. 1967 Infrared Spectroscopic Investigation of Charged Nickel Hydroxide Electrodes. *J. Electrochem. Soc.* **114**, 215-218. (doi:10.1149/1.2426549).

32. Lee, J.W., Ahn, T., Soundararajan, D., Ko, J.M. & Kim, J.-D. 2011 Non-Aqueous Approach to the Preparation of Reduced Graphene Oxide/α-$Ni(OH)_2$ Hybrid Composites and Their High Capacitance Behavior. *Chem. Commun.* **47**, 6305-6307. (doi:10.1039/C1CC11566A).

33. Li, B., Cao, H., Shao, J., Zheng, H., Lu, Y., Yin, J. & Qu, M. 2011 Improved performances of [small beta]-Ni(OH)2@reduced-graphene-oxide in Ni-MH and Li-ion batteries. *Chem. Commun.* **47**, 3159-3161. (doi:10.1039/C0CC04507A).

34. McEwen, R.S. 1971 Crystallographic studies on nickel hydroxide and the higher nickel oxides. *J. Phys. Chem.* **75**, 1782-1789. (doi:10.1021/j100681a004).

35. Oliva, P., Leonardi, J., Laurent, J.F., Delmas, C., Braconnier, J.J., Figlarz, M., Fievet, F. & de Guibert, A. 1982 Review of the Structure and the Electrochemistry of Nickel Hydroxides and Oxy-Hydroxides. *J. Power Sources* **8**, 229-255. (doi:10.1016/0378-7753(82)80057-8).

36. Palacín, M.R. 2009 Recent Advances in Rechargeable Battery Materials: A Chemist's Perspective. *Chem. Soc. Rev.* **38**, 2565-2575. (doi:10.1039/B820555H).

37. Burke, L.D. & Whelan, D.P. 1980 Growth of an electrochromic film on nickel in base under potential cycling conditions. *J. Electroanal. Chem. Interfacial Electrochem.* **109**, 385-388. (doi:10.1016/S0022-0728(80)80139-2).

38. Torresi, R.M., Vázquez, M.V., Gorenstein, A. & Córdoba de Torresi, S.I. 1993 Infrared Characterization of Electrochromic Nickel Hydroxide Prepared by Homogeneous Chemical Precipitation. *Thin Solid Films* **229**, 180-186. (doi:10.1016/0040-6090(93)90361-R).

39. Yu, J., Hai, Y. & Cheng, B. 2011 Enhanced Photocatalytic H_2-Production Activity of TiO_2 by $Ni(OH)_2$ Cluster Modification. *J. Phys. Chem. C* **115**, 4953-4958. (doi:10.1021/jp111562d).

40. Hall, D.S., Bock, C. & MacDougall, B.R. 2013 The Electrochemistry of Metallic Nickel: Oxides, Hydroxides, Hydrides and Alkaline Hydrogen Evolution. *J. Electrochem. Soc.* **160**, F235-F243. (doi:10.1149/2.026303jes).

41. Medway, S.L., Lucas, C.A., Kowal, A., Nichols, R.J. & Johnson, D. 2006 In Situ Studies of the Oxidation of Nickel Electrodes in Alkaline Solution. *J. Electroanal. Chem.* **587**, 172-181. (doi:10.1016/j.jelechem.2005.11.013).

42. Visscher, W. & Barendrecht, E. 1983 Anodic oxide films of nickel in alkaline electrolyte. *Surf. Sci.* **135**, 436-452. (doi:10.1016/0039-6028(83)90235-2).

43. Larramona, G. & Gutiérrez, C. 1990 The Nickel Electrode: A Potential-Modulated Reflectance Study. *J. Electrochem. Soc.* **137**, 428-435. (doi:10.1149/1.2086457).

44. MacDougall, B. & Cohen, M. 1974 Anodic Oxidation of Nickel in Neutral Sulfate Solution. *J. Electrochem. Soc.* **121**, 1152-1159. (doi:10.1149/1.2402003).

45. MacDougall, B. & Graham, M.J. 1981 Growth of Thick Anodic Oxide Films on Nickel in Borate Buffer Solution. *J. Electrochem. Soc.* **128**, 2321-2325. (doi:10.1149/1.2127242).

46. Melendres, C.A. & Pankuch, M. 1992 On the Composition of the Passive Film on Nickel: A Surface-Enhanced Raman Spectroelectrochemical Study. *J. Electroanal. Chem.* **333**, 103-113. (doi:10.1016/0022-0728(92)80384-g).

47. Machet, A., Galtayries, A., Zanna, S., Klein, L., Maurice, V., Jolivet, P., Foucault, M., Combrade, P., Scott, P. & Marcus, P. 2004 XPS and STM Study of the Growth and

Structure of Passive Films in High Temperature Water on a Nickel-Base Alloy. *Electrochim. Acta* **49**, 3957-3964. (doi:10.1016/j.electacta.2004.04.032).

48. Zhang, X., Zagidulin, D. & Shoesmith, D.W. 2013 Characterization of Film Properties on the NiCrMo Alloy C-2000. *Electrochim. Acta* **89**, 814-822. (doi:10.1016/j.electacta.2012.11.029).

49. Livingstone, A. & Bish, D. 1982 On the New Mineral Theophrastite, a Nickel Hydroxide, From Unst, Shetland, Scotland. *Mineral. Mag.* **46**, 1-5. (doi:10.1180/minmag.1982.046.338.01).

50. Marcopoulos, T. & Economou, M. 1981 Theophrastite, $Ni(OH)_2$, a New Mineral From Northern Greece. *Am. Mineral.* **66**, 1020-1021.

51. Szytula, A., Murasik, A. & Balanda, M. 1971 Neutron Diffraction Study of $Ni(OH)_2$. *Phys. Status Solidi B* **43**, 125-128. (doi:10.1002/pssb.2220430113).

52. Greaves, C. & Thomas, M.A. 1986 Refinement of the structure of deuterated nickel hydroxide, $Ni(OD)_2$, by powder neutron diffraction and evidence for structural disorder in samples with high surface area. *Acta Crystallogr., Sect. B: Struct. Sci.* **42**, 51-55. (doi:10.1107/S0108768186098592).

53. Pandya, K.I., O'Grady, W.E., Corrigan, D.A., McBreen, J. & Hoffman, R.W. 1990 Extended X-Ray Absorption Fine Structure Investigations of Nickel Hydroxides. *J. Phys. Chem.* **94**, 21-26. (doi:10.1021/j100364a005).

54. Le Bihan, S. & Figlarz, M. 1973 Note sur l'article: “Zur kenntnis der Nickel-hydroxidelektrode—III. Thermogravimetrische Untersuchungen an Nickel(II)-hydroxigen” par W. Dennstedt et W. Löser. *Electrochim. Acta* **18**, 123-124. (doi:10.1016/0013-4686(73)87021-5).

55. Le Bihan, S., Guenot, J. & Figlarz, M. 1970 Sur la cristallogénèse de l'hydroxyde de nickel $Ni(OH)_2$. *Compte Rendu de l'Académie des Science: Paris* **270**, 2131-2133.

56. Delahaye-Vidal, A., Beaudoin, B., Sac-Epée, N., Tekaia-Elhsissen, K., Audemer, A. & Figlarz, M. 1996 Structural and textural investigations of the nickel hydroxide electrode. *Solid State Ionics* **84**, 239-248. (doi:10.1016/0167-2738(96)00030-6).

57. de Oliveira, E.F. & Hase, Y. 2003 Infrared study of magnesium–nickel hydroxide solid solutions. *Vib. Spectrosc.* **31**, 19-24. (doi:10.1016/s0924-2031(02)00049-8).

58. Faure, C., Delmas, C. & Fouassier, M. 1991 Characterization of a Turbostratic α-Nickel Hydroxide Quantitatively Obtained from an $NiSO_4$ Solution. *J. Power Sources* **35**, 279-290. (doi:10.1016/0378-7753(91)80112-B).

59. Jackovits, J.F. 1982 In *Proceedings of the Symposium on the Nickel Electrode* (eds. R.G. Funther & S. Gross), pp. 48-68, The Electrochemical Society.

60. Kamath, P.V., Therese, G.H.A. & Gopalakrishnan, J. 1997 On the existence of hydrotalcite-like phases in the absence of trivalent cations. *J. Solid State Chem.* **128**, 38-41. (doi:10.1006/jssc.1996.7144).

61. Le Bihan, S. & Figlarz, M. 1972 Croissance de l'Hydroxyde de Nickel $Ni(OH)_2$ à Partir d'un Hydroxyde de Nickel Turbostratique. *J. Cryst. Growth* **13/14**, 458-461. (doi:10.1016/0022-0248(72)90280-1).

62. Minkova, N., Krusteva, M. & Nikolov, G. 1984 Spectroscopic study of nickel hydroxyde, nickel carbonate-hexahydrate and nickel hydroxocarbonate. *J. Mol. Struct.* **115**, 23-26. (doi:10.1016/0022-2860(84)80006-x).

63. Portemer, F., Delahaye-Vidal, A. & Figlarz, M. 1992 Characterization of active material deposited at the nickel hydroxide electrode by electrochemical impregnation. *J. Electrochem. Soc.* **139**, 671-678. (doi:10.1149/1.2069283).

64. Rajamathi, M. & Kamath, P.V. 1998 On the Relationship Between α-Nickel Hydroxide and the Basic Salts of Nickel. *J. Power Sources* **70**, 118-121. (doi:10.1016/S0378-7753(97)02656-6).

65. Weckler, B. & Lutz, H.D. 1996 Near-infrared spectra of M(OH)Cl (M = Ca, Cd, Sr), Zn(OH)F, γ-$Cd(OH)_2$, $Sr(OH)_2$, and brucite-type hydroxides $M(OH)_2$ (M = Mg, Ca, Mn, Fe, Co, Ni, Cd). *Spectrochim. Acta, Part A* **52**, 1507-1513. (doi:10.1016/0584-8539(96)01693-5).

66. Audemer, A., Delahaye, A., Farhi, R., Sac-Epée, N. & Tarascon, J.-M. 1997 Electrochemical and Raman Studies of Beta-Type Nickel Hydroxides $Ni_{1-x}Co_x(OH)_2$ Electrode Materials. *J. Electrochem. Soc.* **144**, 2614-2620. (doi:10.1149/1.1837873).

67. Bernard, M.C., Cortes, R., Keddam, M., Takenouti, H., Bernard, P. & Senyarich, S. 1996 Structural Defects and Electrochemical Reactivity of β-$Ni(OH)_2$. *J. Power Sources* **63**, 247-254. (doi:10.1016/s0378-7753(96)02482-2).

68. Bernard, M.C., Bernard, P., Keddam, M., Senyarich, S. & Takenouti, H. 1996 Characterisation of new nickel hydroxides during the transformation of α $Ni(OH)_2$ to β $Ni(OH)_2$ by ageing. *Electrochim. Acta* **41**, 91-93. (doi:10.1016/0013-4686(95)00282-J).

69. Cornilsen, B.C., Karjala, P.J. & Loyselle, P.L. 1988 Structural models for nickel electrode active mass. *J. Power Sources* **22**, 351-357. (doi:10.1016/0378-7753(88)80029-6).

70. Cornilsen, B.C., Shan, X. & Loyselle, P.L. 1990 Structural comparison of nickel electrodes and precursor phases. *J. Power Sources* **29**, 453-466. (doi:10.1016/0378-7753(90)85018-8).

71. Desilvestro, J., Corrigan, D.A. & Weaver, M.J. 1988 Characterization of Redox States of Nickel Hydroxide Film Electrodes by In Situ Surface Raman Spectroscopy. *J. Electrochem. Soc.* **135**, 885-892. (doi:10.1149/1.2095818).

72. Johnston, C. & Graves, P.R. 1990 In Situ Raman Spectroscopy Study of the Nickel Oxyhydroxide Electrode (NOE) System. *Appl. Spectrosc.* **44**, 105-115. (doi:10.1366/0003702904085769).

73. Kostecki, R. & McLarnon, F. 1997 Electrochemical and In Situ Raman Spectroscopic Characterization of Nickel Hydroxide Electrodes. *J. Electrochem. Soc.* **144**, 485-493. (doi:10.1149/1.1837437).

74. Liu, C. & Li, Y. 2009 Synthesis and characterization of amorphous α-nickel hydroxide. *J. Alloys Compd.* **478**, 415-418. (doi:10.1016/j.jallcom.2008.11.049).

75. Murli, C., Sharma, S.M., Kulshreshtha, S.K. & Sikka, S.K. 2001 High-pressure behavior of β-Ni (OH)2—A Raman scattering study. *Physica B* **307**, 111-116. (doi:10.1016/s0921-4526(01)00646-9).

76. Nan, J., Yang, Y. & Lin, Z. 2006 In situ photoelectrochemistry and Raman spectroscopic characterization on the surface oxide film of nickel electrode in 30 wt.% KOH solution. *Electrochim. Acta* **51**, 4873-4879. (doi:10.1016/j.electacta.2006.01.031).

77. Bantignies, J.L., Deabate, S., Righi, A., Rols, S., Hermet, P., Sauvajol, J.L. & Henn, F. 2008 New Insight into the Vibrational Behavior of Nickel Hydroxide and Oxyhydroxide

Using Inelastic Neutron Scattering, Far/Mid-Infrared and Raman Spectroscopies. *J. Phys. Chem. C* **112**, 2193-2201. (doi:10.1021/jp075819e).

78. Bardé, F., Palacin, M.R., Chabre, Y., Isnard, O. & Tarascon, J.M. 2004 In Situ Neutron Powder Diffraction of a Nickel Hydroxide Electrode. *Chem. Mater.* **16**, 3936-3948. (doi:10.1021/cm0401286).

79. Braconnier, J.J., Delmas, C., Fouassier, C., Figlarz, M., Beaudouin, B. & Hagenmuller, P. 1984 A Novel Nickel(II) Hydroxide Hydrate Obtained by Soft Chemistry. *Rev. Chim. Miner.* **21**, 496-508.

80. Barnard, R., Randell, C.F. & Tye, F.L. 1980 Studies concerning charged nickel hydroxide electrodes. I. Measurement of reversible potentials. *J. Appl. Electrochem.* **10**, 109-125. (doi:10.1007/BF00937345).

81. Rajamathi, M., Vishnu Kamath, P. & Seshadri, R. 2000 Polymorphism in nickel hydroxide: role of interstratification. *J. Mater. Chem.* **10**, 503-506. (doi:10.1039/a905651c).

82. Linden, D. 1995 *Handbook of Batteries*. New York: Mc-Graw-Hill. p.

83. Delmas, C. & Tessier, C. 1997 Stacking faults in the structure of nickel hydroxide: a rationale of its high electrochemical activity. *J. Mater. Chem.* **7**, 1439-1443. (doi:10.1039/a701037k).

84. Kober, F.P. 1967 On the structure of electrochemically active hydrated nickel-oxide electrodes. In *Power Sources: Proceedings for the 5th International Power Sources Symposium* (ed. D.H. Collins), pp. 257-268. Brighton, Academic Press, London.

85. Dennstedt, W. & Löser, W. 1971 Zur kenntnis der nickelhydroxid-elektrode—III. Thermogravimetrische untersuchungen an Nickel(II)-hydroxiden. *Electrochim. Acta* **16**, 429-435. (doi:10.1016/0013-4686(71)85015-6).

86. Mani, B. & de Neufville, J.P. 1988 Dehydration of Chemically and Electrochemically Impregnated (CI and EI) Nickel Hydroxide Electrodes. *J. Electrochem. Soc.* **135**, 800-803. (doi:10.1149/1.2095777).

87. Hall, D.S., Lockwood, D.J., Poirier, S., Bock, C. & MacDougall, B.R. 2012 Raman and Infrared Spectroscopy of α and β Phases of Thin Nickel Hydroxide Films Electrochemically Formed on Nickel. *J. Phys. Chem. A* **116**, 6771-6784. (doi:10.1021/jp303546r).

88. Radha, A.V., Kamath, P.V. & Shivakumara, C. 2007 Order and disorder among the layered double hydroxides: combined Rietveld and DIFFaX approach. *Acta Crystallographica Section B* **63**, 243-250. (doi:10.1107/S010876810700122X).

89. Tessier, C., Haumesser, P.H., Bernard, P. & Delmas, C. 1999 The Structure of $Ni(OH)_2$: From the Ideal Material to the Electrochemically Active One. *J. Electrochem. Soc.* **146**, 2059-2067. (doi:10.1149/1.1391892).

90. Sebastian, M.T. & Krishna, P. 1994 *Random, Non-Random, and Periodic Faulting in Crystals*. Langhorne, PA, USA: Gordon and Breach Science Publishers; 383 p.

91. Zhang, W., Jiang, W., Yu, L., Fu, Z., Xia, W. & Yang, M. 2009 Effect of nickel hydroxide composition on the electrochemical performance of spherical $Ni(OH)_2$ positive materials for Ni–MH batteries. *Int. J. Hydrogen Energy* **34**, 473-480. (doi:10.1016/j.ijhydene.2008.07.129).

92. Huang, J., Lei, T., Wei, X., Liu, X., Liu, T., Cao, D., Yin, J. & Wang, G. 2013 Effect of Al-doped β-$Ni(OH)_2$ nanosheets on electrochemical behaviors for high performance supercapacitor application. *J. Power Sources* **232**, 370-375. (doi:10.1016/j.jpowsour.2013.01.081).

93. Begum, S.N., Muralidharan, V.S. & Ahmed Basha, C. 2009 The influences of some additives on electrochemical behaviour of nickel electrodes. *Int. J. Hydrogen Energy* **34**, 1548-1555. (doi:10.1016/j.ijhydene.2008.11.074).

94. Watanabe, K., Koseki, M. & Kumagai, N. 1996 Effect of cobalt addition to nickel hydroxide as a positive material for rechargeable alkaline batteries. *J. Power Sources* **58**, 23-28. (doi:10.1016/0378-7753(95)02272-4).

95. Watanabe, K. & Kumagai, N. 1998 Thermodynamic studies of cobalt and cadmium additions to nickel hydroxide as material for positive electrodes. *J. Power Sources* **76**, 167-174. (doi:10.1016/S0378-7753(98)00150-5).

96. Chen, H., Wang, J.M., Zhao, Y.L., Zhang, J.Q. & Cao, C.N. 2005 Electrochemical performance of Zn-substituted Ni(OH)2 for alkaline rechargeable batteries. *J. Solid State Electrochem.* **9**, 421-428. (doi:10.1007/s10008-004-0578-x).

97. Hu, B., Chen, S.-F., Liu, S.-J., Wu, Q.-S., Yao, W.-T. & Yu, S.-H. 2008 Controllable Synthesis of Zinc-Substituted α- and β-Nickel Hydroxide Nanostructures and Their Collective Intrinsic Properties. *Chem.–Eur. J.* **14**, 8928-8938. (doi:10.1002/chem.200800458).

98. Bao, J., Zhu, Y., Xu, Q.S., Zhuang, Y.H., Zhao, R.D., Zeng, Y.Y. & Zhong, H.L. 2012 Structure and Electrochemical Performance of Cu and Al Codoped Nanometer α-Nickel

Hydroxide. *Adv. Mater. Res.* **479**, 230-233. (doi:10.4028/www.scientific.net/AMR.479-481.230).

99. Chen, H., Wang, J.M., Pan, T., Zhao, Y.L., Zhang, J.Q. & Cao, C.N. 2005 The structure and electrochemical performance of spherical Al-substituted α-$Ni(OH)_2$ for alkaline rechargeable batteries. *J. Power Sources* **143**, 243-255. (doi:10.1016/j.jpowsour.2004.11.041).

100. Jayashree, R.S. & Vishnu Kamath, P. 2001 Suppression of the α → β-nickel hydroxide transformation in concentrated alkali: Role of dissolved cations. *J. Appl. Electrochem.* **31**, 1315-1320. (doi:10.1023/a:1013876006707).

101. Li, Y.W., Yao, J.H., Liu, C.J., Zhao, W.M., Deng, W.X. & Zhong, S.K. 2010 Effect of interlayer anions on the electrochemical performance of Al-substituted α-type nickel hydroxide electrodes. *Int. J. Hydrogen Energy* **35**, 2539-2545. (doi:10.1016/j.ijhydene.2010.01.015).

102. Qi, J., Xu, P., Lv, Z., Liu, X. & Wen, A. 2008 Effect of crystallinity on the electrochemical performance of nanometer Al-stabilized α-nickel hydroxide. *J. Alloys Compd.* **462**, 164-169. (doi:10.1016/j.jallcom.2007.07.102).

103. Wang, C.Y., Zhong, S., Bradhurst, D.H., Liu, H.K. & Dou, S.X. 2002 Ni/Al/Co-substituted α-$Ni(OH)_2$ as electrode materials in the nickel metal hydride cell. *J. Alloys Compd.* **330–332**, 802-805. (doi:10.1016/S0925-8388(01)01515-8).

104. Zhao, Y.L., Wang, J.M., Chen, H., Pan, T., Zhang, J.Q. & Cao, C.N. 2004 Different additives-substituted α-nickel hydroxide prepared by urea decomposition. *Electrochim. Acta* **50**, 91-98. (doi:10.1016/j.electacta.2004.07.016).

105. Guerlou-Demourgues, L. & Delmas, C. 1996 Electrochemical Behavior of the Manganese-Substituted Nickel Hydroxides. *J. Electrochem. Soc.* **143**, 561-566. (doi:10.1149/1.1836480).

106. Demourgues-Guerlou, L. & Delmas, C. 1993 Structure and properties of precipitated nickel-iron hydroxides. *J. Power Sources* **45**, 281-289. (doi:10.1016/0378-7753(93)80017-J).

107. Liu, C., Huang, L., Li, Y. & Sun, D. 2010 Synthesis and electrochemical performance of amorphous nickel hydroxide codoped with Fe^{3+} and CO_3^{2-}. *Ionics* **16**, 215-219. (doi:10.1007/s11581-009-0383-8).

108. Chen, J.-C., Hsu, C.-T. & Hu, C.-C. 2014 Superior capacitive performances of binary nickel–cobalt hydroxide nanonetwork prepared by cathodic deposition. *J. Power Sources* **253**, 205-213. (doi:10.1016/j.jpowsour.2013.12.073).

109. Delmas, C., Braconnier, J.J., Borthomieu, Y. & Hagenmuller, P. 1987 New families of cobalt substituted nickel oxyhydroxides and hydroxides obtained by soft chemistry. *Mater. Res. Bull.* **22**, 741-751. (doi:10.1016/0025-5408(87)90027-4).

110. Nethravathi, C., Ravishankar, N., Shivakumara, C. & Rajamathi, M. 2007 Nanocomposites of α-hydroxides of nickel and cobalt by delamination and co-stacking: Enhanced stability of α-motifs in alkaline medium and electrochemical behaviour. *J. Power Sources* **172**, 970-974. (doi:10.1016/j.jpowsour.2007.01.098).

111. Bao, J., Zhu, Y., Zhang, Z., Xu, Q., Zhao, W., Chen, J., Zhang, W. & Han, Q. 2013 Structure and electrochemical properties of nanometer Cu substituted α-nickel hydroxide. *Mater. Res. Bull.* **48**, 422-428. (doi:10.1016/j.materresbull.2012.10.059).

112. Dixit, M., Kamath, P.V. & Gopalakrishnan, J. 1999 Zinc-Substituted α-Nickel Hydroxide as an Electrode Material for Alkaline Secondary Cells. *J. Electrochem. Soc.* **146**, 79-82. (doi:10.1149/1.1391567).

113. Tessier, C., Guerlou-Demourgues, L., Faure, C., Basterreix, M.t., Nabias, G. & Delmas, C. 2000 Structural and textural evolution of zinc-substituted nickel hydroxide electrode materials upon ageing in KOH and upon redox cycling. *Solid State Ionics* **133**, 11-23. (doi:10.1016/S0167-2738(00)00690-1).

114. Ren, J., Zhou, Z., Gao, X.P. & Yan, J. 2006 Preparation of porous spherical α-$Ni(OH)_2$ and enhancement of high-temperature electrochemical performances through yttrium addition. *Electrochim. Acta* **52**, 1120-1126. (doi:10.1016/j.electacta.2006.07.028).

115. Xu, Q., Zhu, Y., Han, Q., Zhao, R., Zhuang, Y., Liu, Y., Zhang, S. & Miao, C. 2014 Preparation of Yb-substituted α-$Ni(OH)_2$ and its physicochemical properties. *J. Alloys Compd.* **584**, 1-6. (doi:10.1016/j.jallcom.2013.08.097).

116. Hall, D.S., Lockwood, D.J., Poirier, S., Bock, C. & MacDougall, B.R. 2014 Applications of in Situ Raman Spectroscopy for Identifying Nickel Hydroxide Materials and Surface Layers during Chemical Aging. *ACS Appl. Mater. Interfaces* **6**, 3141-3149. (doi:10.1021/am405419k).

117. Streinz, C.C., Hartman, A.P., Motupally, S. & Weidner, J.W. 1995 The Effect of Current and Nickel Nitrate Concentration on the Deposition of Nickel Hydroxide Films. *J. Electrochem. Soc.* **142**, 1084-1089. (doi:10.1149/1.2044134).

118. Lee, J.W., Ko, J.M. & Kim, J.-D. 2011 Hierarchical Microspheres Based on α-$Ni(OH)_2$ Nanosheets Intercalated with Different Anions: Synthesis, Anion Exchange, and Effect of

Intercalated Anions on Electrochemical Capacitance. *The Journal of Physical Chemistry C* **115**, 19445-19454. (doi:10.1021/jp206379h).

119. Xu, L., Ding, Y.-S., Chen, C.-H., Zhao, L., Rimkus, C., Joesten, R. & Suib, S.L. 2007 3D Flowerlike α-Nickel Hydroxide with Enhanced Electrochemical Activity Synthesized by Microwave-Assisted Hydrothermal Method. *Chem. Mater.* **20**, 308-316. (doi:10.1021/cm702207w).

120. Alberti, G. & Bein, T. 1996 Layered Solids and Their Intercalation Chemistry. In *Solid-state Supramolecular Chemistry: Two- and Three-dimensional Inorganic Networks* (eds. G. Alberti & T. Bein), pp. 1-23. New York, Pergamon Press.

121. Zhu, W.-H., Ke, J.-J., Yu, H.-M. & Zhang, D.-J. 1995 A study of the electrochemistry of nickel hydroxide electrodes with various additives. *J. Power Sources* **56**, 75-79. (doi:10.1016/0378-7753(95)80011-5).

122. Rajamathi, M., N. Subbanna, G. & Vishnu Kamath, P. 1997 On the existence of a nickel hydroxide phase which is neither α nor β. *J. Mater. Chem.* **7**, 2293-2296. (doi:10.1039/a700390k).

123. Häring, P. & Kötz, R. 1995 Nanoscale thickness changes of nickel hydroxide films during electrochemical oxidation/reduction monitored by in situ atomic force microscopy. *J. Electroanal. Chem.* **385**, 273-277. (doi:10.1016/0022-0728(94)03869-5).

124. Subbaiah, T., Mallick, S.C., Mishra, K.G., Sanjay, K. & Das, R.P. 2002 Electrochemical precipitation of nickel hydroxide. *J. Power Sources* **112**, 562-569. (doi:10.1016/S0378-7753(02)00470-6).

125. Šurca, A., Orel, B., Pihlar, B. & Bukovec, P. 1996 Optical, spectroelectrochemical and structural properties of sol-gel derived Ni-oxide electrochromic film. *J. Electroanal. Chem.* **408**, 83-100. (doi:10.1016/0022-0728(96)04509-3).

126. Martins, P.R., Araújo Parussulo, A.L., Toma, S.H., Rocha, M.A., Toma, H.E. & Araki, K. 2012 Highly stabilized alpha-$NiCo(OH)_2$ nanomaterials for high performance device application. *J. Power Sources* **218**, 1-4. (doi:10.1016/j.jpowsour.2012.06.065).

127. Cheng, J., Cao, G.-P. & Yang, Y.-S. 2006 Characterization of sol–gel-derived NiO_x xerogels as supercapacitors. *J. Power Sources* **159**, 734-741. (doi:10.1016/j.jpowsour.2005.07.095).

128. Liu, X.H., Liu, W., Lv, X.K., Yang, F., Wei, X., Zhang, Z.D. & Sellmyer, D.J. 2010 Magnetic properties of nickel hydroxide nanoparticles. *J. Appl. Phys.* **107**, 083919. (doi:10.1063/1.3374468).

129. Soler-Illia, G.J.d.A.A., Jobbágy, M., Regazzoni, A.E. & Blesa, M.A. 1999 Synthesis of Nickel Hydroxide by Homogeneous Alkalinization. Precipitation Mechanism. *Chem. Mater.* **11**, 3140-3146. (doi:10.1021/cm9902220).

130. Zhu, Z., Wei, N., Liu, H. & He, Z. 2011 Microwave-assisted hydrothermal synthesis of $Ni(OH)_2$ architectures and their in situ thermal convention to NiO. *Advanced Powder Technology* **22**, 422-426. (doi:10.1016/j.apt.2010.06.008).

131. Machado, S.A.S. & Avaca, L.A. 1994 The hydrogen evolution reaction on nickel surfaces stabilized by H-absorption. *Electrochim. Acta* **39**, 1385-1391. (doi:10.1016/0013-4686(94)e0003-i).

132. Juškėnas, R., Selskis, A. & Kadziauskienė, V. 1998 In situ X-ray diffraction investigation of nickel hydride formation during cathodic charging of Ni. *Electrochim. Acta* **43**, 1903-1911. (doi:10.1016/s0013-4686(97)00304-6).

133. Baranowski, B. 1999 Electrochemical formation of nickel hydride in alkaline solutions. *J. Electroanal. Chem.* **472**, 182-184. (doi:10.1016/S0022-0728(99)00297-1).

134. Baranowski, B. & Filipek, S.M. 2005 45 Years of nickel hydride—History and perspectives. *J. Alloys Compd.* **404–406**, 2-6. (doi:10.1016/j.jallcom.2005.02.102).

135. Bernardini, M., Comisso, N., Davolio, G. & Mengoli, G. 1992 Formation of nickel hydrides by hydrogen evolution in alkaline media. *J. Electroanal. Chem.* **442**, 125-135. (doi:10.1016/S0022-0728(97)00492-0).

136. Bernardini, M., Comisso, N., Mengoli, G. & Sinico, L. 1998 Formation of nickel hydrides by hydrogen evolution in alkaline media: effect of temperature. *J. Electroanal. Chem.* **457**, 205-219. (doi:10.1016/s0022-0728(98)00307-6).

137. Conway, B.E., Angerstein-Kozlowska, H., Sattar, M.A. & Tilak, B.V. 1983 Study of a Decomposing Hydride Phase at Nickel Cathodes by Measurement of Open-Circuit Potential Decay. *J. Electrochem. Soc.* **130**, 1825-1836. (doi:10.1149/1.2120106).

138. Hitz, C. & Lasia, A. 2001 Experimental study and modeling of impedance of the her on porous Ni electrodes. *J. Electroanal. Chem.* **500**, 213-222. (doi:10.1016/S0022-0728(00)00317-X).

139. Hitz, C. & Lasia, A. 2002 Determination of the kinetics of the hydrogen evolution reaction by the galvanostatic step technique. *J. Electroanal. Chem.* **532**, 133-140. (doi:10.1016/s0022-0728(02)00760-x).

140. Jaksic, M., Brun, J., Johansen, B. & Tunold, R. 1995 The Rowland or EDTA effect on electrochemical behavior of transition metals and in electrocatalysis for the hydrogen evolution reaction. The Rowland effect on some non-noble non-valve transition metals. *Russ. J. Electrochem.* **31**, 1187-1202.

141. Gileadi, E. 1993 *Electrode kinetics for chemists, chemical engineers, and materials scientists*. New York: VCH; 597 p.

142. Flanagan, T.B. & Lewis, F.A. 1959 Hydrogen absorption by palladium in aqueous solution. *Trans. Faraday Soc.* **55**, 1400-1408. (doi:10.1039/TF9595501400).

143. Wollan, E.O., Cable, J.W. & Koehler, W.C. 1963 The hydrogen atom positions in face centered cubic nickel hydride. *J. Phys. Chem. Solids* **24**, 1141-1143. (doi:10.1016/0022-3697(63)90028-3).

144. Szklarska-Smialowska, Z. & Smialowski, M. 1958 Creation of stresses in nickel cathodes due to hydrogenation. *Bull. Acad. Pol. Sci., Ser. Sci. Chim.* **6**, 427-432.

145. Baranowski, B., Majchrzak, S. & Flanagan, T.B. 1971 The volume increase of fcc metals and alloys due to interstitial hydrogen over a wide range of hydrogen contents. *Journal of Physics F: Metal Physics* **1**, 258-261. (doi:10.1088/0305-4608/1/3/307).

146. Boniszewski, T. & Smith, G.C. 1961 A note on nickel hydride. *J. Phys. Chem. Solids* **21**, 115-118. (doi:10.1016/0022-3697(61)90219-0).

147. Trasatti, S. & Petrii, O.A. 1992 Real surface area measurements in electrochemistry. *J. Electroanal. Chem.* **327**, 353-376. (doi:10.1016/0022-0728(92)80162-W).

148. Manandhar, K. & Pletcher, D. 1979 The preparation of high surface area nickel oxide electrodes for synthesis. *J. Appl. Electrochem.* **9**, 707-713. (doi:10.1007/bf00614964).

149. Alsabet, M., Grden, M. & Jerkiewicz, G. 2011 Electrochemical Growth of Surface Oxides on Nickel. Part 1: Formation of α-$Ni(OH)_2$ in Relation to the Polarization Potential, Polarization Time, and Temperature. *Electrocatalysis* **2**, 317-330. (doi:10.1007/s12678-011-0067-9).

150. Bai, L., Harrington, D.A. & Conway, B.E. 1987 Behavior of overpotential-deposited species in faradaic reactions-II. ac Impedance measurements on H2 evolution kinetics at activated and unactivated Pt cathodes. *Electrochim. Acta* **32**, 1713-1731. (doi:10.1016/0013-4686(87)80006-3).

151. Lasia, A. & Rami, A. 1990 Kinetics of hydrogen evolution on nickel electrodes. *J. Electroanal. Chem. Interfacial Electrochem.* **294**, 123-141. (doi:10.1016/0022-0728(90)87140-f).

152. Lyons, M.E.G. & Brandon, M.P. 2008 The Oxygen Evolution Reaction on Passive Oxide Covered Transition Metal Electrodes in Aqueous Alkaline Solution. Part 1-Nickel. *Int. J. Electrochem. Sci.* **3**, 1386-1424.

153. Shervedani, R.K. & Lasia, A. 1999 Evaluation of the surface roughness of microporous Ni–Zn–P electrodes by in situ methods. *J. Appl. Electrochem.* **29**, 979-986. (doi:10.1023/A:1003577631897).

154. Chen, L. & Lasia, A. 1991 Study of the kinetics of hydrogen evolution reaction on nickel-zinc alloy electrodes. *J. Electrochem. Soc.* **138**, 3321-3328. (doi:10.1149/1.2085409).

155. Bockris, J.O.M. & Otagawa, T. 1984 The Electrocatalysis of Oxygen Evolution on Perovskites. *J. Electrochem. Soc.* **131**, 290-302. (doi:10.1149/1.2115565).

156. Ho, J.C.K. & Piron, D.L. 1996 Active surface area in oxide electrodes by overpotential deposited oxygen species for the oxygen evolution reaction. *J. Appl. Electrochem.* **26**, 515-521. (doi:10.1007/bf01021975).

157. Huang, V.M.-W., Vivier, V., Orazem, M.E., Pebere, N. & Tribollet, B. 2007 The Apparent Constant-Phase-Element Behavior of an Ideally Polarized Blocking Electrode. *J. Electrochem. Soc.* **154**, C81-C88. (doi:10.1149/1.2398882).

158. Brug, G.J., van den Eeden, A.L.G., Sluyters-Rehbach, M. & Sluyters, J.H. 1984 The analysis of electrode impedances complicated by the presence of a constant phase element. *J. Electroanal. Chem. Interfacial Electrochem.* **176**, 275-295. (doi:10.1016/s0022-0728(84)80324-1).

159. Biesinger, M.C., Payne, B.P., Lau, L.W.M., Gerson, A. & Smart, R.S.C. 2009 X-ray photoelectron spectroscopic chemical state quantification of mixed nickel metal, oxide and hydroxide systems. *Surf. Interface Anal.* **41**, 324-332. (doi:10.1002/sia.3026).

160. Lockwood, D.J., Cottam, M.G. & Baskey, J.H. 1992 One- and two-magnon excitations in NiO. *J. Magn. Magn. Mater.* **104-107, Part 2**, 1053-1054. (doi:10.1016/0304-8853(92)90486-8).

161. Pascale, F., Tosoni, S., Zicovich-Wilson, C., Ugliengo, P., Orlando, R. & Dovesi, R. 2004 Vibrational spectrum of brucite, $Mg(OH)_2$: a periodic ab initio quantum mechanical calculation including OH anharmonicity. *Chem. Phys. Lett.* **396**, 308-315. (doi:10.1016/j.cplett.2004.08.047).

162. Dawson, P., Hadfield, C.D. & Wilkinson, G.R. 1973 The polarized infra-red and Raman spectra of Mg(OH)2 and Ca(OH)2. *J. Phys. Chem. Solids* **34**, 1217-1225. (doi:10.1016/s0022-3697(73)80212-4).

163. de Oliveira, E.F. & Hase, Y. 2001 Infrared study and isotopic effect of magnesium hydroxide. *Vib. Spectrosc.* **25**, 53-56. (doi:10.1016/s0924-2031(00)00107-7).

164. Herzberg, G. & Spinks, J. 1966 *Molecular Spectra and Molecular Structure: II. Infrared and Raman Spectra of Polyatomic Molecules*. 6th ed. Toronto, Canada: D. Van Nostrand Company, Inc.

165. Riddell, J.D., Lockwood, D.J. & Irish, D.E. 1972 Ion Pair Formation in NaNO3/D2O Solutions: Raman and Infrared Spectra, Partial Molal Volumes, Conductance, and Viscosity. *Can. J. Chem.* **50**, 2951-2962. (doi:10.1139/v72-474).

166. Ikeda, K. & Vedanand, S. 1999 Optical Spectrum of Synthetic Theophrastite, $Ni(OH)_2$. *Neues Jahrb. Mineral., Monatsh.*, 21-26.

167. Laporte, O. & Meggers, W.F. 1925 Some rules of spectral structure. *J. Opt. Soc. Am.* **11**, 459-460. (doi:10.1364/JOSA.11.000459).

168. Deabate, S., Fourgeot, F. & Henn, F. 2000 X-ray diffraction and micro-Raman spectroscopy analysis of new nickel hydroxide obtained by electrodialysis. *J. Power Sources* **87**, 125-136. (doi:10.1016/S0378-7753(99)00437-1).

169. Deabate, S., Fourgeot, F. & Henn, F. 2006 Electrochemical behaviour of the β(II)-Ni(OH)2/β(III)-NiOOH redox couple upon potentiodynamic cycling conditions. *Electrochim. Acta* **51**, 5430-5437. (doi:10.1016/j.electacta.2006.02.012).

170. Desilvestro, J., Corrigan, D.A. & Weaver, M.J. 1986 Spectroelectrochemistry of Thin Nickel Hydroxide Films on Gold Using Surface-Enhanced Raman Spectroscopy. *J. Phys. Chem.* **90**, 6408-6411. (doi:10.1021/j100282a002).

171. Osińska, M., Stefanowicz, T. & Paukszta, D. 2004 Nickel Hydroxide Ageing Time Influence on its Solubility in Water Acidified With Sulphuric Acid. *J. Hazard. Mater.* **112**, 177-182. (doi:10.1016/j.jhazmat.2004.05.028).

172. Godwin, I.J. & Lyons, M.E.G. 2013 Enhanced Oxygen Evolution at Hydrous Nickel Oxide Electrodes Via Electrochemical Ageing in Alkaline Solution. *Electrochem. Commun.* **32**, 39-42. (doi:10.1016/j.elecom.2013.03.040).

173. Hall, D.S., Bock, C. & MacDougall, B.R. 2013 Surface Layers in Alkaline Media: Nickel Hydrides on Metallic Nickel Electrodes. *ECS Trans.* **50**, 165-179. (doi:10.1149/05031.0165ecst).

174. Beden, B., Floner, D., Leger, J.M. & Lamy, C. 1985 A voltammetric study of the formation on hydroxides and oxyhydroxides on nickel single crystal electrodes in contact with an alkaline solution. *Surf. Sci.* **162**, 822-829. (doi:10.1016/0039-6028(85)90985-9).

175. Burke, L.D. & Twomey, T.A.M. 1982 Influence of pH on the redox behaviour of hydrous nickel oxide. *J. Electroanal. Chem. Interfacial Electrochem.* **134**, 353-362. (doi:10.1016/0022-0728(82)80013-2).

176. Burke, L.D. & Twomey, T.A.M. 1984 Voltammetric behaviour of nickel in base with particular reference to thick oxide growth. *J. Electroanal. Chem. Interfacial Electrochem.* **162**, 101-119. (doi:10.1016/S0022-0728(84)80158-8).

177. Seghiouer, A., Chevalet, J., Barhoun, A. & Lantelme, F. 1998 Electrochemical oxidation of nickel in alkaline solutions: A voltammetric study and modelling. *J. Electroanal. Chem.* **442**, 113-123. (doi:10.1016/S0022-0728(97)00498-1).

178. Visscher, W. & Barendrecht, E. 1980 The Anodic Oxidation of Nickel in Alkaline Solution. *Electrochim. Acta* **25**, 651-655. (doi:10.1016/0013-4686(80)87072-1).

179. Huang, V.M.-W., Vivier, V., Orazem, M.E., Pebere, N. & Tribollet, B. 2007 The Apparent Constant-Phase-Element Behavior of a Disk Electrode with Faradaic Reactions. *J. Electrochem. Soc.* **154**, C99-C107. (doi:10.1149/1.2398894).

180. Szklarska-Smialowska, Z. & Smialowski, M. 1963 Electrochemical Study of the Nickel-Hydrogen System. *J. Electrochem. Soc.* **110**, 444-448. (doi:10.1149/1.2425783).

181. Bard, A., Parsons, R. & Jordan, J. 1985 *Standard Potentials in Aqueous Solution*. New York, New York: International Union of Pure and Applied Chemistry.

182. Rossini, F.D., Wagman, D.D., Evans, W.H., Levine, S. & Jaffe, I. 1952 *Selected Values of Chemical Thermodynamic Properties*: National Bureau of Standards.

183. Boyle, B.J., King, E.G. & Conway, K.C. 1954 Heats of Formation of Nickel and Cobalt Oxides (NiO and CoO) of Combustion Calorimetry. *J. Am. Chem. Soc.* **76**, 3835-3837. (doi:10.1021/ja01643a072).

184. Engel, T. & Reid, P. 2006 *Thermodynamics, Statistical Thermodynamics, & Kinetics*. Toronto: Benjamin Cummings.

185. Vuković, M. 1994 Voltammetry and anodic stability of a hydrous oxide film on a nickel electrode in alkaline solution. *J. Appl. Electrochem.* **24**, 878-882. (doi:10.1007/bf00348775).

186. Abouatallah, R.M., Kirk, D.W. & Graydon, J.W. 2002 Long-term electrolytic hydrogen permeatin in nickel and the effect of vanadium species addition. *Electrochim. Acta* **47**, 2483-2494. (doi:10.1016/S0013-4686(02)00108-1).

187. Grdeń, M. & Klimek, K. 2005 EQCM studies on oxidation of metallic nickel electrode in basic solutions. *J. Electroanal. Chem.* **581**, 122-131. (doi:10.1016/j.jelechem.2005.04.026).

188. Zemaitis, J.F.J., Clark, D.M., Rafal, M. & Scrivner, N.C. 1986 *Handbook of aqueous electrolyte thermodynamics: Theory & application*. New York: Design Institute for Physical Property Data; 852 p.

189. Devanathan, M.A.V. & Stachurski, Z. 1962 The adsorption and diffusion of electrolytic hydrogen in palladium. *Proc. R. Soc. Lond. A* **270**, 90-102. (doi:10.1098/rspa.1962.0205).

190. Gileadi, E., Kirowa-Eisner, E. & Penciner, J. 1975 Absorption of hydrogen in palladium and diffusion through it. In *Interfacial Electrochemistry: An Experimental Approach* (pp. 472-484. Don Mills, Ontario, Addison-Wesley Publishing Company, Inc.

191. Williamson, G.K. & Hall, W.H. 1953 X-ray line broadening from filed aluminium and wolfram. *Acta Metallurgica* **1**, 22-31. (doi:10.1016/0001-6160(53)90006-6).

192. Louthan Jr, M.R., Donovan, J.A. & Caskey Jr, G.R. 1975 Hydrogen diffusion and trapping in nickel. *Acta Metallurgica* **23**, 745-749. (doi:10.1016/0001-6160(75)90057-7).

193. MacDougall, B., Mitchell, D.F. & Graham, M.J. 1980 Galvanostatic Oxidation of Nickel in Borate Buffer Solution. *J. Electrochem. Soc.* **127**, 1248-1252. (doi:10.1149/1.2129864).

194. Sikora, E. & Macdonald, D.D. 2002 Nature of the passive film on nickel. *Electrochim. Acta* **48**, 69-77. (doi:10.1016/s0013-4686(02)00552-2).

195. Grdeń, M., Klimek, K. & Czerwinski, A. 2004 A quartz crystal microbalance study on a metallic nickel electrode. *J. Solid State Electrochem.* **8**, 390-397. (doi:10.1007/s10008-003-0461-1).

196. Hahn, F., Beden, B., Croissant, M.J. & Lamy, C. 1986 *In situ uv* visible reflectance spectroscopic investigation of the nickel electrode-alkaline solution interface. *Electrochim. Acta* **31**, 335-342. (doi:10.1016/0013-4686(86)80087-1).

197. Grosvenor, A.P., Biesinger, M.C., Smart, R.S.C. & McIntyre, N.S. 2006 New interpretations of XPS spectra of nickel metal and oxides. *Surf. Sci.* **600**, 1771-1779. (doi:10.1016/j.susc.2006.01.041).

198. Kibria, M.F., Mridha, M.S. & Khan, A.H. 1995 Electrochemical studies of a nickel electrode for the hydrogen evolution reaction. *Int. J. Hydrogen Energy* **20**, 435-440. (doi:10.1016/0360-3199(94)00073-9).

199. Hall, D.S., Bock, C. & MacDougall, B.R. 2014 An oxalate method for measuring the surface area of nickel electrodes. *J. Electrochem. Soc.* **161**, H787-H795. (doi:10.1149/2.0711412jes).

200. Gladisheva, T., Podlovchenko, B. & Zikrina, Z. 1987 Preparation and Properties of Highly-Dispersed Electrolytic Rhodium Deposits on a Carbon Substrate. *Elektrokhimiya* **23**, 1446-1448.

201. Quiroz, M.A., Meas, Y., Lamy-Pitara, E. & Barbier, J. 1983 Characterization of a ruthenium electrode by underpotential deposition of copper. *J. Electroanal. Chem. Interfacial Electrochem.* **157**, 165-174. (doi:10.1016/S0022-0728(83)80387-8).

202. Siegenthaler, H. & Jüttner, K. 1984 Voltammetric investigation of lead adsorption on Cu(111) single crystal substrates. *J. Electroanal. Chem. Interfacial Electrochem.* **163**, 327-343. (doi:10.1016/S0022-0728(84)80060-1).

203. Vashkyalis, A. & Demontaite, O. 1978 Determination of the Value of the Surface Area of Silver by Electrochemical Precipitation of a Lead Monolayer. *Elektrokhimiya* **14**, 1213-1215.

204. Bett, J., Kinoshita, K., Routsis, K. & Stonehart, P. 1973 A comparison of gas-phase and electrochemical measurements for chemisorbed carbon monoxide and hydrogen on platinum crystallites. *J. Catal.* **29**, 160-168. (doi:10.1016/0021-9517(73)90214-5).

205. Kinoshita, K. & Ross, P.N. 1977 Oxide stability and chemisorption properties of supported ruthenium electrocatalysts. *J. Electroanal. Chem. Interfacial Electrochem.* **78**, 313-318. (doi:10.1016/S0022-0728(77)80125-3).

206. Rodriguez, J.F., Mebrahtu, T. & Soriaga, M.P. 1987 Determination of the surface area of gold electrodes by iodine chemisorption. *J. Electroanal. Chem. Interfacial Electrochem.* **233**, 283-289. (doi:10.1016/0022-0728(87)85023-4).

207. Ross, P.N., Kinoshita, K., Scarpellino, A.J. & Stonehart, P. 1975 Electrocatalysis on binary alloys: I. Oxidation of molecular hydrogen on supported Pt−Rh alloys. *J. Electroanal. Chem. Interfacial Electrochem.* **59**, 177-189. (doi:10.1016/S0022-0728(75)80032-5).

208. Deyrieux, R., Berro, C. & Penéloux, A. 1973 Structure cristalline des oxalates dihydratés de manganèse, de cobalt, de nickel et de nickel. *Bull. Soc. Chim. Fr.* **1**, 25-34.

209. Herbert, J.M. & Ortiz, J.V. 2000 Ab Initio Investigation of Electron Detachment in Dicarboxylate Dianions. *The Journal of Physical Chemistry A* **104**, 11786-11795. (doi:10.1021/jp002657c).

210. Dean, P.A.W. 2012 The oxalate dianion, $C_2O_4^{2-}$: Planar or nonplanar? *J. Chem. Educ.* **89**, 417-418. (doi:10.1021/ed200202r).

211. Bhandari, N., Hausner, D.B., Kubicki, J.D. & Strongin, D.R. 2010 Photodissolution of Ferrihydrite in the Presence of Oxalic Acid: An In Situ ATR-FTIR/DFT Study†. *Langmuir* **26**, 16246-16253. (doi:10.1021/la101357y).

212. Mendive, C.B., Bredow, T., Feldhoff, A., Blesa, M.A. & Bahnemann, D. 2009 Adsorption of oxalate on anatase (100) and rutile (110) surfaces in aqueous systems: experimental results vs. theoretical predictions. *Phys. Chem. Chem. Phys.* **11**, 1794-1808. (doi:10.1039/b814608j).

213. Gao, B. & Liu, Z.F. 2005 First principles study on the solvation and structure of $C_2O_4^{2-}(H_2O)_n$, n = 6-12. *J. Phys. Chem. A* **109**, 9104-9111. (doi:10.1021/jp052968t).

214. Lasia, A. 2014 *Electrochemical Impedance Spectroscopy and its Applications*. New York, USA: Springer; 367 p.

215. Fleischmann, M., Korinek, K. & Pletcher, D. 1971 The oxidation of organic compounds at a nickel anode in alkaline solution. *J. Electroanal. Chem. Interfacial Electrochem.* **31**, 39-49. (doi:10.1016/S0022-0728(71)80040-2).

216. Parfitt, R.L., Fraser, A.R., Russell, J.D. & Farmer, V.C. 1977 Adsorption on hydrous oxides: II. Oxalate, benzoate and phosphate on gibbsite. *Journal of Soil Science* **28**, 40-47. (doi:10.1111/j.1365-2389.1977.tb02294.x).

217. Miller, F.A. & Wilkins, C.H. 1952 Infrared Spectra and Characteristic Frequencies of Inorganic Ions. *Anal. Chem.* **24**, 1253-1294. (doi:10.1021/ac60068a007).

218. Su, C. & Suarez, D.L. 1997 *In Situ* Infrared Speciation of Adsorbed Carbonate on Alumium and Iron Oxides. *Clays Clay Miner.* **45**, 814-825. (doi:10.1346/CCMN.1997.0450605).

219. Nyquist, R.A., Putzig, C.L., Leugers, M.A. & O, K.R. 1997 *The Handbook of Infrared and Raman Spectra of Inorganic Compounds and Organic Salts*. San Diego: Academic Press.

220. Yoon, T.H., Johnson, S.B., Musgrave, C.B. & Brown Jr, G.E. 2004 Adsorption of organic matter at mineral/water interfaces: I. ATR-FTIR spectroscopic and quantum chemical study of oxalate adsorbed at boehmite/water and corundum/water interfaces. *Geochim. Cosmochim. Acta* **68**, 4505-4518. (doi:10.1016/j.gca.2004.04.025).

221. Dobson, K.D. & McQuillan, A.J. 1999 In situ infrared spectroscopic analysis of the adsorption of aliphatic carboxylic acids to TiO_2, ZrO_2, Al_2O_3, and Ta_2O_5 from aqueous solutions. *Spectrochim. Acta, Part A* **55**, 1395-1405. (doi:10.1016/S1386-1425(98)00303-5).

222. Hug, S.J. & Bahnemann, D. 2006 Infrared spectra of oxalate, malonate and succinate adsorbed on the aqueous surface of rutile, anatase and lepidocrocite measured with in situ ATR-FTIR. *J. Electron Spectrosc. Relat. Phenom.* **150**, 208-219. (doi:10.1016/j.elspec.2005.05.006).

223. Duckworth, O.W. & Martin, S.T. 2001 Surface complexation and dissolution of hematite by C1-C6 dicarboxylic acids at pH = 5.0. *Geochim. Cosmochim. Acta* **65**, 4289-4301. (doi:10.1016/S0016-7037(01)00696-2).

224. García Rodenas, L.A., Iglesias, A.M., Weisz, A.D., Morando, P.J. & Blesa, M.A. 1997 Surface Complexation Description of the Dissolution of Chromium(III) Hydrous Oxides by Oxalic Acid. *Inorg. Chem.* **36**, 6423-6430. (doi:10.1021/ic9709382).

225. Axe, K. & Persson, P. 2001 Time-dependent surface speciation of oxalate at the water-boehmite (γ-AlOOH) interface: implications for dissolution. *Geochim. Cosmochim. Acta* **65**, 4481-4492. (doi:10.1016/S0016-7037(01)00750-5).

226. Degenhardt, J. & McQuillan, A.J. 1999 Mechanism of oxalate ion adsorption on chromium oxide-hydroxide from pH dependence and time evolution of ATR-IR spectra. *Chem. Phys. Lett.* **311**, 179-184. (doi:10.1016/S0009-2614(99)00848-9).

227. Persson, P. & Axe, K. 2005 Adsorption of oxalate and malonate at the water-goethite interface: Molecular surface speciation from IR spectroscopy. *Geochim. Cosmochim. Acta* **69**, 541-552. (doi:10.1016/j.gca.2004.07.009).

228. Giarola, D., Catarini da Silva, P., Urbano, A., Oliveira, F., Texeira Tarley, C. & Dall'Antonia, L. 2014 Surfactant effect on electrochemical-induced synthesis of α-Ni(OH)2. *J. Solid State Electrochem.* **18**, 497-504. (doi:10.1007/s10008-013-2280-3).

229. Coudun, C., Grillon, F. & Hochepied, J.-F. 2006 Surfactant effects on pH-controlled synthesis of nickel hydroxides. *Colloids and Surfaces A: Physicochemical and Engineering Aspects* **280**, 23-31. (doi:10.1016/j.colsurfa.2006.01.018).

230. Ida, S., Shiga, D., Koinuma, M. & Matsumoto, Y. 2008 Synthesis of Hexagonal Nickel Hydroxide Nanosheets by Exfoliation of Layered Nickel Hydroxide Intercalated with Dodecyl Sulfate Ions. *J. Am. Chem. Soc.* **130**, 14038-14039. (doi:10.1021/ja804397n).

231. Nethravathi, C., Rajamathi, M., Ravishankar, N., Basit, L. & Felser, C. 2010 Synthesis of graphene oxide-intercalated α-hydroxides by metathesis and their decomposition to graphene/metal oxide composites. *Carbon* **48**, 4343-4350. (doi:10.1016/j.carbon.2010.07.047).

232. Tan, Y., Srinivasan, S. & Choi, K.-S. 2005 Electrochemical Deposition of Mesoporous Nickel Hydroxide Films from Dilute Surfactant Solutions. *J. Am. Chem. Soc.* **127**, 3596-3604. (doi:10.1021/ja0434329).

233. Wang, M., Ren, W., Zhao, Y., Liu, Y. & Cui, H. 2013 One-pot synthesis of powder-form β-$Ni(OH)_2$ monolayer nanosheets with high electrochemical performance. *Journal of Nanoparticle Research* **15**, 1-8. (doi:10.1007/s11051-013-1849-1).

234. Sebastian, M., Nethravathi, C. & Rajamathi, M. 2013 Interstratified hybrids of α-hydroxides of nickel and cobalt as supercapacitor electrode materials. *Mater. Res. Bull.* **48**, 2715-2719. (doi:10.1016/j.materresbull.2013.03.029).

235. Huckaby, D.A. & Blum, L. 1991 A model for sequential first-order phase transitions occurring in the underpotential deposition of metals. *J. Electroanal. Chem. Interfacial Electrochem.* **315**, 255-261. (doi:10.1016/0022-0728(91)80074-Z).

236. Stickney, J.L., Stern, D.A., Schardt, B.C., Zapien, D.C., Wiekowski, A. & Hubbard, A.T. 1986 Electrodeposition of Pb onto Pt (111) surfaces containing iodine adlattices: Studies by low-energy electron diffraction and Auger spectroscopy. *J. Electroanal. Chem. Interfacial Electrochem.* **213**, 293-300. (doi:10.1016/0022-0728(86)80209-1).

237. Kakiuchi, T., Usui, H., Hobara, D. & Yamamoto, M. 2002 Voltammetric Properties of the Reductive Desorption of Alkanethiol Self-Assembled Monolayers from a Metal Surface. *Langmuir* **18**, 5231-5238. (doi:10.1021/la011560u).

238. Kirowa-Eisner, E., Bonfil, Y., Tzur, D. & Gileadi, E. 2003 Thermodynamics and kinetics of upd of lead on polycrystalline silver and gold. *J. Electroanal. Chem.* **552**, 171-183. (doi:10.1016/S0022-0728(03)00181-5).

239. Trotochaud, L., Young, S.L., Ranney, J.K. & Boettcher, S.W. 2014 Nickel-Iron Oxyhydroxide Oxygen-Evolution Electrocatalysts: The Role of Intentional and Incidental Iron Incorporation. *J. Am. Chem. Soc.* (doi:10.1021/ja502379c).

240. Wang, Y., Gai, S., Niu, N., He, F. & Yang, P. 2013 Fabrication and electrochemical performance of 3D hierarchical β-$Ni(OH)_2$ hollow microspheres wrapped in reduced graphene oxide. *Journal of Materials Chemistry A* **1**, 9083-9091. (doi:10.1039/c3ta11161j).

241. Fang, M., Engelhard, M.H., Zhu, Z., Helm, M.L. & Roberts, J.A.S. 2013 Electrodeposition from Acidic Solutions of Nickel Bis(benzenedithiolate) Produces a Hydrogen-Evolving Ni–S Film on Glassy Carbon. *ACS Catalysis* **4**, 90-98. (doi:10.1021/cs400675u).